Ultrafast electron dynamics and decoherence in metallic nanostructures

RafałJasiak
of the University of Strasbourg

A dissertation submitted to the University of Strasbourg for the degree of PhD

To my brother Piotr

Acknowledgements

It is a great pleasure to thank the many people who have contributed to this dissertation. I would like to pay my deepest thank to Giovanni Manfredi and Paul-Antoine Hervieux, my advisors, who opened a new domain of theoretical physics for me. Their creativity and deep knowledge were decisive for the success of our work. Besides, their care in all problems helped me much during these years of life in France, especially during my initial health problems. They have been the valued teachers, and I hope my four years at University of Strasbourg have given me even a few of their qualities.

Another large debt of thanks is due to my Polish friends with whom I spent many wonderful moments and who were always ready to offer help. In particular, let me express my gratitude to Piotr and Marcelina Klajner, Karolia Rybak, Marzena Materska and Alicja Siwek.

It was nice to work in the friendly atmosphere created by Yannick Hinschberger, Tomas Gelot, Emanuel Murat, Nhan Le Cong with whom I shared the office. I'm also thankful for their help in many difficult situations.

And finally, I should also like to thank all my family, especially my parents and my brothers for their support during hard times and faith in my success (dziękuje). Special acknowledgments I would like to address to my wife Kamila, for all her loving support, and her inordinate patience during the somewhat extended temporal interval over which this thesis was finally run to ground.

Contents

"There's Plenty of Room at the Bottom"

— Richard Feynman

Résumé

The ultrafast electron dynamics in thin metal films was studied numerically using a phase-space approach. For large excitation energies, the quantum and classical dynamics are virtually identical, whereas they diverge below a certain threshold, roughly equal to the plasmon energy. This is a clear signature of a quantum-mechanical effect, which should be observable in standard pump-probe experiments on thin metal films. For longer timescales, the electron dynamics becomes dissipative, as the electrons exchange energy incoherently with the ion lattice. A classical relaxation time and a quantum decoherence time were shown to emerge naturally from the simulations. These time scales are in good agreement with phenomenological estimates based on the two-temperature model, and correctly reproduce the main features observed in experiments on small sodium clusters.

Chapter 1

Introduction

Constantly progressing miniaturization of today's electronic devices has led to the development of new innovative nanosystems and nanostructured materials, which reveal effects not observed hitherto in their bulk counterparts. Also new theoretical and experimental techniques have been developed in order to give better insight into processes and phenomena occurring in such structures. Understanding these processes is a matter of great importance for both fundamental studies and possible technological applications.

Thin metal films of submicron thickness, which are typical examples of nanostructures, are widely used in modern high–speed electronic and optoelectronic devices. In those systems, the switching time can nowadays approach the femtosecond time domain. The electron distribution, in this time regime, is out of thermal equilibrium. In order to control the energy consumption, it is important to have better comprehension of the electron transport and energy relaxation on the femtosecond time–scale.

Over the last few decades, a dramatic progress of ultrafast spectroscopy techniques made it possible to monitor the femtosecond dynamics of an electron gas confined in metallic nanostructures such thin films [5–10], nanotubes [11], metal clusters [12, 13], and nanoparticles [5, 14]. In a typical experiments, the following schematic scenario is generally assumed: first, the electrons absorb quasi-instantaneously the laser energy via interband and/or intraband transitions. Under certain conditions (e.g. not too high energy transfer [15]) this early stage leads to the creation of a collective oscillation, the so-called surface plasmon. Subsequently, the plasmon oscillation is damped through coupling to self-consistent quasi-particle excitations (Landau damping). During these fast processes, the ionic background remains frozen and the electron distribution is nonther-

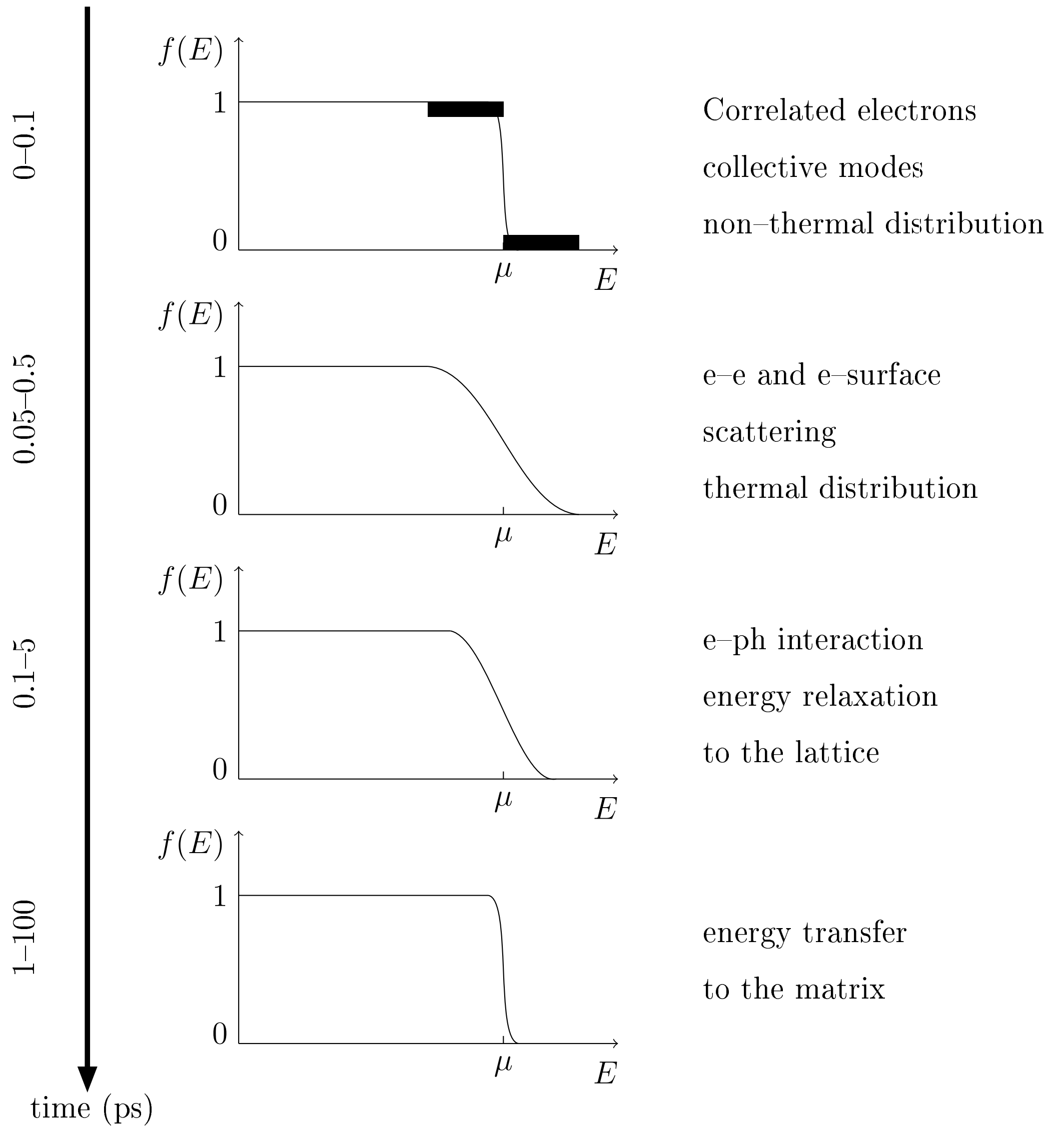

Figure 1.1: Sketch of the relaxation processes in a metallic nanopartice after an excitation by a femtosecond laser pulse. $f(E)$ represents the electronic distribution and μ is the chemical potential. (Inspired by Ref. [5])

mal. As a result, the electron temperature cannot be properly defined at this stage of the relaxation process. On a longer timescale ($>$50 fs), the injected energy is redistributed among the electrons via electron–electron collisions, leading the electron population to a metastable equilibrium at a temperature significantly higher than that of the lattice. On a picosecond timescale, the electron gas starts to interact incoherently with the phonons, and eventually relaxes to the thermal equilibrium at the same temperature as the lattice. The lattice motion occurs on even longer time scales, ranging from tens of picoseconds to a few nanoseconds for the final heat transfer to the dielectric matrix in which the nano-objects are usually embedded. A schematic representation of the energy relaxation following the strong excitation by the femtosecond pump pulse, is shown in figure 1.1.

In order to model and interpret such experimental results obtained with large nanoparticles, *ab initio* methods cannot be employed, as they involve prohibitive computational time. Also the theoretical models [16–19] originally developed for bulk materials, such as phenomenological Boltzmann–type equations that provide the time evolution of the electron occupation number, fail to describe finite-size systems because the interfaces, which play a crucial role in the ultrafast dynamics, are not included.

A possible alternative relies on the use of kinetic methods originally developed for plasma physics. These methods are capable to reproduce processes occurring in nanoparticles since the valence electrons can be assimilated to an inhomogeneous electron plasma. In those methods the quantum electron dynamics is described in the phase space by the Wigner equation, coupled self-consistently to the Poisson equation. In the semiclassical limit, the Wigner–Poisson system reduces to the Vlasov–Poisson equations.

The Wigner representation [20] is a useful tool to express quantum mechanics in a phase space formalism. In this representation, a quantum state (either pure or mixed) is described by a Wigner function, i.e. a function of the phase space variables. Although the Wigner distribution satisfies most of the standard properties of probability distributions, it cannot be regarded as such, since it may take negative values.

The purpose of the present thesis is to provide extensive computational results on the ultrafast electron dynamics in thin metal films, based on a phase-space description within the Wigner formalism. We propose a model to describe the microscopic electron dynamics over all time scales from the laser excitation up to the coupling with the ion lattice. We shall focus our attention on the electron dynamics in alkali metals (particularly sodium), for which the valence electrons are fully delocalized and the influence of the core electrons can be neglected. Simple sodium films constitute the first and the simplest step towards more complex materials and, for that reason, should be thoroughly understood.

1.1 Nanostructures

When we refer to the expression "nanostructures" we usually think about objects composed of 10^6 atoms or less, whose properties differ from those of the same atoms bound in the bulk materials. Although the words "nanoparticles" and "nanotechnology" are relatively new, nanoparticles themselves have been present and studied long before they have gained such widespread interest. For example, many of the stained glass windows owe their beautiful colors to the presence of small metal oxide clusters. Also the process of image formation in photography is due to small colloidal particles of silver.

Nanostructures are generally considered as a whole unit made of atoms bound together with a radius between 1 nm and 100 nm. The approximate classification of the particles according to their size in presented in figure 1.2. The definition based on size is not fully relevant because is doesn't really distinguish between molecules and nanoparticles. Many molecules contain more than 25 atoms, particularly biological ones. What makes nanoparticles interesting is that their size is smaller than the critical length that characterize many macroscopic physical phenomena (like a thermal diffusion length, or mean free path).

As the size of the particles approaches the atomic scale, the relevant physical laws change form the classical to the quantum–mechanical laws, represented by Schrödinger's equation. Small particles exhibit wave–like behavior and they must be described by quantum mechanics. When we consider the dimensionality of a nano-object, it is reasonable to compare its size with an appropriate intrinsic characteristic length. In the quantum regime the most relevant length scale is the Fermi length λ_F. Considering a rectangular sample of sizes L_x, L_y, and L_z, following Ref. [21] one can distinguish:

- $\lambda_F \ll L_x \approx L_y \approx L_z$: 3D (bulk samples)
- $L_x \approx \lambda_F \ll L_y \approx L_z$: 2D (films)
- $L_x \approx L_y \approx \lambda_F \ll L_z$: 1D (quantum wires)
- $L_x \approx L_y \approx L_z \approx \lambda_F$: 0D (quantum dots)

Metallic nanostructures are particularly interesting systems because of the convenience with which they can be synthesized and modified chemically.

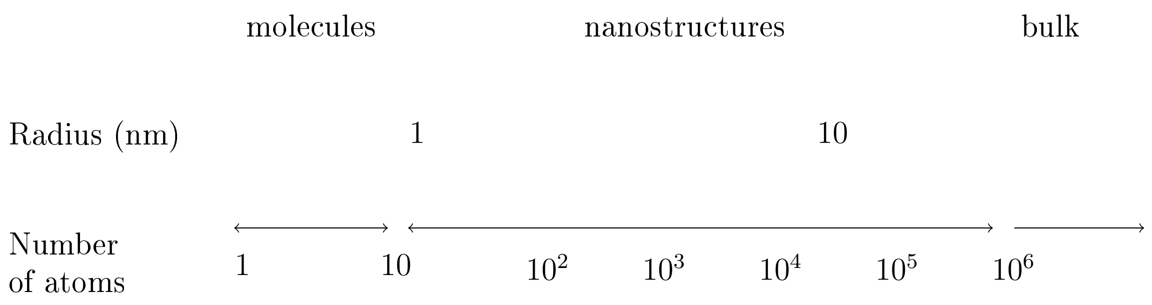

Figure 1.2: Schematic classification of the particles with respect to the number of atoms. (Inspired by Ref. [22])

1.1.1 Thin metal films

Thin metal films constitute a very important branch of nanotechnology. Recent advances in this field made them particularly attractive from the point of view of possible application as a basis to advanced technologies, devices and new materials. Thin films have properties remarkably different form their bulk counterparts due to their symmetry reduction, geometric confinement of electrons, and boundary effects. All those effects are very complicated and the complete understanding of these processes is based on multidisciplinary research in solid state physics and chemistry, surface science, statistical and computational physics. Thanks to their simple geometry, thin metal films constitute an ideal tool for a detailed study of the connection between atomistic details and macroscopic physical and chemical properties.

One of the most important properties of thin films is the quantization of the energy levels along the direction perpendicular to the film surface. The continuum characterizing the bulk materials in replaced, due to the quantum confinement, by a discrete spectrum of quantum states with their energies depending on the boundary conditions. The consequent modifications of the electronic structure can lead to significant changes of their physical properties.

In the present work, we would like to present a numerical study of the temporal evolution of the electron gas confined in a thin metal film after a laser excitation, and improve the basic knowledge of the light–matter interaction in the nonlinear regime. Before, however, we get to this point let us first discuss some experiments describing some of the most important transport properties in thin metal films.

1.1.2 Experiments on thin metal films

Some experiments [6, 7] in which the authors have measured the properties of heat transport in thin gold films, showed that it is not a diffusive process, but rather a ballistic one (unimpeded flow of electrons). These works also demonstrated that heat transport occurs on a femtosecond time scale and involves nonequilibrium electrons traveling at a velocity close to the Fermi velocity of the metal.

One of the most popular tools to investigate fundamental processes occurring in the excited electronic systems is the pump–probe experiments. Pump–probe measurements involve pulsed laser excitations of the system at one surface of the metallic thin film, followed by a second, appropriately delayed, pulse that acts as a diagnostic tool. The development of ultrashort laser pulses (in the femtosecond time domain) allows to resolve the dynamical properties of nonequilibrium electrons with great accuracy. On the other hand, if the pulse duration is longer ($> 1-10$ ps), excited particles and their surroundings have enough time to approach thermal equilibrium, and the results of these experiments differ significantly from those with temporal resolution shorter than 500 fs. Another advantage of this approach is that except for the dynamics of nonequilibrium particles, we can also investigate particle transport.

In Ref. [6] the authors investigate the reflectivity changes induced by electronic temperature variation in gold thin films. The results were obtained by both front–probe and back–probe thermomodulation measurements designed to distinguish between relaxation due to heat flow out of the probed region and electronic relaxation via phonon emission. The principle of the measurement was based on the fact that an ultrashort laser pulse heats the electrons at the front surface, and in this way changes the occupancy of electronic states near the Fermi level, which in turns affects the transition rate. The imaginary part of the dielectric function $\varepsilon = \varepsilon_1 + i\varepsilon_2$ is sensitive to changes in the transition rate. Since the reflectivity R of the sample depends upon ε, the experimental change in R marks the electron temperature change.

A schematic representation of the experimental setup is presented in figure 1.3 (left panel), together with the fractional reflectivity $\Delta R/R$ (right panel) for several values of the thickness of the film L. From the reflectivity plots it appears that the delay time of the rise of the reflectivity changes with the sample thickness. This effect is a

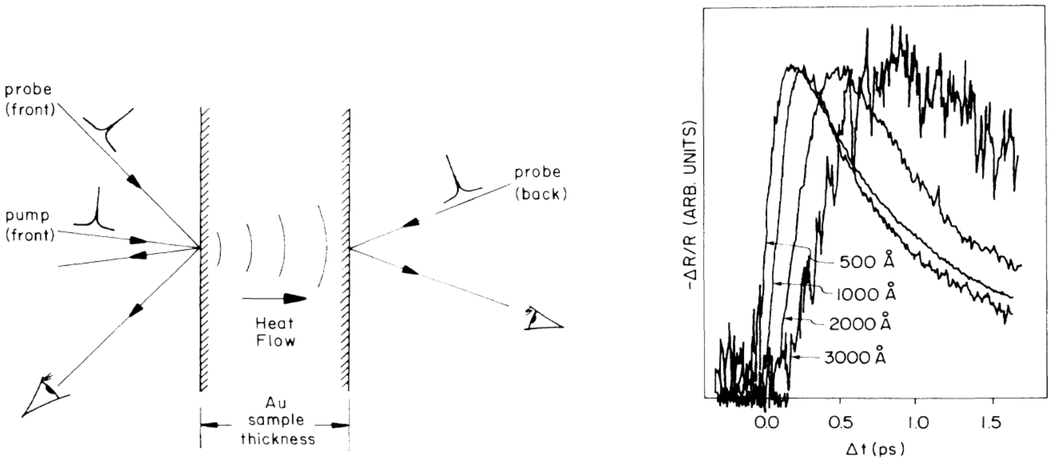

Figure 1.3: Left panel: schematic representation of the pump–probe experiments. The sample is pumped on the front surface, and the change in reflectivity at either the front or the back surface is probed. Right panel: reflectivity change for Au films of different thicknesses. (Both reprinted from Ref. [6])

direct consequence of the finite time needed for heat to propagate through the sample. By plotting the sample thickness against the measured delay (figure 1.4), the authors obtained approximately a linear relation, from which it is possible to extract a heat transport velocity being of the order of the Fermi velocity of Au. This situation implies the ballistic motion of excited particles. The electrons propagate through the film without experiencing any large scattering and are detected at the rear surface after a delay $\Delta t = L/v_F$.

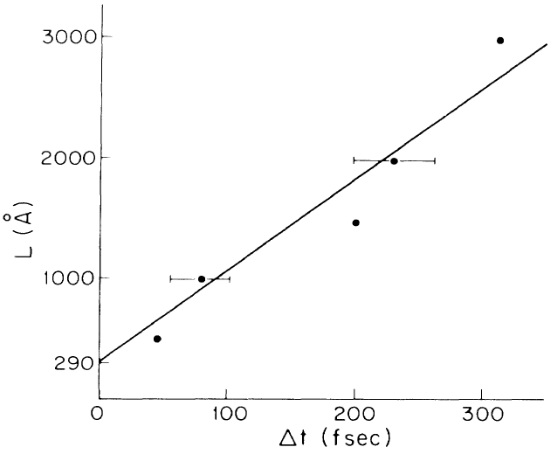

Figure 1.4: Samples thickness as a function of time of flight for various Au films (reprinted from Ref. [6]).

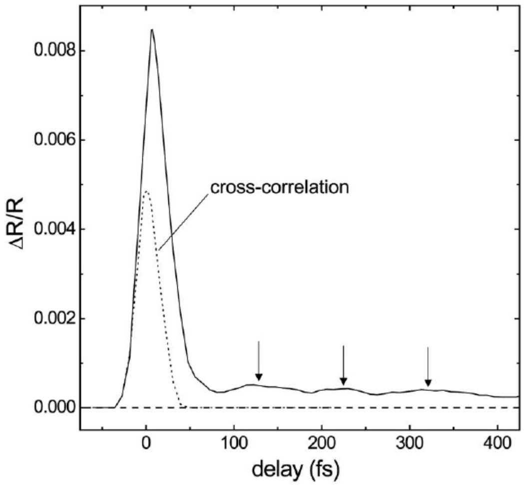

Figure 1.5: Transient reflectivity of a 45 nm Au film. (Reprinted form Ref. [23].)

Ballistic transport of the excited particles in thin metal films can suggest the possibility that some of the initial nonthermal electrons may be reflected back at one surface and propagate to the other surface where they experience another reflection. A few such a roundtrips have been shown experimentally [23] in the behavior of the transient reflectivity signal in a pump–probe experiments. Figure 1.5 shows the transient reflectivity result for a gold film of thickness 45 nm. After an initial fast decay of the transient reflectivity we can clearly observe some damped oscillations. The period of the oscillations is found to be about 107 fs, which, by assuming transport perpendicular to the film surface, gives an effective velocity of about $0.86 \cdot 10^6$ m/s. This velocity is of the same order of magnitude as the Fermi velocity $v_F = 1.4 \cdot 10^6$ m/s of gold. Similar low–frequency oscillations were also observed for smaller films, with the period scaled proportionally to the thickness of the film. The explanation of the observed modulation of the reflectivity is based on the ballistic motion of the electrons near the Fermi level.

For longer pulse durations, the non–thermal components of the electron gas (represented by the top graph in figure 1.1) are very fast and usually hidden in the noise of the experimental results. It is still possible, however, to extract from such measurements some useful information about the processes leading to thermal equilibrium between the electron gas and the ion lattice [5]. Figure 1.6 shows the differential transmission $\Delta T/T$, and the differential reflection $\Delta R/R$, together with the corresponding change of the real and imaginary parts of the dielectric function ε obtained on a 33 nm thick Ag film. The signals for $\Delta T/T$ and $\Delta R/R$ both decay exponentially with a similar relaxation

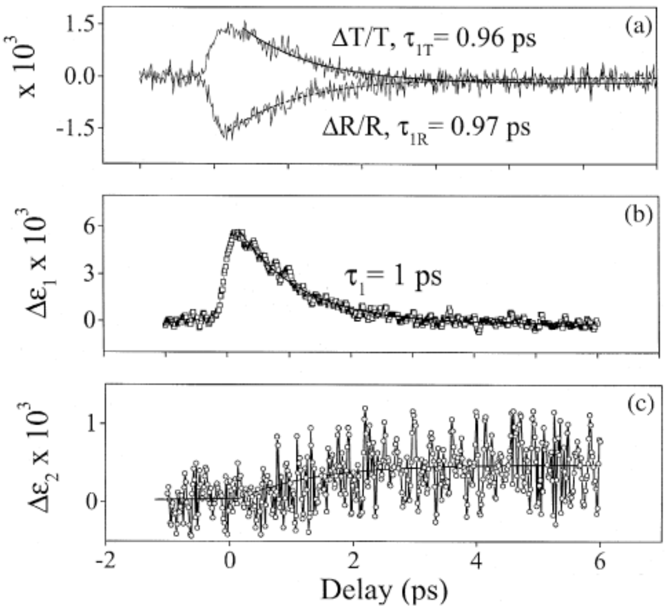

Figure 1.6: Time dependence of $\Delta T/T$, $\Delta R/R$ (a), $\Delta\varepsilon_1$ (b), and $\Delta\varepsilon_2$ (c) in a 33 nm thick silver film. (Reprinted form Ref. [5])

rate of 960 ± 20 fs. These decay times are related to the cooling of the electrons to the lattice and to the simultaneous increase of the lattice temperature. The electron dynamics in this situation is governed mainly by two mechanism: the electron–electron interaction and the energy relaxation to the lattice. The latter process can be described by the exchange of temperature between the electrons and the lattice in the framework of so-called two-temperature model.

The above experiment describes the long-time electron relaxation, which involves electron–phonon interactions. The considered time scales differ quite significantly from those discussed in the experiments mentioned earlier, and highlight effects leading to the thermal equilibrium. In our numerical representation we would like to include all these phenomena and propose a model that is capable of reproducing all those processes.

1.2 Theoretical approach

The injection of the laser pulse energy into the system of electrons generates strongly out-of-equilibrium situation. One of the possible tools to study the evolution of charged particles in such a condition is provided by the kinetic theory, and the corresponding kinetic equations that govern the dynamics. In those methods the electron population is described by a distribution function $f(x, v, t)$ in the phase-space [24]. The full kinetic model is provided by the Wigner equation [25], which is particularly attractive as it recasts quantum mechanics in a classical phase space formalism. In the classical limit the Wigner equation reduces to the Vlasov equation [26], and these two models will be used here to investigate the electron dynamics.

Although the Wigner approach is fully quantum the quantization rules are omitted and should be imposed by additional constraints. Thus, for the calculation of the ground-state, we make use of the standard density functional theory (DFT), which is a widely used and efficient tool for self-consistent calculations of electronic structures. The main feature of this technique is that the density of the interacting electron system can be obtained as the density of an auxiliary system of non-interaction electrons moving in an effective local single-particle potential. More details of this representation we will be given in the next chapter as there is an intimate connection between the electronic wavefunctions and the Wigner function.

1.2.1 Distribution function

In classical physics, at any given time, each particle has a specific position and velocity. The instantaneous configuration of a large number of particles is thus characterized by specifying the density of particles at each point x, v in the phase-space. The function prescribing the instantaneous density of particles in the phase-space is called the *distribution function* and is denoted by $f(x, v, t)$. Thus, $f(x, v, t)dxdv$ is the number of particles at time t having positions in the interval x and $x + dx$ and velocities in the range between v and $v + dv$.

$$f(x, v, t)dxdv = \text{Number of particles in } dxdv \text{ at time } t$$

As time progresses, the particle motion and acceleration causes the change of the number of particles in a given phase-space volume, so that f will change. The characterization of the system by f does not keep track of the trajectories of individual particles, but rather characterizes classes of particles having the same x and v.

1.2.2 Classical Vlasov equation

In order to understand better the evolution of the distribution function in the phase space let us recall an example shown in Ref. [27]. Let us consider the ensemble of alike particles in a two dimensional phase-space x, v showed in figure 1.7. Let us try to find the rate of change of the number of particles inside a small box $dxdv$. Defining $a(x, v, t)$ to be the acceleration of a particle, it is seen that the particle flux in the horizontal direction is fv and the particle flux in the vertical direction is fa. Thus, the particle fluxes into the four sides of the box are:

I. Flux into left side of box is $f(x, v, t)vdv$

II. Flux into right side of box is $-f(x + dx, v, t)vdv$

III. Flux into bottom of box is $f(x, v, t)a(x, v, t)dx$

IV. Flux into top of box is $-f(x, v + dv, t)a(x, v + dv, t)dx$

Since the number of particles in this box is $f(x, v, t)dxdv$, the rate of change of the particles in the box is:

$$\begin{aligned}\frac{\partial f(x,v,t)}{\partial t}dxdv = & - \; f(x+dx,v,t)vdv + f(x,v,t)vdv \\ & - \; f(x,v+dv,t)a(x,v+dv,t)dx + f(x,v,t)a(x,v,t)dx\end{aligned} \tag{1.1}$$

by expanding the quantities on the right hand side in Taylor series, we obtain the one dimensional *Vlasov equation*

$$\frac{\partial f}{\partial t} + v\frac{\partial f}{\partial x} + \frac{\partial}{\partial v}(af) = 0 \tag{1.2}$$

Because x, v are independent variables in phase-space, the spatial derivative term has the commutation property

$$v \cdot \frac{\partial f}{\partial x} = \frac{\partial}{\partial x} \cdot (vf). \tag{1.3}$$

For typical electrostatic problems the acceleration can be written as

$$a = \frac{e}{m}\frac{\partial \phi}{\partial x} \tag{1.4}$$

where ϕ is the electrostatic potential. Because the acceleration in that case is independent of the velocity we can write

$$a \cdot \frac{\partial f}{\partial v} = \frac{\partial}{\partial v} \cdot (af) \tag{1.5}$$

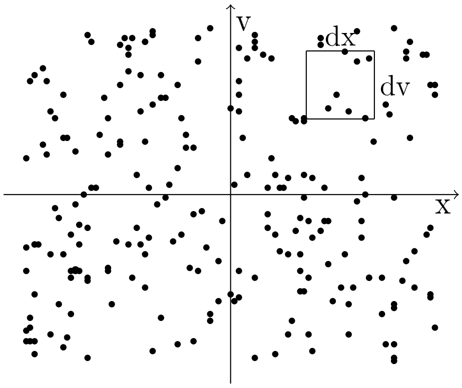

Figure 1.7: One–dimensional phase space with randomly distributed particles.

and the Vlasov equation can also be written in the following form:

$$\frac{\partial f}{\partial t} + v\frac{\partial f}{\partial x} + \frac{e}{m}\frac{\partial \phi}{\partial x}\frac{\partial f}{\partial v} = 0. \tag{1.6}$$

In the present thesis we make use of the Vlasov equation to describe the classical electron dynamics in thin metal films. Within the mean field approximation the electric potential can be calculated by Poisson equation:

$$\frac{\partial^2 \phi}{\partial x^2} = \frac{e}{\varepsilon_0}\left(\int f dv - n_i\right). \tag{1.7}$$

where n_i is the ion density. The one–dimensional (1D) approximation used in equations (1.6) and (1.7) relies on the fact that a thin film can be considered as an infinite slab of thickness L. This assumption holds if the film size in the directions parallel to its surface is large compared with L. In this case, it is suitable to use a 1D model, where only the normal coordinate x and its corresponding velocity v play a role.

The Vlasov–Poisson (VP) model satisfies some basic physical properties like, for example:

- mass conservation

$$\frac{d}{dt}\iint f(t,x,v)dxdv = 0 \tag{1.8}$$

- momentum conservation

$$\frac{d}{dt}\iint f(t,x,v)vdxdv = 0 \tag{1.9}$$

- energy conservation

$$\frac{d}{dt}\left\{\frac{m}{2}\iint f(t,x,v)v^2 dx dv + \frac{\varepsilon_0}{2}\int E^2(t,x)dx\right\} = 0 \tag{1.10}$$

  where $E(t,x) = -\partial\phi/\partial x$ is the electric field. The latter expression can be obtained by multiplying the Vlasov equation by v^2, and integrating by parts.

Concerning the initial condition for the electrons, the relevant equilibrium is given by the quantum Fermi–Dirac statistics. In that sense, this model can be referred as semiclassical (it includes the Fermi–Dirac distribution for the ground state, but neglects the quantum character of the electron dynamics). When dealing with such a representation it is important that the numerical scheme preserve the fermionic character of the electron. For the VP model, a form of the exclusion principle is satisfied if f respects the following condition [28]: $f(x,v,t) \leq f(x,v,t=0)$, where $f(x,v,t=0)$ is the ground state Fermi–Dirac distribution. This property (known mathematically as the "maximum principle") is indeed satisfied by the Vlasov equation (1.6).

1.2.3 Wigner formalism

The phase space (x,v) cannot have the same meaning in classical and in quantum mechanics. We are not able to represent a pure state of the system by a point in phase space, because the Heisenberg's uncertainty principle states that x and v cannot be known simultaneously with arbitrary precision. As a result, it is also not possible to define a quantum distribution function on the phase space which can be interpreted as a probability density. However, it is still possible to construct a phase-space formalism for quantum mechanics which preserves many of the classical features.

The phase-space formation of quantum mechanics has its roots in the work of Wigner [29], where he introduced the phase space distribution function that now bears his name. This formalism can often provide useful physical insights that cannot easily be gained from other approaches. Furthermore, it requires dealing only with constant–number equations and not with operators, which can sometimes be a significant practical advantage. The main tool for the phase-space formulation of quantum mechanic is the phase-space distribution function. There is no unique way of defining a quantum phase-space distribution function [30] and therefore it should be considered simply as a mathematical tool that facilitates quantum calculations.

We now turn to a somewhat more general description of the Wigner formalism, in terms of the standard concepts of quantum mechanics.

Wigner function

The state operator, in quantum-mechanics, $\rho = |\psi\rangle\langle\psi|$ can be written in the position representation $\langle q|\rho|q'\rangle$ or in the momentum representation $\langle p|\rho|p'\rangle$. The Wigner representation is, in a sense, intermediate between these two. For a single particle in one dimension, it is defined as [31]

$$f(q,p,t) = \frac{1}{2\pi\hbar}\int\limits_{-\infty}^{\infty} \langle q - \frac{1}{2}\lambda \mid \rho \mid q + \frac{1}{2}\lambda\rangle e^{ip\lambda/\hbar} d\lambda \tag{1.11}$$

The Wigner representation can also be obtained from the momentum representation,

$$f(q,p,t) = \frac{1}{2\pi\hbar}\int\limits_{-\infty}^{\infty} \langle p - \frac{1}{2}k \mid \rho \mid p + \frac{1}{2}k\rangle e^{iqk/\hbar} dk \tag{1.12}$$

showing that it is, indeed, intermediate between the position and momentum representations. The generalization to N particles in three dimensions requires that all variables be interpreted as $3N$–dimensional vectors, and that the factor $(2\pi\hbar)^{-1}$ becomes $(2\pi\hbar)^{-3N}$.

The Wigner function appears as an average value (calculated with ρ) of operators that are not necessarily positive definite. It means that the Wigner function is not everywhere positive (or zero), but may take also negative values. Consequently, it cannot be interpreted as a probability distribution. This is the price to be paid in order to be able to represent a quantum state in the classical phase-space. It is, however, remarkable that the Wigner function provides a perfectly self-consistent formalism for calculating averages, quite analogous to that of classical statistical mechanics. For example the Wigner function reproduces the correct quantum-mechanical marginal distributions:

$$\int\limits_{-\infty}^{\infty} f(q,p) dp = \langle q \mid \rho \mid q\rangle, \tag{1.13}$$

$$\int\limits_{-\infty}^{\infty} f(q,p) dq = \langle p \mid \rho \mid p\rangle. \tag{1.14}$$

Other useful properties of the quantum distribution function can be summarized as follows:

- The distribution function is real-valued for all q, p, and t
- It can be used to compute averages just like in classical statistical mechanics. For example, the expectation value of a generic quantity $A(p, q)$ is defined as:

$$\langle A \rangle = \frac{\iint f(q,p)A(q,p)dqdp}{\iint f(q,p)dqdp} \tag{1.15}$$

- if $\langle \Psi_i | \Psi_j \rangle = \delta_{ij}$ the set of functions f_i form a complete orthogonal set

$$\int f_i f_j dxdv = \delta_{ij}/2\pi\hbar. \tag{1.16}$$

Wigner approach for many-body problems

The Wigner function in terms of the single–particle wavefunctions ψ_i reads as [32]

$$f(x,v,t) = \sum_{i=1}^{N} \frac{m}{2\pi\hbar} w_i \int\limits_{-\infty}^{\infty} \psi_i^*(x + \frac{\lambda}{2}, t)\psi_i(x - \frac{\lambda}{2}, t) e^{imv\lambda/\hbar} d\lambda. \tag{1.17}$$

where w_i stands for the occupation weights. As was stated above, the Wigner function is capable to reproduce the correct quantum-mechanical distribution, so the spatial density must satisfy the relation:

$$n(x,t) = \int\limits_{-\infty}^{\infty} f(x,v,t)dv = \sum_{i=1}^{N} w_i |\psi_i|^2. \tag{1.18}$$

The evolution equation for the Wigner function in its integro–differential form is given by the following formula:

$$\begin{aligned} &\frac{\partial f}{\partial t} + v\frac{\partial f}{\partial x} + \\ &\frac{em}{2i\pi\hbar^2} \iint d\lambda dv' e^{im(v-v')\lambda/\hbar} \left[\phi\left(x + \frac{\lambda}{2}\right) - \phi\left(x - \frac{\lambda}{2}\right)\right] f(x, v', t) = 0 \end{aligned} \tag{1.19}$$

where $\phi(x,t)$ is the self-consistent electrostatic potential. The Wigner equation must be coupled to Poisson's equation (1.7) for the electric potential. Similarly like in the Vlasov case, the Wigner equation also satisfies the physical properties like mass, momentum, and energy conservation.

Developing the integral in (3.17) up to order $O(\hbar^2)$ we obtain

$$\frac{\partial f}{\partial t} + v\frac{\partial f}{\partial x} + \frac{e}{m}\frac{\partial \phi}{\partial x}\frac{\partial f}{\partial v} = \frac{e\hbar^2}{24m^3}\frac{\partial^3 \phi}{\partial x^3}\frac{\partial^3 f}{\partial v^3} + O(\hbar^4). \tag{1.20}$$

In the formal semiclassical limits $\hbar \to 0$ we obtain the Vlasov equation (1.6).

In summary, the Wigner representation is a useful tool to provide information about the state of the system in the phase-space. This contrasts with the more conventional representations, which may provide information about position only, or about momentum only, but not both together. It should be stressed, however, that the Wigner function is not a real probability distribution, because it takes both positive and negative values. The negativity of the Wigner function is a purely quantum effect (in classical physics we do not deal with negative probability distribution), and can be used as a measure of "classicality" of a given quantum state [33], which in turns is related to the loss of quantum coherence.

1.3 Outline of this thesis

In this thesis we investigate the problem of the ultrafast electron dynamics in thin sodium films over all time scales up to the coupling with the ion lattice, and the resulting quantum decoherence. Our numerical approach is based on the Wigner formalism, which is particularly attractive as it allows to unravel complicated quantum mechanical processes in the familiar phase-space representation. In the classical limit, the Wigner equation reduces to the Vlasov equation, and these two models will serve us to describe the electron dynamics. In this work, we adopt a one–dimensional approximation, which relies on the fact that a thin film can be viewed as an infinite slab. This assumption holds if the film size in the direction parallel to its surfaces are large compared to the film thickness.

The manuscript is organized as follows: In Chapter 2, we present the ground state properties of our system. For this purpose, we make use of the Density Functional Theory (DFT) thanks to which we are able to compute the wavefunctions and energy levels in a slab geometry (Sec. 2.1). These results are used to construct the ground-state Wigner function as it is described in Sec 2.2.

Chapter 3 is devoted to the description of our dynamical models. We describe in more details typical time, length and velocity scales (Sec. 3.1) associated with an electron gas, which are used in the representation of our results. The numerical aspects of our approach are specified in Sec. 3.3. In Sec. 3.4 we present also some details of the linear response, which is possible to attain with a small modification of our model.

The main topic of this thesis, i.e., the electron dynamics, is investigated in Chapters 4 and 5. Fist, we study the ultrafast processes appearing shortly after the injection of the laser energy. In particular, we are interested in the dipole oscillation and energy evolution. Systematic comparisons between the classical and the quantum results will reveal a clear classical–quantum transition occurring at low excitation energy (Sec 4.3). The threshold of this transition corresponds roughly to the quantum of energy of a plasmon oscillation (Sec 4.4).

The results of Chapter 4 are devoted to the early stages of the electron dynamics, during which the ionic background remains frozen. The inclusion of the electron–lattice interaction is provided in Chapter 5. The advantage of the phase-space description of the quantum electron dynamics is that dissipative terms can be introduced by analogy with classical transport models, such as the Fokker–Planck equation. The electron–phonon coupling can be modeled by a set of two coupled differential equations, called two-temperature model. In Sec 5.2 we compare the results of the Wigner simulations with those obtained form the two-temperature model. The negativity of the Wigner function is a pure quantum effect and it can be used to evaluate the decoherence time, which represents the typical time over which quantum correlations are lost to the ion lattice. This issue is investigated in Sec. 5.2.

In Chapter 6 we leave the electrons dynamics in metal films and turn to the interesting subject of the quantum fidelity in semiconductors. We investigate there the influence of a random potential on the wavefunctions and energy levels of an electron gas confined in a nonparabolic quantum well.

Finally, conclusions and perspectives are discussed in Chapter 7.

Chapter 2

Ground-state

Numerical study of the electron dynamics can be divided into two steps: first, the ground state of the electron population (at finite temperature) is determined self-consistently; and subsequently, the equilibrium distribution is perturbed by injecting some energy into the system. The quantum dynamics is described by the time-dependent Wigner equation, which was described briefly in the previous chapter. Although the Wigner approach is a fully quantum-mechanical description, it is intrinsically ill-suited to deal with stationary states (indeed, quantization rules are overlooked by the Wigner formalism, and must be imposed as additional constraints). It is more convenient to determine the ground-state from a standard density functional approach (Kohn—Sham equations), and then construct the Wigner function from the computed Kohn—Sham wavefunctions.

2.1 Density functional theory

Density-functional theory [34] developed by Hohenberg and Kohn (1964) and Kohn and Sham (1965) provided methods of investigating the electronic structure of many-body system. Hohenberg and Kohn proved that the total energy of an electron gas is unique functional of the electronic density $n(\vec{r})$:

$$E[n] = T[n] + \int n(\vec{r}) V_{ion}(\vec{r}) d^3\vec{r} + \frac{1}{2} \int d^3\vec{r} \int \frac{n(\vec{r})n(\vec{r}')}{|\vec{r} - \vec{r}'|} d^3r' + E_{xc}[n]. \qquad (2.1)$$

The minimum value of the total energy functional is the ground-state energy of the system, and the density that yields this minimum value is the exact single-particle ground-state density. The first term in this expression represents the kinetic energy of an equivalent non-interacting electron system with the same ground-state density as that of the exact many-body electron system. The second term is the potential energy due to the electron–ion interaction, with $V_{ion}(\vec{r})$ representing the Coulomb potential generated by the positive ionic charges. The third denotes the average electron-electron interactions. The last one is the exchange–correlation energy which contains all the remaining many-body interactions. The many-electron wave function must be antisymmetric under exchange of any two electrons because electrons are fermions. The antisymmetry of the wave function produce a spatial separation between electrons that have the same spin and thus reduces the Coulomb energy of the electronic system. This energy reduction is called the exchange energy, and this is generally referred to as the Hartree–Fock approximation. The Coulomb energy of the electronic system can be reduced below its Hartree–Fock value if electrons that have opposite spins are also spatially separated. In this case the Coulomb energy of the electronic system is reduced at the cost of increasing the kinetic energy of the electrons. The difference between the many-body energy of an electronic system and the energy of the system calculated in the Hartree–Fock approximation is called the correlation energy.

An important practical advantage of the density functional approach is that the electron density can be derived from the solution of a one-electron Schrödinger-like equation (Khon–Sham equation)

$$\left[-\frac{\hbar^2}{2m}\nabla^2 + V_{eff}(\vec{r})\right]\Psi_\nu(\vec{r}) = E_\nu\Psi_\nu(\vec{r}) \tag{2.2}$$

where the effective potential V_{eff} is given by

$$V_{eff}(\vec{r}) = V_{ion}(\vec{r}) + \int \frac{e^2 n(\vec{r}')}{|\vec{r}-\vec{r}'|}d^3r' + V_{xc}(\vec{r}) \tag{2.3}$$

with

$$V_{xc} = \frac{\delta E_{xc}[n]}{\delta n(\vec{r})}. \tag{2.4}$$

The electronic density is then

$$n_e(\vec{r}) = \sum_\nu f_\nu|\Psi_\nu(\vec{r})|^2 \tag{2.5}$$

where f_ν are the Fermi–Dirac occupation numbers. The Kohn–Sham equations must be solved self-consistently so that the occupied electronic states generate a charge density that produce the effective potential which is used to build the equation. This equation shows that we can replace the full many-body problem of interacting electron gas by an equivalent set of self-consistent one-electron equations.

2.1.1 Metal slab

In this work, we consider a thin metal film (or semiconductors, see Chapter 6) of thickness $L = d - 2x_0$ containing a degenerate system of electrons interacting via the Coulomb potential (figure 2.1). According to the jellium model the ionic background is replaced by a constant ionic charge density $\rho_i = e\overline{n}_i$ (of the bulk material) where e denotes the absolute electron charge ($e > 0$). In atomic units we have $\overline{n}_i = \frac{3}{4\pi r_s^3}$ where r_s is the Wigner-Seitz radius. The two parallel faces of the jellium film are assumed to be normal to the x–axis. The normalization area in the $y-z$ plane is A. The total number of electron is $N = LA\overline{n}_i \equiv N_s A$. It is convenient to render the electronic system strictly finite in the x direction by assuming that the electron-density profile actually vanishes at finite distance (denoted by x_0) from the jellium edges. In the jellium model, the effective energy potential (the self-consistent energy potential) depends only on the coordinate normal to the surface ($y - z$ plane) i.e. $V_{eff}(\vec{r}) = V_{eff}(x)$. The motion of an electron in the plane of surface completely decouples from it's motion along the x–direction and therefore we have

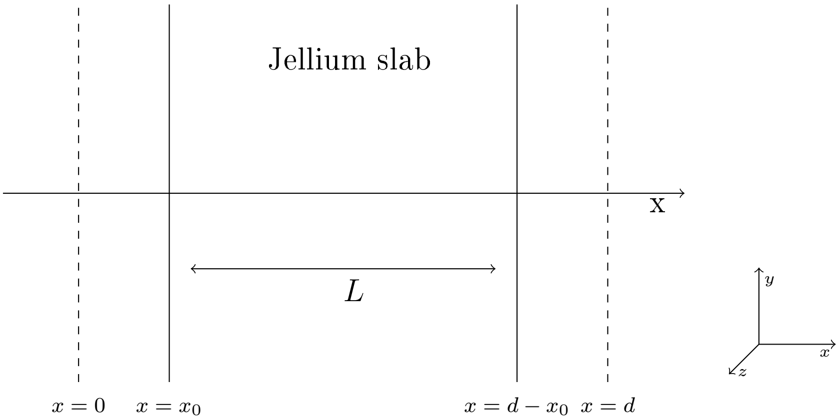

Figure 2.1: Jellium geometry

$$\Psi_\nu(\vec{r}) = \frac{e^{i\vec{k}_{\shortparallel}\cdot\vec{r}_{\shortparallel}}}{\sqrt{A}}\psi_l(x), \tag{2.6}$$

where $\vec{r}_{\shortparallel}$ and $\vec{k}_{\shortparallel}$ are, respectively, position and wave vectors in the $y - z$ plane and the total energy reads,

$$E_\nu = \frac{\hbar^2 k_{\shortparallel}^2}{2m} + \varepsilon_l. \tag{2.7}$$

From $(2.6, 2.7, 2.2)$, $\psi_l(x)$ and ε_l (ε_l have discrete values) are the stationary wave functions and the associated energy eigenvalues solutions of the one-dimensional Schrödinger equation

$$\left[-\frac{\hbar^2}{2m}\frac{d^2}{dx^2} + V_{eff}(x)\right]\psi_l(x) = \varepsilon_l \psi_l(x). \tag{2.8}$$

The effective potential $V_{eff}(x)$ is given by

$$V_{eff}(x) = V_{\infty}(x) + V_H(x) + V_{xc}(x), \tag{2.9}$$

where V_{∞} is the potential energy which simulates the presence of infinite potential walls located at a distance x_0 from the jellium edges (vertical dashed lines in figure 2.1) and $V_H(x)$ the electrostatic Hartree energy potential, which is the solution of Poisson's equation

$$\frac{d^2 V_H}{dx^2} = -\frac{e}{\varepsilon_0}(n_i - n_e) \tag{2.10}$$

This equation is solved numerically by using finite difference methods (for more details about the numerical methods see section 3.3).

The complexity of the many-body problem is hidden in the last term $V_{xc}(x)$. The simplest method to describe the exchange–correlation energy is to use the *local density approximation* (LDA), where commonly used the exchange energy potential (local Slater approximation reduced by a factor 2/3) is given by

$$V_x(x) = -e^2\left(\frac{3}{\pi}\right)^{\frac{1}{3}} n_e(x)^{\frac{1}{3}} \tag{2.11}$$

and the correlation energy (local Wigner formula in atomic units)

$$V_c(x) = -\frac{0.587e^2}{(r_s(x) + 7.8)^2}(r_s(x) + 5.85) \tag{2.12}$$

with $r_s(x) = (3/4\pi n_e(x))^{1/3}$. Finally $V_{xc}(x) = V_x(x) + V_c(x)$. The LDA has been used in large number of practical applications of the density functional method and is known to give good results for important quantities, such as the work function and surface energy [34]. Here, we are not interested in a detailed discussion about possible description of V_{xc}, as in our model we need a solid representation which incorporates only the most important effects.

At finite temperature the electron density is given by

$$n_e(\vec{r}) = n_e(x) \equiv \sum_{\nu} f_{\nu} |\Psi_{\nu}(\vec{r})|^2 \tag{2.13}$$

where f_ν is the Fermi-Dirac energy distribution function. We define the internal energy U as

$$U = \sum_\nu E_\nu = \sum_{\vec{k}_{\shortparallel},l} f_{\vec{k}_{\shortparallel},l} \left(\frac{\hbar^2 k_{\shortparallel}^2}{2m} + \varepsilon_l \right). \tag{2.14}$$

The Fermi-Dirac energy distribution

(a) At $T_e = 0$ K is given by

$$f_\nu = 2\Theta(E_F - E_\nu), \tag{2.15}$$

where E_F is the Fermi energy and Θ is the Heaviside function. The factor 2 in the above expression takes care of the summation over the electronic spin states. The density (2.13) can be rewritten as

$$n_e(\vec{r}) = \frac{1}{A} \sum_{\vec{k}_{\shortparallel},l} f_{\vec{k}_{\shortparallel},l} |\psi_l(x)|^2, \tag{2.16}$$

and by using the usual prescription

$$\frac{1}{A} \sum_{\vec{k}_{\shortparallel}} \rightarrow \frac{1}{(2\pi)^2} \int\limits_0^\infty dk_{\shortparallel} k_{\shortparallel} \int\limits_0^{2\pi} d\theta \tag{2.17}$$

we get ($\psi_l(x) \in \mathbb{R}$ and $\int_0^d \psi_l^2(x) dx = 1 \; \forall l$)

$$n_e(x) = \frac{m}{\pi \hbar^2} \sum_l^{occ} (E_F - \varepsilon_l) \psi_l^2(x), \tag{2.18}$$

where *occ* denotes the number of occupied states. The Fermi energy E_F is determined by the condition (charge neutrality of the system $A \int\limits_0^d n_e(x) dx = AL\overline{n}_i$)

$$\frac{m}{\pi \hbar^2} \sum_l^{occ} \Theta(E_F - \varepsilon_l)(E_F - \varepsilon_l) = L\overline{n}_i = N_s. \tag{2.19}$$

The internal energy (2.14) reads as

$$U = \left(\frac{Am}{\pi \hbar^2} \right) \frac{1}{2} \sum_l^{occ} (E_F^2 - \varepsilon_l). \tag{2.20}$$

(b) At $T_e \neq 0$ K we have

$$f_\nu = \frac{2}{e^{(E_\nu - \mu)/k_B T} + 1} \tag{2.21}$$

leading to

$$n_e(x) = \frac{m}{\pi \hbar^2 \beta} \sum_l^\infty \left[\ln(1 + e^{\beta(\varepsilon_l - \mu)}) - \beta(\varepsilon_l - \mu) \right] \psi_l^2(x), \tag{2.22}$$

and by using (2.17) to

$$U = \frac{Am}{\pi \hbar^2 \beta} \left[\frac{\pi^2}{6\beta} + \varepsilon_l \ln \left(e^{(\varepsilon_l - \mu)\beta} + 1 \right) + \frac{1}{\beta} \text{polylog}(2, -e^{(\varepsilon_l - \mu)\beta}) + \frac{\beta}{2}(\mu^2 - \varepsilon_l^2) \right] \tag{2.23}$$

where $\beta = 1/k_B T_e$ and μ is the chemical potential. The polylog(a, z) is a special function given by

$$\text{polylog}(a, z) = \sum_{j=1}^\infty \frac{z^j}{j^a}. \tag{2.24}$$

The thermal energy per particle can be defined as

$$\bar{E}_{th} = \kappa(T_e) - \kappa(0) \tag{2.25}$$

with $\kappa = K/N$ where K is the kinetic energy of a non-interacting electron gas of density $n_e(x)$. In order to calculate K, we note from (2.2) and (2.14) that

$$U = \sum_\nu f_\nu \left\langle \Psi_\nu \left| -\frac{1}{2} \nabla^2 + V_{eff}(x) \right| \Psi_\nu \right\rangle \tag{2.26}$$

leading to

$$K = U - A \int_0^d V_{eff}(x) n_e(x) dx. \tag{2.27}$$

Since the number of particles is given by $N = A \int_0^d n_e(x) dz = AL\overline{n}_i$, the internal energy per particle reads

$$u = \frac{m}{\pi \hbar^2 \beta L \overline{n}_i} \left[\frac{\pi^2}{6\beta} + \varepsilon_l \ln \left(e^{(\varepsilon_l - \mu)\beta} + 1 \right) + \frac{1}{\beta} \text{polylog}(2, -e^{(\varepsilon_l - \mu)\beta}) + \frac{\beta}{2}(\mu^2 - \varepsilon_l^2) \right] \tag{2.28}$$

and

$$\kappa = u - \frac{1}{a \overline{n}_i} \int_0^d V_{eff}(x) n_e(x) dx. \tag{2.29}$$

Let's define a degeneracy factor for the state l as

$$\overline{w}_l \equiv \frac{m}{\pi\hbar^2\beta}\left[\ln(1+e^{\beta(\varepsilon_l-\mu)}) - \beta(\varepsilon_l-\mu)\right]. \tag{2.30}$$

Using this definition one has

$$n_e(x) = \sum_l^{\infty} \overline{w}_l \psi_l^2(x). \tag{2.31}$$

For $T_e = 0$ K (2.30) reduces to

$$\overline{w}_l = \frac{m}{\pi\hbar^2}(E_F - \varepsilon_l). \tag{2.32}$$

The occupation weight for the subband l is thus given by

$$w_l = \frac{\overline{w}_l}{L\overline{n}_i}. \tag{2.33}$$

Finally, the chemical potential μ is determined by the condition (charge neutrality of the system)

$$\sum_l^{\infty} \overline{w}_l = L\overline{n}_i. \tag{2.34}$$

2.1.2 Definition of the ionic backgrounds

For simple metals, the electronic properties of a thin metal film can be described quite well within the so-called jellium model [34]. In this approximation the lattice of positive ionic charges is replaced by a uniform background defined by

$$n_i(x) = \overline{n}_i\Theta(x) \tag{2.35}$$

where $\Theta(|x| \leq L/2) = 1$ and $\Theta(|x| > L/2) = 0$. The only free parameter is the density $\overline{n}_i$.

In our calculations, however, we have considered another shape for the background (jellium model with soft edges, which is more realistic than the version with steep edges) given by

$$n_i = \overline{n}_i[1 + \exp((|x - d/2| - L/2)/\sigma_i)]^{-1}. \tag{2.36}$$

Typical ion density profiles as a function of the spatial coordinate are presented in figure 2.2. The value of the parameter σ_i determines steepness of the ion density. The higher the value of σ_i, the smoother is the transition of the density around the edges.

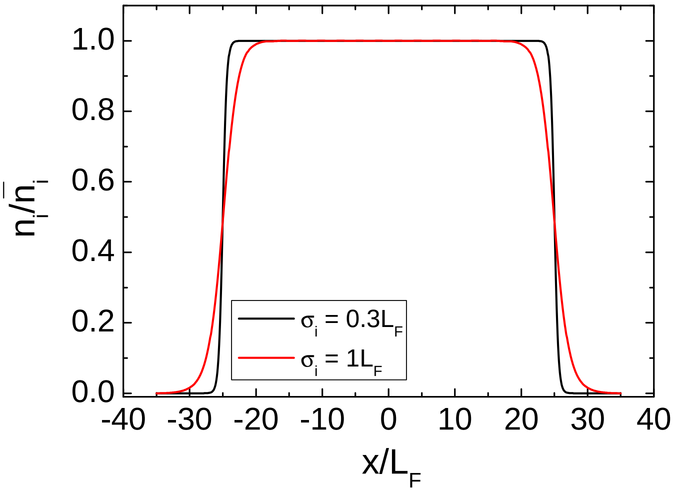

Figure 2.2: Normalized ion densities for the film of thickness $L = 50L_F \approx 6$ mn. Two different backgrounds are depicted.

For ions we have the following relation

$$\int_0^d dx n_i(x) = L\overline{n}_i = N_s. \tag{2.37}$$

2.1.3 Numerical method

The solutions of the Schrödinger equation for a one-dimensional square well potential with perfectly rigid walls ($V = 0$ for $0 < x < d$ and $V = \infty$ for $x = 0$ and $x = d$) are

$$\varphi_s(x) = \begin{cases} (2/d)^{1/2} \sin\left(\frac{s\pi}{d}x\right) & \text{for } 0 \leq x \leq d \\ 0 & \text{for } x < 0; x > d, \end{cases} \tag{2.38}$$

and

$$\varepsilon_s = \left[\frac{\hbar\pi s}{(2\pi)^{1/2} d}\right]^2. \tag{2.39}$$

According to the symmetry of our electronic system we use the following representation of the wavefunctions ψ_l, solutions of (2.8) which automatically satisfy the boundary conditions $\psi_l(x) = 0$ at $x = 0$ and $x = d$:

$$\psi_l(x) = \left(\frac{2}{d}\right)^{1/2} \sum_{s=1}^{\infty} a_s^{(l)} \sin\left(\frac{s\pi}{d}x\right). \tag{2.40}$$

Substituting (2.40) in (2.8), we obtain the following matrix equation

$$\sum_{k'}^{\infty} M_k^{k'} a_{k'}^{(l)} = \epsilon_l a_k^{(l)} \quad \text{for} \quad k = 1, 2, 3, ... \tag{2.41}$$

Practically, the above sum is performed only up to k'_{max}. The matrix M has the following expression

$$M_k^{k'} = \frac{\hbar}{2m}\left(\frac{k\pi}{d}\right)^2 \delta_k^{k'} + M_k^{k'(H)} + M_k^{k'(xc)} \tag{2.42}$$

with

$$M_k^{k'(H)} = \frac{4\pi e^2}{d} \int_0^d dx [n_e(x) - n_i(x)] I_k^{k'}(x) \tag{2.43}$$

and

$$M_k^{k'(xc)} = \frac{2}{d} \int_0^d dx V_{xc}(x) \sin\left(\frac{k\pi}{d}z\right) \sin\left(\frac{k'\pi}{d}z\right). \tag{2.44}$$

The above integrals have to be evaluated numerically. The explicit form of $I_k^{k'}(x)$ in (2.43) is given by

$$I_k^{k'}(x) = \frac{1}{2}[I_k^{k'(+)}(x) - I_k^{k'(-)}(x)] \tag{2.45}$$

where

$$I_k^{k'(+)}(x) = \frac{d^2}{\pi^2(k+k')}\left[1 + (-1)^{k+k'} - 2\cos\left[(k+k')\frac{\pi}{d}x\right]\right] \tag{2.46}$$

and

$$I_k^{k'(-)}(x) = \delta_k^{k'}\left[z^2 - zd + \frac{d^2}{2}\right] + (1 - \delta_k^{k'})\frac{d^2}{\pi^2(k-k')^2}\left[1 + (-1)^{k+k'} - 2\cos\left[(k-k')\frac{\pi}{d}x\right]\right]. \tag{2.47}$$

The Kohn–Sham procedure consists of solving equations (2.8, 2.9, 2.13) self-consistently. During each step of our numerical procedure, the equation (2.8) is solved using its matrix form (2.41) and the chemical potential μ is determined by requiring the conservation of the total number of electrons form equation (2.34). The two free parameters: k'_{max} the maximum number of matrix elements, and x_0, does not alters the final results for reasonable choices. For the slab of thickness $L = 50L_F$ the values of the free parameters are $x_0 = 10L_F$ and $k'_{max} = 23$. It has been checked that other reasonable choices of those parameters gives exactly the same solutions.

2.1.4 Solution of the Kohn–Sham equations

In this section we shortly describe the main results of our ground-state construction based on the resolution of the Kohn–Sham equation in the thin film symmetry (which we shall use to compute the Wigner function). We concentrate here on the thin sodium films ($r_s = 4a_0$ where $a_0 = 0.529\text{Å}$), for which the valence electrons are fully delocalized and the influence of the core electrons can be neglected. (We express all quantities in terms of a few normalized units, which will be described in the next chapter.)

In figure 2.3 we show the effective potential V_{eff} with and without exchange–correlation part for several thicknesses of the film. With increasing size of the film, we take into consideration more and more states, and the potential profiles becomes broader. Without V_{xc}, the potential falls less rapidly, and its minimum is situated at the center of the film. As it can be clearly seen on the picture V_{xc} gives more confinement to the system.

The normalized electron density $n_e/\overline{n}_i$ for different temperatures is presented in figure 2.4. The profile reveals slowly decaying Friedel oscillations, which correspond to a rippling pattern of electrons around the positive ion density. This effect is the consequence of the quantum nature of the electrons. In quantum mechanics the negative charge is not sitting at exactly one spot, but is "smeared out" over a region of space. The size of this region is characterized by the electron wavelength λ. For an electron gas only electrons with energy near the Fermi energy can participate in the screening process and $\lambda = \lambda_F$ where $\lambda_F = 2\pi/k_F$ with k_F representing Fermi wave vector. Negative electrons are initially pulled strongly toward the surface. This determines the charge density not just at the surface, but also for the distance after it. The charge density that is correct for the surface becomes too strong for further distances, and sets up a cycle of overcompensation and correction of the electron density, with gradually decreasing amplitude.

The amplitude of the Friedel oscillations weakly depends on the electron temperature. The reason of this effect can be explained by a wide range of electron wavelengths λ at higher temperatures. If we increase the temperature of the system the new states become available for the electrons. As the electrons jump to these states their energy increase and their wavelengths decrease. The quantum interference of the electrons with different λ causes the lowering of the oscillation's amplitude, and with increasing temperature the system becomes more classical (no oscillation at all).

The actual wavelength of the observed Friedel oscillations is equal $\lambda_F/2$ instead of

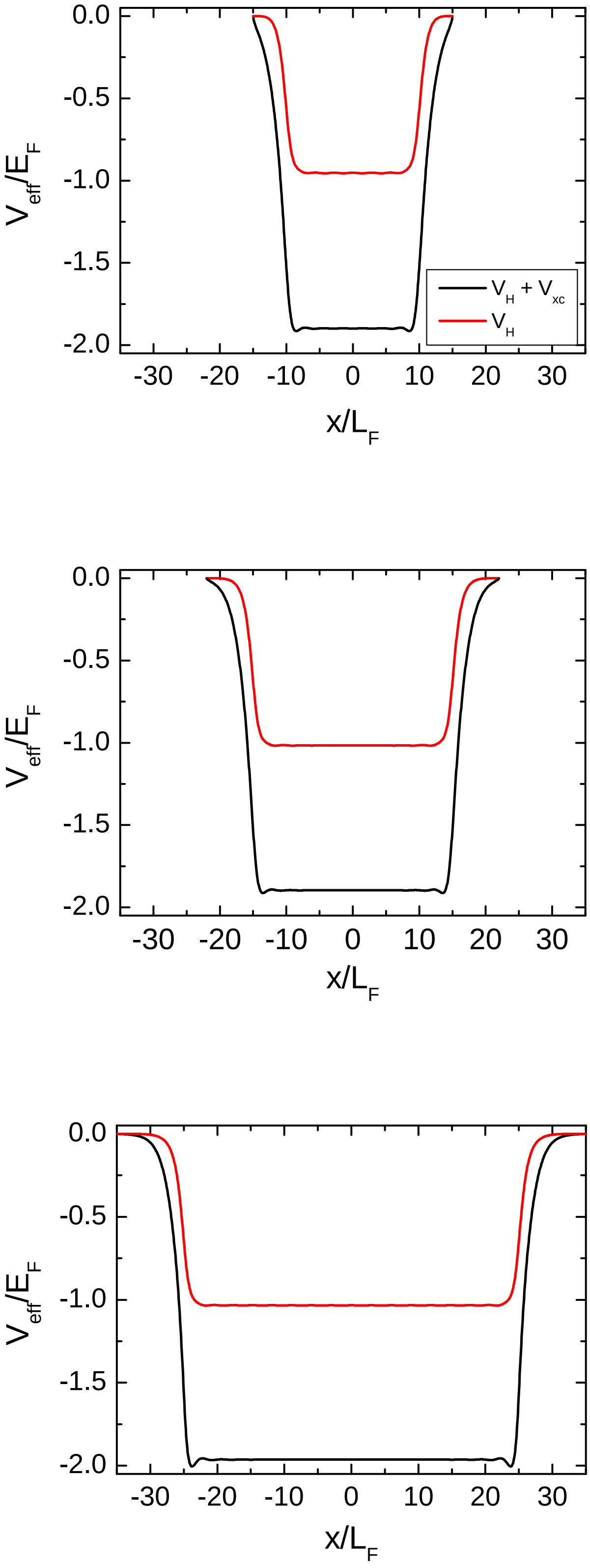

Figure 2.3: Effective and Hartree potentials for three films of thickness: $L = 20L_F$, $L = 30L_F$, and $L = 50L_F$.

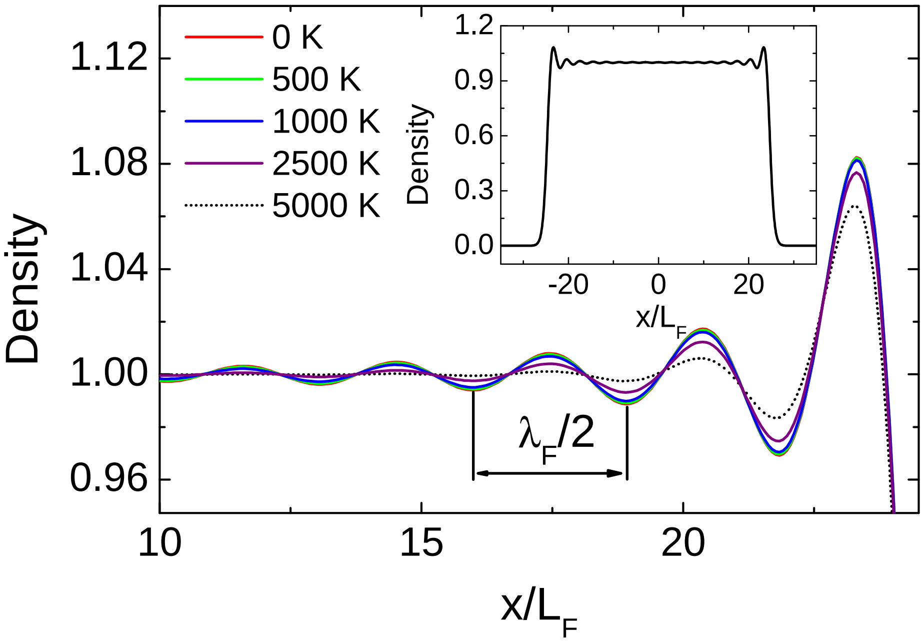

Figure 2.4: Normalized density profile near the edge of the slab of thickness $50L_F$ for different temperatures. The inset shows complete profile at $T_e = 0$ K.

λ_F. The reason for the discrepancy comes from thinking about one wavelength of the electron as a single "lump" of density. In reality, since the density of the electron n_e is proportional to the wave amplitude squared ($n_e \sim \psi^2$), each wavelength corresponds to two density "lumps". So each electron consists of two density lumps, and a resultant charge density oscillates with half-wavelength of the screening electrons [35].

Typical examples of the solution of the Kohn–Sham equation are presented in figure 2.5. At the absolute zero temperature, starting with the empty system, the electrons start filling the bottom unoccupied quantum states and continue occupying higher levels until all electrons are accommodated. The topmost filled level in the ground-state determines the Fermi energy. As the temperature is increased the kinetic energy is also increased and some energy levels which were vacant at $T_e = 0$ K are now accessible for the electrons. The probability of filling the high energy states increases with the temperature.

The computed electron density given by (2.22) together with the weighted subbands densities are presented in figure 2.6. The profiles, for two films of thickness $L = 50L_F$

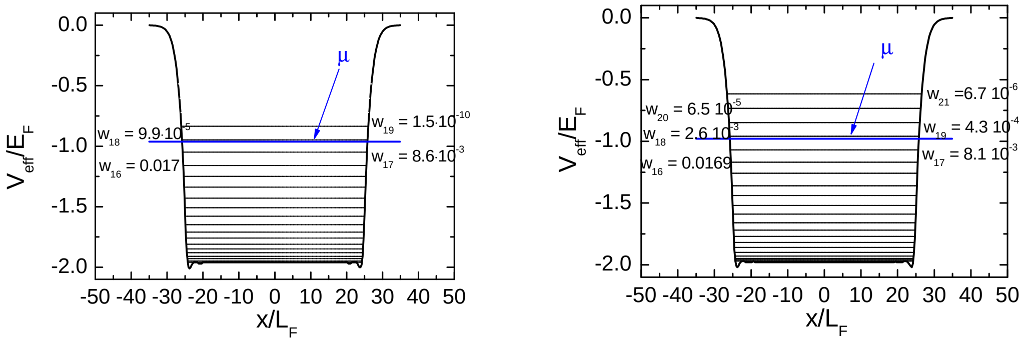

Figure 2.5: Effective potential with the energy levels at $T_e = 300$ K (left) and $T_e = 2000$ K (right) for $L = 50L_F$. The occupation probability of high energy subbands increases with temperature.

and $L = 20L_F$, were calculated self-consistently with and without V_{xc}, respectively. The density profiles in the interior exhibit slowly decaying Friedel oscillation. However, the density shape in the absence of the exchange–correlation potential shows the ripples of smaller amplitude.

The width of the electron density profiles clearly becomes boarder with increasing L, as we need to include more states for larger film. Subbands densities for the two thickness of the films (see for example n_1) differ quite significantly because the occupation weights w_l are considerably smaller if we have more states (the sum is always equal to $\sum w_l = 1$).

2.2 Wigner function in slab geometry

Having computed N Kohn–Sham wavefunctions ψ_l and respective occupation numbers w_l we can construct the ground-state Wigner function $f(x, v)$.

Following the definition (1.17) the Wigner function can be written as a sum of individual Wigner function taken with compatible weight $f(x, v) = \sum_l w_l f_l(x, v)$. Each of the partial Wigner function f_l corresponds to the suitable wavefunctions ψ_l of the ground-state. As an illustration, some typical ground-state wavefunctions and the corresponding partial Wigner functions, for a film of thickness $L = 50L_F$, are shown in figure 2.7. First plot shows Wigner function for the state $l = 1$. As it can be seen that the partial Wigner distribution is peaked at the center $x = v = 0$, and near the main

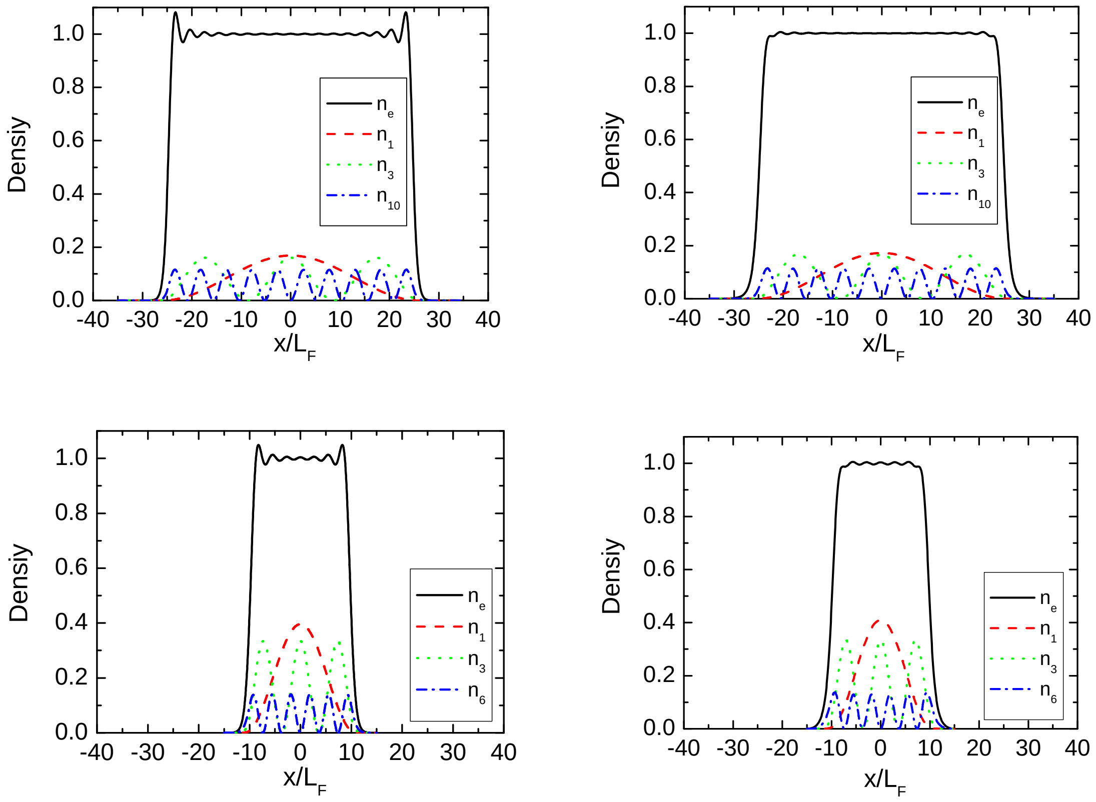

Figure 2.6: Electron density (at $T_e = 300$ K) with exchange–correlation potential (left panels) and for pure Hartree potential (right panels), for two thicknesses of the film: $L = 50L_F$ (top) and $L = 20L_F$ (bottom). The electron density is the sum of weighted subbands densities $n_e = \sum n_l$, given by $n_l = w_l \psi_l^2$.

peak we can also observe disappearing ripples where Wigner function takes negative value. This feature of the Wigner distribution becomes even more clear for the 2nd eigenstate, which besides of four peaks with positive value, have also one big negative peak. For higher subbands Wigner function becomes strongly oscillating.

An example of the total Wigner function is presented in figure 2.8. A good test of this construction is comparing the spatial density obtained from integrating the distribution function over the velocity coordinates with those given by the sum of the square of wavefunctions (2.22) (that is to check the relation (1.18)). As we can see in figure 2.8 there is no difference between the two curves and it constitutes a direct confirmation that this procedure is correct.

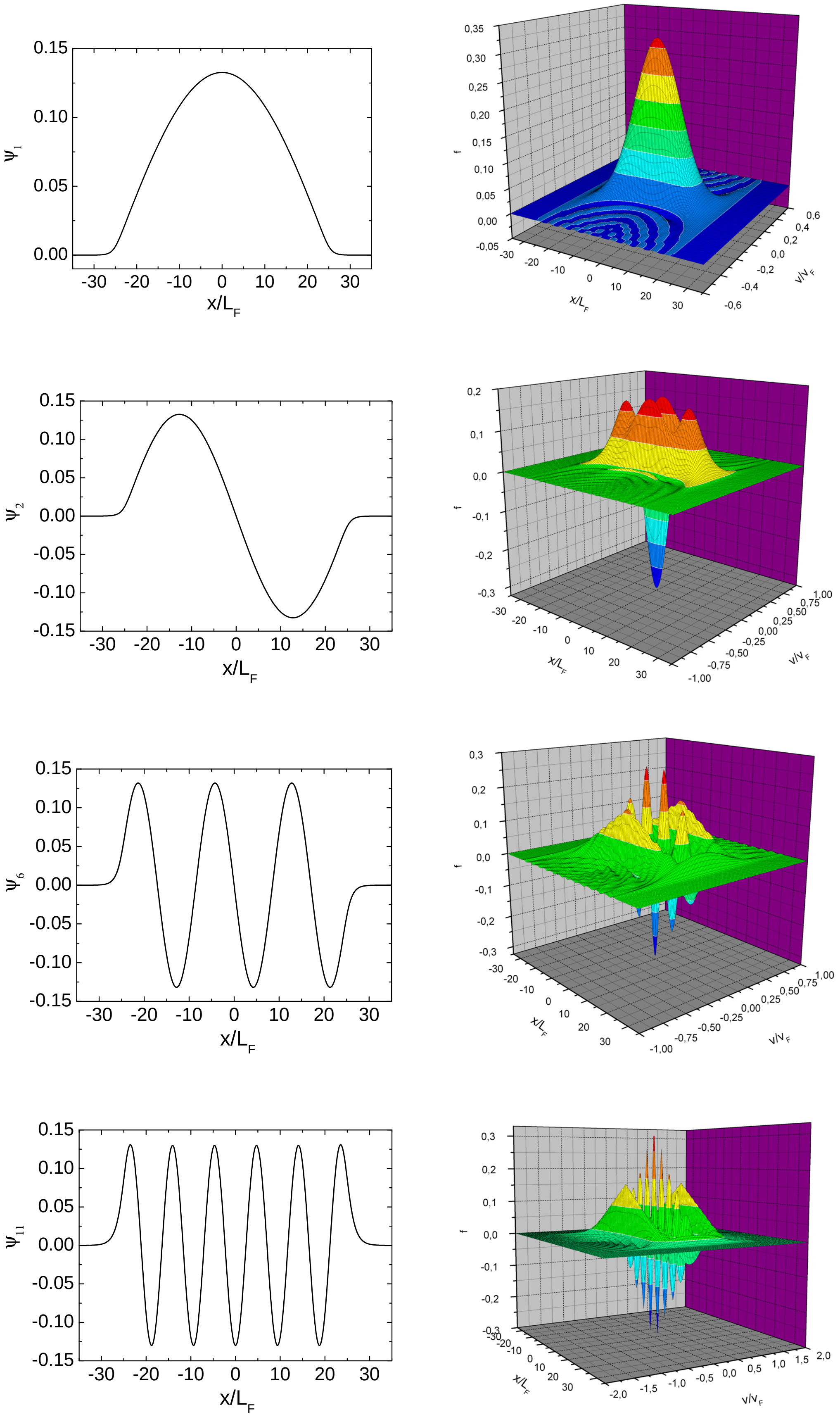

Figure 2.7: Individual Wigner function at $T_e = 300$ K with corresponding them wave function for respectively, 1st state, 2nd state, 6th state, 11th state.

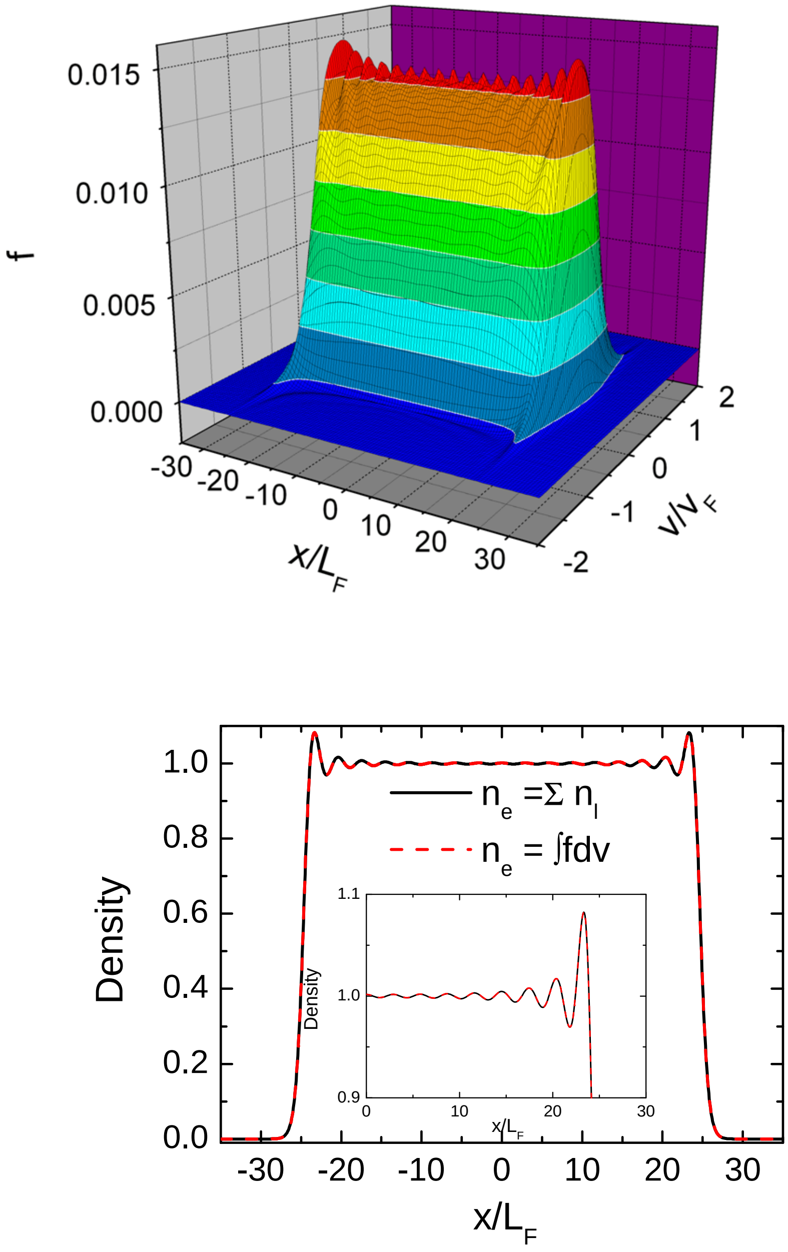

Figure 2.8: Total Wigner function at $T_e = 300$ K (top panel). Below, the normalized spatial density as sum of square wave functions (black line) and after integrating Wigner function (red dashed line). The inset shows the zoom near the film edge.

2.3 Initial state for the Vlasov model

At a given temperature T_e, which is generally much smaller than the Fermi temperature T_F, the relevant equilibrium for electrons is given by the quantum Fermi–Dirac distribution [36]. Although the Vlasov model (described in Section 1.2.2) constitutes a classical representation, the initial (Fermi–Dirac function) condition we use to evaluate the electron dynamics lies deeply in the quantum regime. In this sense, the Vlasov model can be considered as semiclassical (classical dynamics, but quantum statistics at equilibrium).

As was previously described we have adopted a 1D geometry to describe the electron dynamics. However, at thermodynamic equilibrium, the electrons should be allowed to occupy all available states in velocity space, and there is no reason why states with $v_y \neq 0$ and $v_z \neq 0$ shouldn't be occupied. Therefore, even in 1D model, the equilibrium distribution should always be described by a three-dimensional Fermi-Dirac distribution

$$f_0(x, \mathbf{v}) = \text{const} \times \frac{1}{1 + e^{\beta(\varepsilon - \mu)}}, \tag{2.48}$$

where $\varepsilon = m|\mathbf{v}|^2/2 - eV_H(x)$ is the single-particle energy ($\mathbf{v}$ is the 3D velocity vector). The chemical potential $\mu(T)$ is determined by $\int f_0 dv = n_0$, where n_0 is the equilibrium density.

It is still possible to keep the 1D geometry provided that we use the 3D Fermi-Dirac distribution (2.48) projected on the v_x axis $f_0(x, v_x) = \int\int f_0(x, \mathbf{v}) dv_y dv_z$. This integral automatically yields (with the correct multiplicative constant)

$$f_0(x, v_x) = \frac{3}{4} \frac{n_e}{v_F} \frac{T_e}{T_F} \ln\left(1 + e^{-\beta(\varepsilon - \mu)}\right), \tag{2.49}$$

with $\varepsilon(x, v_x) = mv_x^2/2 - eV_H(x)$. At zero temperature the above expression takes the form

$$f_0^{T_e=0}(x, v_x) = \tfrac{3}{4}\tfrac{n_e}{v_F}\left(1 - \tfrac{\varepsilon}{E_F}\right) \quad \text{for } |v_x| < v_F \tag{2.50}$$

and $f_0^{T_e=0} = 0$, for $|v_x| > v_F$ (in the following we assume $v = v_x$).

The electrostatic potential is obtained self-consistently from the solution of the Possion's equation

$$\frac{\partial^2 V_H}{\partial x^2} = -\frac{e}{\varepsilon_0}[n_i(x) - n_e(V_H(x))]. \tag{2.51}$$

The nonlinear Poisson equation is solved with boundary conditions $V_H'(0) = V_H'(d) = 0$ which corresponds to zero electric field at the boundaries. These boundary conditions imply that the total electric charge in the interval $[0, d]$ vanishes, i.e. $\int n_e dx = \int n_i dx$.

2.4 Ground-state properties

Typical density profiles for the equilibrium electron distribution are shown in figure 2.9. The semiclassical VP model yields a smooth density profile (without oscillations – representing continuous energy spectrum). In the quantum regime (WP) we observe the usual Friedel oscillations, which are particularly important near the edges of the film.

The ground-state thermal energy per particle $\bar{E}_{th}$, given by (2.25), as function of the square of the electron temperature is presented in figure 2.10. The Wigner and Vlasov results are almost identical and close to the theoretical value represented by a solid line. The theoretical curve corresponds to the estimation for a Fermi gas (1D bulk system) at low temperature given by $\bar{E}_{th} = C(T_e/T_F)^2$, with $C = \pi^2/12$ [37]. This estimation is only valid for temperatures $T_e \ll T_F$. This is why we observe differences between the theoretical prediction and our results at higher temperatures. Another possible explanation for this difference may be related to the fact that we are dealing with a finite-size electron system, whereas the theoretical approximation was obtained for an infinite electron gas.

Another ground-state property which we would like to investigate is the chemical

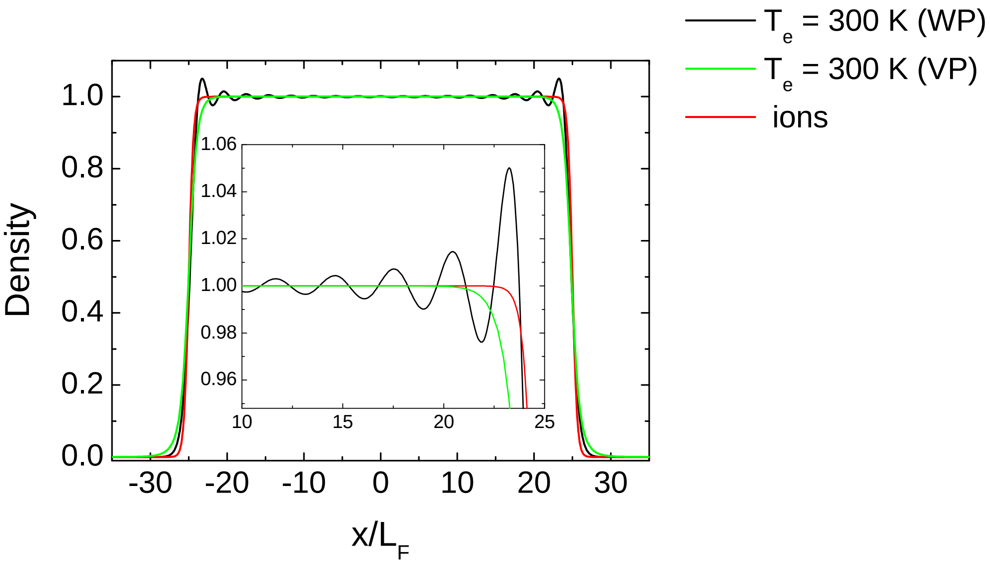

Figure 2.9: Ground-state electron densities in the semiclassical (VP) and quantum (WP) models. The inset shows a zoom near the film edge.

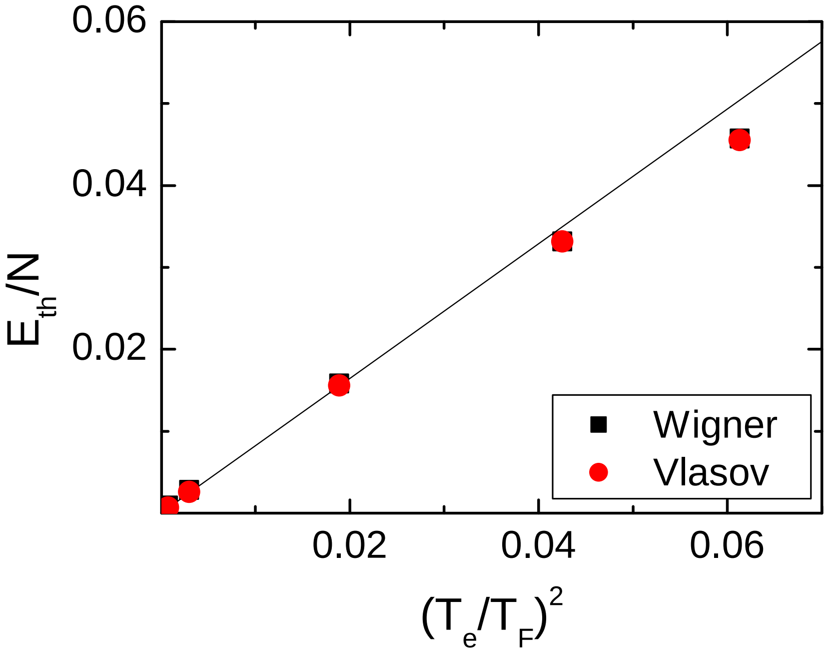

Figure 2.10: Thermal energy per particle as a function of $(T_e/T_F)^2$. The solid line corresponds to the theoretical value for the bulk at low temperature.

potential μ, shown in figure 2.11. The value of this quantity in the Wigner and Vlasov models is quite similar for all considered temperatures, and close to the exact theoretical result (here valid for all temperatures) obtained for a Fermi gas in three dimensions. The exact value of the chemical potential μ is solution of the equation

$$g\left(-\beta\mu, \frac{d-2}{2}\right) = \alpha_B \tag{2.52}$$

with

$$g(-\beta\mu, \rho) = \frac{1}{\Gamma(\rho+1)} \int\limits_0^\infty \frac{z^\rho dz}{e^{-\beta\mu+z}+1} \tag{2.53}$$

where Γ is the Gamma function and

$$\alpha_B \equiv e^{\beta\mu_B} = \frac{1}{2}\overline{n}_i \lambda_T^d \tag{2.54}$$

where μ_B is the Boltzmann chemical potential and λ_T is the thermal wave length defined by $\lambda_T = \left(\frac{2\pi\hbar^2}{mk_BT_e}\right)^{1/2}$.

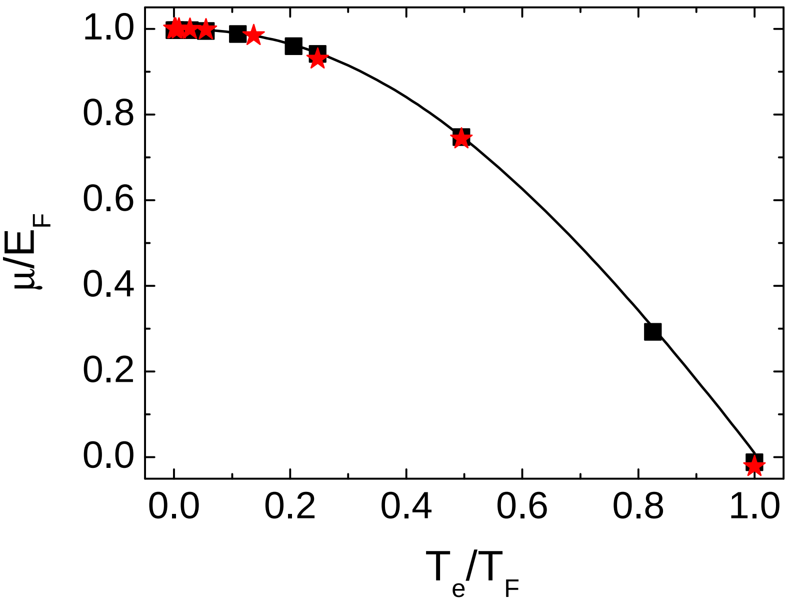

Figure 2.11: Chemical potential as a function of the electron temperature for the Wigner (black squares) and Vlasov (red stars) ground-states. The continuous line represents the theoretical results for the bulk.

Another interesting quantity is the statistical entropy of the ground-state. We present here only the results for the quantum regime as there is no easy way to get similar results for the classical representation.

Let us consider the statistical entropy [37]

$$S = -k_B \sum_{\nu} f_\nu \ln(f_\nu) + (1 - f_\nu) \ln(1 - f_\nu). \tag{2.55}$$

By using (2.17, 2.21) we obtain

$$S = \frac{k_B m A}{\pi \hbar^2 \beta} \sum_l \left[\mathrm{dilog}\left(\frac{e^{\beta(\varepsilon_l - \mu)}}{e^{\beta(\varepsilon_l - \mu)} + 1} \right) + \frac{\pi^2}{6} + \mathrm{dilog}(e^{\beta(\varepsilon_l - \mu)} + 1) + \frac{1}{2} \ln(e^{\beta(\varepsilon_l - \mu)} + 1)^2 \right]. \tag{2.56}$$

where $\mathrm{dilog}(x) = \int_1^x \frac{\ln(t)}{1-t} dt$. The entropy per particle $\overline{S}$ is obtained by dividing S by the total number of particles $N = aA\overline{n}_i$. Figure 2.12 shows the statistical entropy per particle as a function of the temperature. With increasing temperature more states with appreciable probability are available for the system leading to an increase of the entropy.

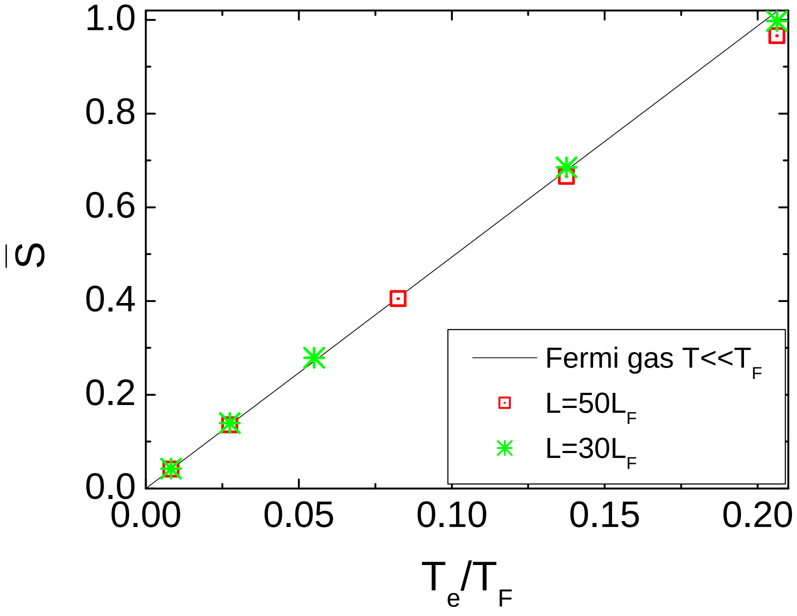

Figure 2.12: Statistical entropy as a function of the temperature for different sizes of the films. The continuous line represents the theoretical results for the bulk at low temperature.

The theoretical estimate for an infinite Fermi gas at low temperature ($T_e \ll T_F$) yields a linear dependence

$$\overline{S} = \frac{2c}{\beta} \tag{2.57}$$

where $c = 1/2(2\pi/3)^{4/3}r_s^2$. As can be clearly seen from figure 2.12 theoretical estimates fit very well the numerical results. Once again we observe that the properties of the electron gas confined in the thin film are very close to those of an infinite Fermi gas.

The ground-state properties presented in this section aimed to understand whether the standard bulk properties apply to finite-size systems. As we have seen they do apply especially well at low temperatures. Although the results for chemical potential agree rather well for both quantum and semiclassical calculations, in cases of the thermal energy and the statistical entropy we can see some little discrepancy in the high temperature limit. Despite this small deviation, the thermodynamical properties of the electron gas in the film are in good accordance with those of an infinite noninteracting fermions. It may seem that the presence of the surfaces does not play a crucial role in determining ground-state properties, however we need to be careful when we turn into dynamical properties. The fact that bulk theory represents quite adequately the ground-state characteristic, does not guarantee that it will work equally well in time-dependent circumstances. As we will see in Chapter 4, the presence of the surfaces is of paramount importance for dynamical phenomena.

Chapter 3

Dynamical models and numerical methods

The calculation of the ground state structure is just a preliminary step to describe the nonlinear dynamics in thin metal films. In this chapter we will provide more details on the mathematical structure of our dynamical models and on the numerical techniques used so solve the relevant equations. Subsequently we will validate our Wigner approach by comparing results of the Wigner model to those obtained with DFT in the linear regime.

3.1 Normalized units

In this work all quantities are expressed in terms of a few normalized units that represent typical velocity, time and length scales for an electron gas. These quantities are commonly used in the plasmas physics as well as the kinetic equations which we use to evaluate the electron dynamics.

Plasma physics is not so far away form the world of nanoparticles [32], which can be easily explained by the following arguments. Valence electrons in metals are not attached to one atom but are shared throughout the lattice. They give rise to a gas of electrons, neutralized by the atomic positive ions. Although, some level of understanding of metallic properties can be obtained by considering noninteracting electrons, a more accurate description can be worked out by treating the electron population as a plasma, globally neutralized by the lattice ions.

For ordinary metals, however, the presence of a regular ion lattice determines most of the properties of the electron population (i.e. band structure, thermodynamics properties) and typical plasma effects constitute only a higher order correction. Thanks to the tremendous progress in the manipulation of metallic nanostructures, it is now possible to produce particles composed of a small number of atoms. For such objects, no underlying regular ionic lattice exists, so that the dynamics of the electron population is principally governed by plasma effects, at least for large enough system. Also the development of ultrafast laser sources makes it possible to probe the electron dynamics in metallic nanostructures on the typical time scale of plasma phenomena. By virtue of these argument metallic nanostructures constitute an ideal area to study the dynamical properties of quantum plasmas.

3.1.1 Time scales

Let us consider a globally neutral plasma of number density n, composed of electrons with mass m and fixed ions, interacting by the Coulomb forces. Now, if the density of the electrons in one region is increased (thus creating a net negative charge), they will repel each other and in addition they will be pulled back by the positive charge they left behind. As the electrons move backwards to their initial configuration they pick up kinetic energy, and instead of just coming to rest in their equilibrium configuration, they overshoot the mark, and travel further. In the absence of collisions this process gives rise to the oscillation of electron population at the plasma frequency ω_p.

It can be easily shown that ω_p corresponds to the typical electrostatic oscillation frequency of charged particles in response to a small charge separation [38]. Let us consider a one-dimensional situation in which we have a slab consisting of electrons residing in the sea of positive ions. Let us suppose that the entire electron population is displaced from its equilibrium position by an infinitesimal distance δx (schematically presented in figure 3.1). Since the electrons have been displaced (we can neglect ionic motion as they are much heavier than electrons) their density will also change. The resulting change in charge density which develops on the leading face of the slab is $\sigma = en\delta x$. An equal and opposite charge density develops on the opposite face. The x–directed electric field generated inside the slab is of magnitude $E_x = -\sigma/\varepsilon_0 = -en\delta x/\varepsilon_0$. The force on an electron in the displaced position is $F_x = eE_x = -e^2 n\delta x/\varepsilon_0$ a restoring force proportional to the displacement δx of the electron. This lead to the harmonical

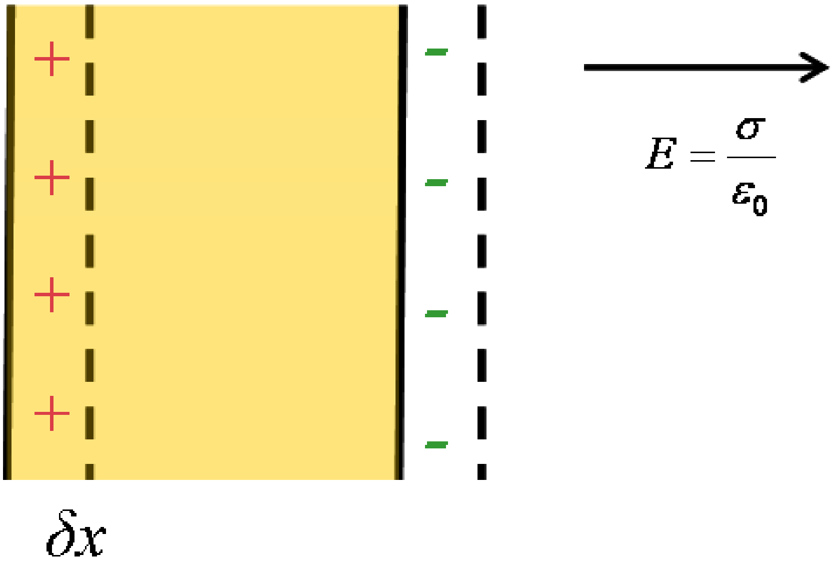

Figure 3.1: A schematic representation of electrons displacement.

oscillations of the electrons. The equation of motion of a displaced electron is

$$m\frac{d^2\delta x}{dt^2} = -\frac{e^2 n}{\varepsilon_0}\delta x \tag{3.1}$$

taking $\delta x = (\delta x)_0 e^{i\omega_p t}$ we find that a disturbance of a plasma will set up free oscillation of the electrons about their equilibrium position at the frequency:

$$\omega_p = \left(\frac{e^2 n}{m\varepsilon_0}\right)^{1/2}. \tag{3.2}$$

Because ω_p represents the typical oscillation frequency for electrons immersed in a neutralizing background of positive ions, the time scale in our model is normalized to the inverse of the plasma frequency ω_p^{-1}.

3.1.2 Debye shielding

Another fundamental characteristic of the behavior of a plasma is its ability of shielding every charge in the plasma by a cloud of oppositely charged particles. When we put some excess positive charge into the plasma, it will be rapidly surrounded by a cloud of electrons. Screening can be calculated using Poisson's equation with the source terms being the additional charge and its associated cloud [27]:

$$\nabla^2\phi = -\frac{1}{\varepsilon_0}\left[q_{ex}\delta(r) + \sum_\sigma n_\sigma(r)q_\sigma\right] \tag{3.3}$$

where the term $q_{ex}\delta(r)$ represents the excessive charge and $\sum n_{\sigma=i,e}(r)q_\sigma$ describes the charge density of all plasma particles that participate in the screening. Before the additional charge was inserted this term vanished because the plasma was assumed to be initially neutral. If plasma is sufficiently close to the thermal equilibrium, its particle densities are distributed according to the Maxwell-Boltzmann law $n_\sigma = n_{\sigma 0}\exp(-q_\sigma\phi/k_BT_\sigma)$. Furthermore, because the perturbation due to excessive particle is infinitesimal, we can safely assume that $|q_\sigma\phi| \ll k_BT_\sigma$, in which case we can expand the exponential in a Taylor series so the density becomes simply $n_\sigma \approx n_{\sigma 0}(1 - q_\sigma\phi/k_BT_\sigma)$. The assumption of initial neutrality means that $\sum_\sigma n_{\sigma 0}q_\sigma = 0$, thus (3.3) reduces to

$$\nabla^2\phi - \frac{1}{L_D^2}\phi = -\frac{q_{ex}}{\varepsilon_0}\delta(r) \tag{3.4}$$

and the effective Debye length can be defined as

$$\frac{1}{L_D^2} = \sum_\sigma \frac{1}{L_\sigma^2}$$

where L_σ represents the species Debye length. After substituting $q_i = -q_e = e$ and $n_{i0} = n_{e0} = n$ we can write the Debye length in the form:

$$L_D = \left(\frac{\varepsilon_0 k_B T}{ne^2}\right)^2. \tag{3.5}$$

Equation (3.4) can be solved using standard mathematical techniques and gives

$$\phi(r) = \frac{e}{4\pi\varepsilon_0 r}\exp(-r/L_D). \tag{3.6}$$

For $r \ll L_D$ the potential $\phi(r)$ is identical to the potential of an additional charge in vacuum whereas for $r \gg L_D$ the extra charge is completely screened by its surrounding shielding cloud. The nominal radius of the shielding cloud is L_D. Because the supplementary particle is completely screened for $r \gg L_D$, the total shielding cloud charge is equal in magnitude to the charge on the additional particle and opposite in sign.

3.1.3 Length and velocity scales in quantum regime

When quantum effects start playing a role, the above picture gets more complicated and new parameters become important. One of the most relevant parameter in this case is the de Broglie wavelength of the charged particles

$$\lambda_B = \frac{\hbar}{m v_T}, \tag{3.7}$$

where $v_T = (k_B T/m)^{1/2}$ represents the thermal velocity due to random thermal motion. The de Broglie wavelength roughly represents spatial extension of the particle wave function and the larger it is the more important quantum effect are. For ions, for example, the de Broglie wavelength is much smaller that for electrons because of the large mass difference, and in all practical situation the ion dynamics is treated classically.

For classical regimes, the de Broglie wavelength is so small that the particles can be considered as pointlike, therefore there is no overlapping of wave functions and no quantum interference. On this basis, it is reasonable to postulate that quantum effects start playing a significant role when the de Broglie wavelength is similar or larger than the average interparticle distance $n^{-1/3}$, i.e. when

$$n\lambda_B^3 \geq 1 \tag{3.8}$$

On the other hand, quantum effect became important when the temperature is lower than the so-called Fermi temperature T_F, defined as

$$k_B T_F \equiv E_F = \frac{\hbar^2}{2m}(3\pi^2)^{2/3} n^{2/3}. \tag{3.9}$$

When T approaches T_F, the relevant statistical distribution changes from Fermi-Dirac to Maxwell-Boltzmann and we can define the degeneracy parameter as $\chi = T_F/T$. It can be also noted that χ is simply related to the dimensionless parameter $n\lambda_B^3$ discussed above:

$$\chi \equiv \frac{T_F}{T} = \frac{1}{2}(3\pi^2)^{2/3}(n\lambda_B^3)^{2/3}. \tag{3.10}$$

Considering the quantum time scale for collective phenomena, this is still given by the inverse of the plasma frequency (3.2). The thermal speed becomes meaningless in the very low temperature limit, and should be replaced by the typical velocity characterizing a Fermi-Dirac distribution. This is the Fermi velocity:

$$v_F = \left(\frac{2E_F}{m}\right)^{1/2} = \frac{\hbar}{m}(3\pi^2 n)^{1/3}. \tag{3.11}$$

With the plasma frequency and the Fermi velocity, we can define a typical length scale

$$L_F = \frac{v_F}{\omega_p}, \tag{3.12}$$

Table 3.1: Typical parameter for gold and sodium films

	Units	Au	Na
$\bar{n}_i$	m^{-3}	5.9×10^{28}	2.5×10^{28}
ω_p^{-1}	fs	0.07	0.11
$\hbar\omega_p$	eV	9.02	5.87
E_F	eV	5.53	3.12
T_F	T	6.4×10^4	3.6×10^4
L_F	nm	0.09	0.12
v_F	ms^{-1}	1.39×10^6	1.05×10^6
r_s	nm	0.16	0.21
r_s/a_0	-	3.01	4.0

which is a quantum analog of the Debye length ($L_D = v_T/\omega_p$). Just like the Debye length, L_F describes the length scale of electrostatic screening in a quantum plasma.

In summary, the basic units used in our model are as follows:

- Time is normalized to the inverse of the plasmon frequency ω_p.
- Velocities are normalized to the Fermi speed v_F.
- Distances are expressed in units of the Thomas–Fermi screening length L_F.

In addition, particles densities are normalized to the ion density of the bulk metal $\bar{n}_i$.

For alkali metals we have $L_F = 0.59(r_s/a_0)$Å, $\omega_p^{-1} = 1.22 \cdot 10^{-2}(r_s/a_0)^{3/2}$fs, $E_F = 50.11(r_s/a_0)^{-2}$eV, and $T_F = 5.82 \cdot 10^5(r_s/a_0)^{-2}$ K, where r_s is the Wigner-Seitz radius and for sodium, $r_s = 4a_0$ (a_0 stands for Bohr radius). The principal physical parameters for sodium and gold films are summarized in table 3.1.

3.2 Classical and quantum dynamical models

The most fundamental model for the quantum N-body problem is the Schrödinger equation for the N-particle wave function $\psi(x_1, x_2, ...x_N, t)$. Obviously, this is an unrealistic task, both for analytical calculations and numerical simulations. A drastic, but useful and to some extent plausible simplification can be achieved by neglecting two-body (or higher order) correlations. In the framework of this mean-field approximation each electron moves independently of all the others except that it feels the Coulomb repulsion due to the average positions of all electrons. This amounts to assume that the N-body wave function can be factored into the product of N one-body functions:

$$\psi(x_1, x_2, ...x_n, t) = \psi_1(x_1, t)\psi_2(x_2, t)...\psi_N(x_N, t). \tag{3.13}$$

For fermions, a weak form of the exclusion principle is satisfied if none of the wave function on the right-hand-side of (3.13) are identical.

The evolution of the electrons in metallic nanostructures can be described by quantum mean-field models, like for example, the time-dependent Hartree equation. Mean-field models take into account collective effects due to the global electric charge distribution, but neglect two-body correlations. This is a fairly reasonable assumption for highly degenerate electron gases in metallic nanostructures at room temperature, as the exclusion principle forbids a vast number of transitions that would otherwise be possible.

The set of N one-body wave functions is known as a quantum mixture (or quantum mixed state) and usually represented by a density matrix

$$\rho(x, y, t) = \sum_{i=1}^{N} w_i \psi_i(x, t)\psi_i^*(y, t), \tag{3.14}$$

where we have assumed the same normalization $\int |\psi_i|^2 dx = 1$ for all wave functions and then introduced occupation probabilities w_i.

In order to evaluate the electron dynamics in thin metal films we use the Wigner model based on the density matrix formalism (Von Neumann equation)

$$i\hbar \frac{\rho(t)}{dt} = [H(t), \rho(t)], \tag{3.15}$$

which is equivalent to the Wigner equation

$$\begin{aligned} &\frac{\partial f}{\partial t} + v\frac{\partial f}{\partial x} + \qquad (3.16)\\ &\frac{em}{2i\pi\hbar^2} \int\int d\lambda dv' e^{im(v-v')\lambda/\hbar} \left[V_{eff}\left(x + \frac{\lambda}{2}\right) - V_{eff}\left(x - \frac{\lambda}{2}\right)\right] f(x, v', t) = 0 \end{aligned}$$

where V_{eff} is composed of a Hartree and an exchange–correlation part. For the exchange and correlation potential we employ the adiabatic local-density approximation, i.e. we use the same functional as in the ground-state calculation (described in more details in Chapter 2), but allow for a time dependence of the electron density. The Hartree potential also includes the effects of the ions (represented in the framework of the jellium model, by a continuous, immobile density), and satisfies Poisson's equation

$$\frac{\partial^2 V_H}{\partial x^2} = \frac{e}{\varepsilon_0}\left(\int f dv - n_i\right). \tag{3.17}$$

In the classical limit (by taking $\hbar \to 0$ and neglecting exchange and correlation), equation (3.17) reduces to the Vlasov equation

$$\frac{\partial f}{\partial t} + v\frac{\partial f}{\partial x} + \frac{e}{m}\frac{\partial V_{eff}}{\partial x}\frac{\partial f}{\partial v} = 0. \tag{3.18}$$

3.3 Numerical method

The equations (3.17), and (3.18) coupled to Poisson's equation for the electrical potential

$$\frac{\partial^2 V}{\partial x^2} = -\frac{e}{\varepsilon_0}[n_i(x) - n_e(x,t)] \equiv \frac{\rho}{\varepsilon_0}, \tag{3.19}$$

constitute a nonlinear self-consistent system, as the electric potential determines f and is in turn determined by it in equation (3.19).

The method of solving of Poisson equation is based on finite–difference approach in which the solution of differential equation is approximated by linear combinations of function values at the grid points

$$\frac{V_{j-1} - 2V_j + V_{j+1}}{\Delta x^2} = -\frac{\rho_j}{\varepsilon_0}. \tag{3.20}$$

The above equation leads to the set of linear equations represented by a tridiagonal matrix, which has nonzero elements only on the diagonal plus minus one column. Our way of obtaining the electric potential is by inverting this tridiagonal matrix.

The numerical solutions of the kinetic equations (Wigner or Vlasov) are much more elaborate and need more precautions. The solving procedure of these equations is based on the Eulerian approach [39] in which a uniform grid covers the entire phase space (x, v), and the distribution function is then defined on the mesh nodes. The main point of numerical solving of the Wigner and Vlasov equations is the use of the well-known splitting technique.

3.3.1 Splitting scheme for Vlasov model

Instead of solving equations (3.18) as a whole, the splitting procedure [40] separates the equation into two parts, which represent the free particle part and the interaction part. The solution from time t_n to time t_{n+1} can be obtained in four steps ($t^-_{n+1/2}$ and $t^+_{n+1/2}$ denote, respectively, the time before and after the electric potential is applied):

(a) $(t_n, t_{n+1/2})$. We have the free particle movement

$$\frac{\partial f}{\partial t} + v\frac{\partial f}{\partial x} = 0 \tag{3.21}$$

performing the shift in the x space, we obtain the solution

$$f(x,v)^\star = f\left(x - \frac{v\Delta t}{2}, v, t_n\right). \tag{3.22}$$

(b) $(t = t^-_{n+1/2})$. We compute the electric potential at time $t_{n+1/2}$ by substituting $f^\star$ in the Poisson equation (3.19).

(c) $(t = t^+_{n+1/2})$. While the potential is applied, the free–particle motion is neglected, and we deal with the interaction part. Thus we have

$$\frac{\partial f}{\partial t} + \frac{e}{m}\frac{\partial V}{\partial x}\frac{\partial f}{\partial v} = 0 \tag{3.23}$$

performing the shift in the v space

$$f(x,v)^{\star\star} = f^\star\left(x, v - \frac{e}{m}\frac{\partial V}{\partial x}\Delta t\right). \tag{3.24}$$

(d) $(t_{n+1/2}, t_{n+1})$. Starting from $f(x,v)^{\star\star}$ step (a) is repeated

$$f(x,v,t_{n+1}) = f^{\star\star}\left(x - \frac{v\Delta t}{2}, v,\right), \tag{3.25}$$

and once again we follow the free particle motion.

Thus repeating the successive shifts, we can follow the time evolution of f.

The numerical implementation of the shifts, either in position or velocity space, requires the interpolation of the distribution function in phase-space. It can be done according to different schemes like cubic splines [41], finite volumes or fast Fourier transforms [42]. Here we employed a numerical technique based on a finite–volume technique, in which the electron distribution is assimilated to a phase-space "fluid" [43].

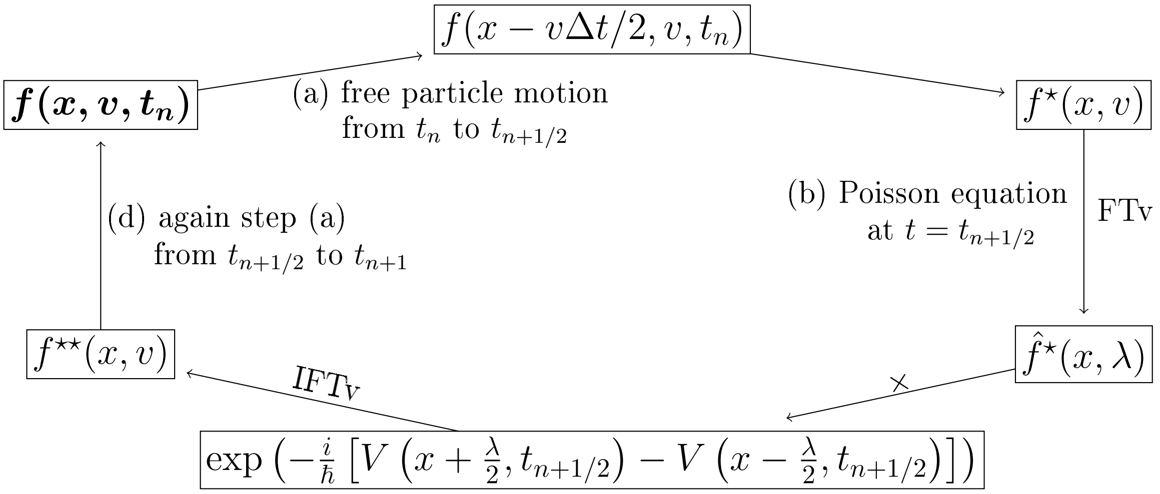

Figure 3.2: Schematic view of the splitting method. FTv stands for Fourier transform with respect to v. IFTv means inverse Fourier transform, and × denotes multiplication (i.e. shifting the phase).

3.3.2 Splitting scheme for Wigner model

The solution of the Wigner equation (3.17) is based on the same scheme as in the Vlasov case, with only a few modification of the interaction part. The first two steps in the procedure of solving are identical and the first difference appears when we come to the acceleration term, which in the quantum case is much more complicated.

While the potential is applied the free particle motion is neglected, and we deal with the interaction part. Thus we have

$$\frac{\partial f}{\partial t}+\frac{i}{2\pi\hbar^2}\iint f(v')\left[V\left(x+\frac{1}{2}\lambda,t\right)-V\left(x-\frac{1}{2}\lambda,t\right)\right]e^{-im(v-v')\lambda/\hbar}d\lambda dv'=0 \quad (3.26)$$

performing the Fourier transformation in v space (λ is the Fourier conjugate of v)

$$\hat{f}^{\star\star}(x,\lambda,t^{+}_{n+1/2})=\hat{f}^{\star}(x,\lambda,t^{-}_{n+1/2})\exp\left(-\frac{i}{\hbar}\left[V\left(x+\frac{1}{2}\lambda,t^{-}_{n+1/2}\right)-V\left(x-\frac{1}{2}\lambda,t^{-}_{n+1/2}\right)\right]\Delta t\right). \quad (3.27)$$

Taking the inverse Fourier transform we obtain $f(x,v)^{\star\star}$, and again the free particle motion is repeated. Schematic representation of this method is shown in figure 3.2.

3.3.3 Boundary conditions

The boundary conditions associated with our system are defined in following manner: for the electron distribution, we define a computational box: $-L_{max}/2 \leq x \leq L_{max}/2$ and $-v_{max} \leq v_x \leq v_{max}$, with $L_{max} > L$ (where L is the film thickness), and $v_{max} > v_F$. The ground-state of the Wigner function is computed on a smaller box, but during the evolution our computational box has to be extended in order to make sure that the electrons do not leave it. For the Poisson equation we chose the boundary conditions $V_H(\pm L_{max}/2) = 0$.

3.3.4 Numerical parameters

In this work we mainly consider films of thickness $L = 50L_F$ (which gives for sodium film $L \approx 6$nm). For diffuseness parameter $\sigma_i = 0.3L_F$, we obtain $N = 18$ occupied states for the ground-state at $T_e = 0$ K; more states are occupied at finite temperature. The computational box L_{max} is chosen to be $L_{max} = L + 210L_F$, which corresponds to an empty buffer zone of $105L_F$ on each side of the film. By using this condition we want to be sure that no electrons leave our system.

3.4 Non-interacting linear response

Before turning to the interesting regime of the nonlinear effects, it is useful to have some insight into the basic nature of the system. The detailed structure of the ground-state has been obtained from the density functional theory, and now we would like to compare these results with the results of the Wigner–Poisson equation within the linear regime. This also constitutes a good test of the correctness of our numerical scheme.

The way of attaining the linear regime in our nonlinear model is by excluding the Poisson equation form the calculation procedure. By this condition we remove all possible interaction between electrons. For the time evolution, we make use of the effective potential V_{eff} calculated for the ground-state using DFT (in this case it is a pure Hartree potential) and then we keep it fixed throughout the simulation. In this way we preclude self-consistent processes, thus focusing on the linear response.

Here we show the spectral properties and their relation to the underlying structure of the sodium film. One of the most important quantities used in monitoring the electron

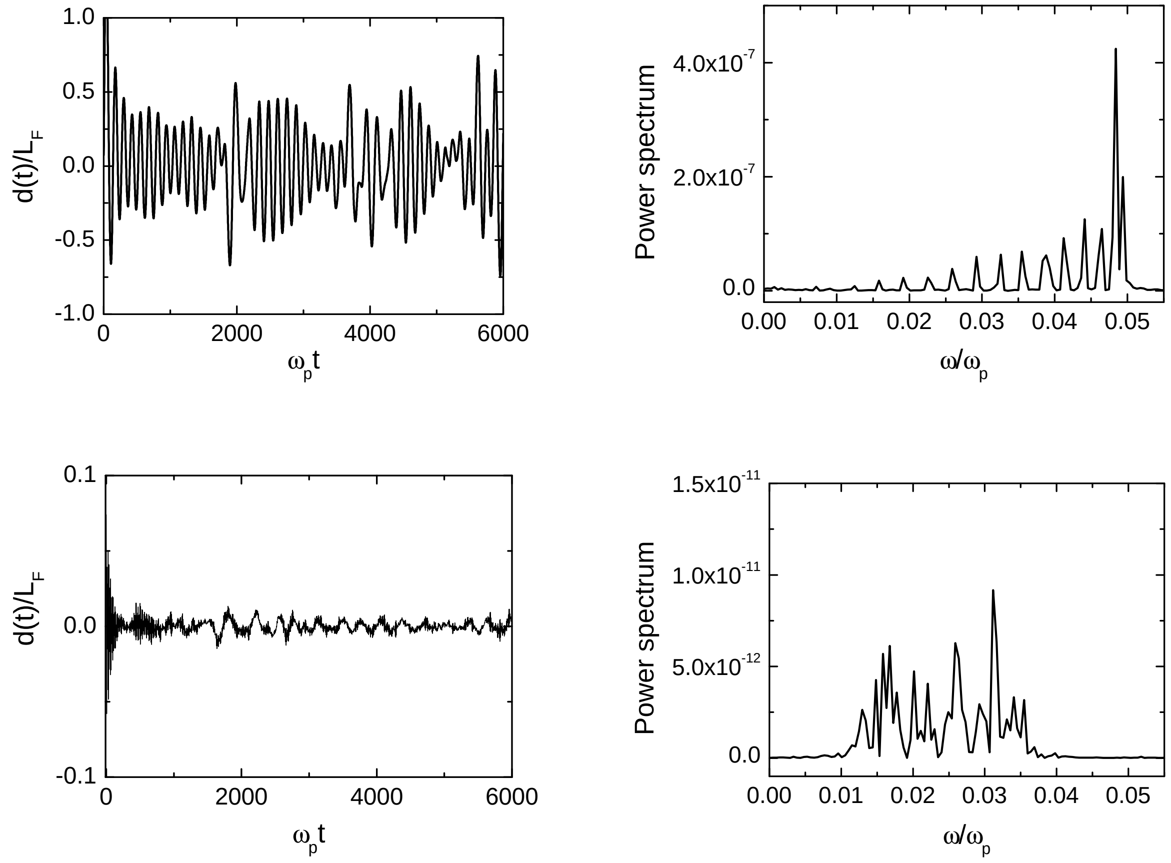

Figure 3.3: Time evolution of the electric dipole for the excitation $\delta v = 0.06 v_F$ in the cases without Poisson equation (top) and with Poisson equation (bottom), together with the power spectrum at $T_e = 300$ K.

gas relaxation is the evolution of the electric dipole, defined as [36]

$$d(t) = \frac{\iint f x dx dv}{\iint f dx dv}. \tag{3.28}$$

For metal nanoparticules, their size is usually smaller than the wavelength of the laser excitation as well as the optical penetration depth, therefore all conduction electron in the particle can be collectively excited. The collective oscillation can be interpreted as a displacement of the center of mass of all electrons in the nanoparticle against the positive background, and for that reason the electric dipole are so important in our investigation.

The dipole evolution is presented in figure 3.3 for the excitation $\delta v = 0.06 v_F$, together with its frequency spectrum (defined as the square of the absolute value of the Fourier transform of $d(t)$). For comparison we also show the typical behavior of this quantity

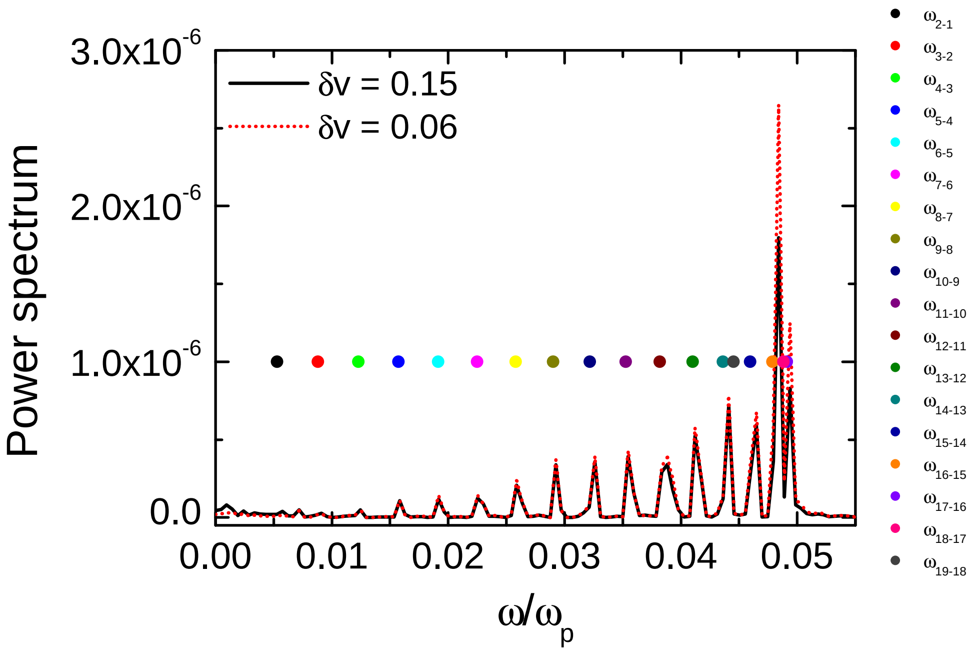

Figure 3.4: Power spectrum of the time history of the electric dipole, together with the transition frequencies obtained from the DFT (large dots). The red dotted line represents the power spectrum for $\delta v = 0.06 v_F$ rescaled by the factor $C = (0.15/0.06)^2$.

in the case of fully nonlinear run, which will be discussed in more details in the next chapter.

In order to understand better the maxima appearing in the power spectrum for the linear regime we have compared them with the transition frequency ω_{i-j} obtained for the ground-state (figure 3.4). The frequency ω_{i-j} corresponds to the frequency of transition from energy level E_i to E_j defined as $\omega_{i-j} = (E_i - E_j)/\hbar$. As we can see in the figure those frequencies almost exactly match the peak values obtained from the Fourier transform of the dipole $d(t)$. The higher intensity for the high energy levels is connected to the fact that these states are near the Fermi level and the transitions in that region occur more often. From the above picture it appears that the linear response is dominated by the transition between the ground-state energy levels. In the nonlinear regime, the observed spectrum cannot be easily explained in the similar way since the observed peaks are rather irregular.

In order to highlight the linear behavior of our model without the Poisson equation we plotted the power spectrum for two excitation values. The red dotted line in figure 3.4 represents the rescaled by an appropriate factor response of the system to the excitation $\delta v = 0.06 v_F$. As we are comparing the excitations $\delta v = 0.06 v_F$ and $\delta v = 0.15 v_F$ the scaling factor is equal $C = (0.15/0.06)^2$. This is a general rule and works equally well for other excitations, with the multiplication factor being the square of the ratio of the considered perturbations. Having in mind that the excitation energy E^* is linked to the perturbation in velocity δv by the relation $E^*/E_F = \bar{n}_i L(\delta v/v_F)^2$, it is clear that the response of the electron gas is linear with respect to the injected energy E^*.

Chapter 4

Electron dynamics in thin sodium films

After describing some of the most important properties of the ground-state and some aspects of the linear response, we can now proceed to the main topic of the present work that is the electronic dynamics in metallic nanoparticles. The most important experimental results in this domain have been achieved thanks to the developments of modern ultrafast pump–probe spectroscopy. In a typical pump–probe experiment, the system is excited two successive laser pulses. The pump pulse brings the electron gas out of equilibrium, while the second weaker pulse (the probe) acts as a diagnostic tool. By modulating the delay between the pump and the probe, it is possible to assess with the great precision the dynamical relaxation of the electron gas.

The description of the electron gas confined in a thin metal film will be preceded by a short representation of dynamical mechanisms involved in the ultrafast dynamics. We will present a typical schematic scenario and the associated time scales observed in experiments after laser excitation.

4.1 Time scales and associated regimes

In order to get better insight into the electron dynamics occurring in metal nanoparticles, let us summarize the typical processes and the associated time scales in sodium clusters [44]. The electron dynamics in metallic nanostructures reveals different behavior than that observed in the bulk material. Steady progress of experimental techniques has given

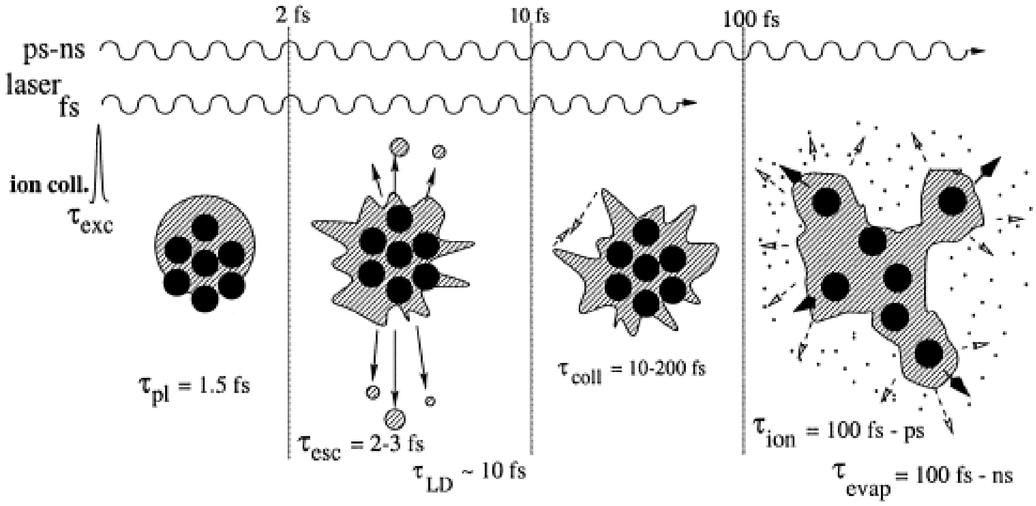

Figure 4.1: Schematic view of relaxation processes in metallic nanoparticles. (reprinted from Ref. [44])

access to the nonlinear domain. As the examples of nonlinear excitation we can mention, for instance:

- beams of highly charged ions – which are designed to ionize nanoparticle into high energy state
- femtosecond lasers – currently used in pump–probe experiments.

These approaches differ in their duration, from ns to sub-fs, but both have in common that they couple to the nanoparticle via the Coulomb interaction.

Initially, the electrons absorb quasi-instantaneously the laser energy via interband and/or intraband transitions. This early stage leads to the creation of a collective oscillation, the so-called surface plasmon (leftmost panel in figure 4.1). Shortly after, the plasmon oscillations are damped through coupling to self-consistent quasiparticle excitations (Landau damping, showed in the second panel of figure 4.1) [45, 46]. This damping, which occurs on a very fast time scale ($\sim 10 - 50$ fs), was observed experimentally in gold nanoparticles [47] and was studied theoretically in several works [46, 48, 49]. During these fast processes the density of excited states depends on the spectral shape of laser pulse and the corresponding electron distribution is non-thermal.

The subsequent step in describing the energy relaxation represents a thermalisation of the electrons ("internal" electron thermalization). The arrangement of occupied electronic states tend to a Fermi–Dirac distribution with a well defined temperature. The electrons undergo electron–electron collisions that eventually lead the electron cloud towards thermal equilibrium, sketched in the third snapshot of figure 4.1. This increase of the temperature due to the laser excitation can easily reach several thousands of degrees, depending on the excitation intensity.

Electron–lattice thermalisation generally occurs on even longer time scales (rightmost panel in figure 4.1), and this process can be described by two coupled thermal baths (the electrons and the lattice). The subject of electron–phonon interaction will be addressed in the next chapter.

In this chapter the main attention is paid to the ultrafast electron processes in which the ionic background remains frozen. Several experiments have shown [6, 7] that heat transport through the film involves ballistic electrons travelling at the Fermi velocity of the metal. These findings were recently corroborated by accurate numerical simulations [36, 50, 51] obtained with a classical phase-space model (Vlasov-Poisson equations). These simulations also highlighted a regime of slow oscillations – corresponding to ballistic electrons bouncing back and forth on the film surfaces – whose period scales linearly with the thickness of the film. Such oscillations were recently measured in transient reflection experiments on thin gold films [23], and their period was shown to obey the predicted scaling.

The above results relied on a completely classical description of the electron dynamics, based on the evolution of a phase-space probability density according to the Vlasov equation [44]. Electron–electron interactions were taken into account within the mean-field approximation, via the electrostatic Poisson's equation (some attempts to include dynamical correlations beyond the mean field were also made).

The purpose of the present chapter is to extend the classical results by including quantum-mechanical effects. For that purpose we make use of the models described in the previous chapter. We perform quantum and semiclasscial simulations of the electron dynamics in order to study the relaxation processes described in the above paragraphs. In quantum model, except where stated otherwise, we will neglect the exchange and correlation potential, so that our description reduces to the mean-field approximation. This will facilitate the comparison with the classical results, for which only the Hartree potential was present.

4.2 Observables

The electron dynamics in thin metal films can be analyzed in terms of different forms of the energy that is deposited, stored or lost during the processes described in Sec. 4.1. A lot of information can be gained by monitoring how the different energy components evolve in time.

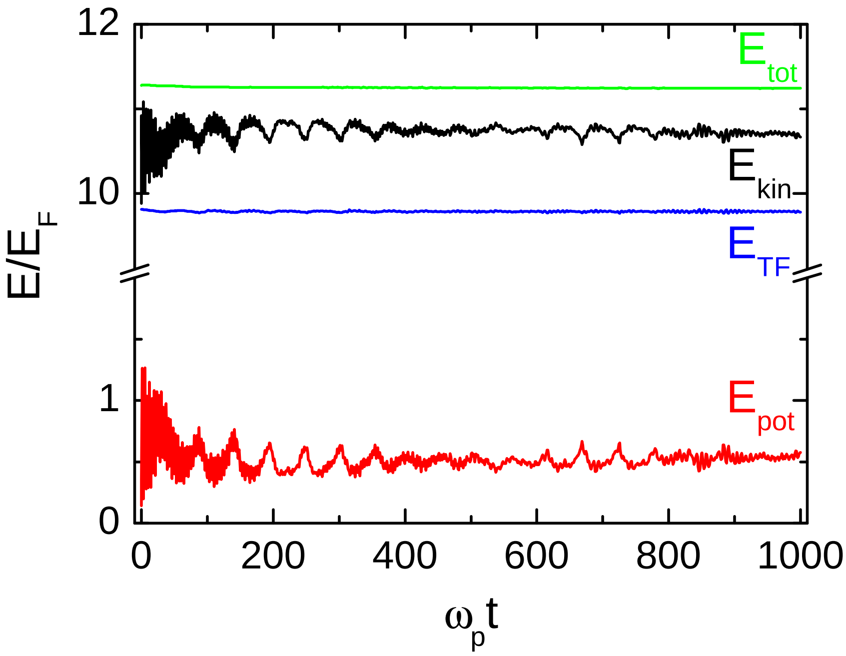

Figure 4.2: Typical behavior of the total, kinetic, Thomas–Fermi and potential energy in Wigner simulations for the excitation $\delta v = 0.15 v_F$ at $T_e = 300$ K.

During the time evolution, several energy quantities will be considered (all normalized to the Fermi energy). The total energy of the electron gas is given by the sum of kinetic plus potential energy $E_{tot} = E_{kin} + E_{pot}$. The kinetic energy $E_{kin} = \iint v^2 f dx dv$ can be spit into three parts:

- The Thomas–Fermi energy $E_{TF} = \frac{1}{5}\int n(x)^{5/3} dx$ – energy of the equivalent zero temperature ground state with the same density,
- The center–of–mass energy $E_{c.m.} = \frac{1}{2}\int \frac{j^2(x,t)}{n(x,t)} dx$ (where $j = \int v f dv$ is the electron current) – the kinetic energy of the center of mass of the electron distribution,

- The thermal energy $E_{th} = E_{kin} - E_{TF} - E_{c.m.}$ – which corresponds to the kinetic energy of the electrons located in a shell of thickness $k_B T$ around the Fermi surface.

The potential energy involving the electric potential is define in the following manner: $E_{pot} = \frac{1}{2} \int E^2 dx$.

In order to study the electron dynamics, a small perturbation was added to the electronic ground state. The perturbation is in the form of a uniform shift δv of the entire electron population in velocity space. In this way, some energy is injected into the system in the form of kinetic energy of the center of the mass of electron population. After applying such perturbation, the electron gas evolves under the action of the self-consistent electric potential.

We consider situations where no linear momentum is transferred parallel to the plane of the surfaces (i.e., only excitation with $k_{\shortparallel} = 0$ are taken into account). This situation corresponds to the excitation of the slab with optical pulses and also to the response to a uniform electric field oriented normal to the surface. The dispersion relation of the slab collective modes is given by expression $\omega_{\pm}(k_{\shortparallel}) = \omega_p \sqrt{(1 \mp e^{-k_{\shortparallel} L})/2}$. For $k_{\shortparallel} = 0$, only longitudinal modes (volume plasmon) can be excited.

The typical behavior of some energy quantities is shown in figure 4.2. Good test of the stability of our numerical result can be provided by the conservation of the total energy. As we do not include any dissipation terms the total energy shouldn't change during the run. This condition is fulfilled with a good accuracy as we can see in the figure.

The Thomas–Fermi energy is also more or less constant with only small fluctuation. As E_{TF} is quite significant, but not contributing a lot to the electron dynamics, in the rest of this chapter we will investigate the behavior of the thermal and the center–of–mass energies as they exhibit more interesting effects.

4.3 Dynamics

4.3.1 Electron dipole

The relaxation of the electron gas is frequently studied by monitoring the electric dipole, given by $d(t) = \frac{\iint fx dx dv}{\iint f dx dv}$. The evolution of the dipole for both the Vlasov and Wigner

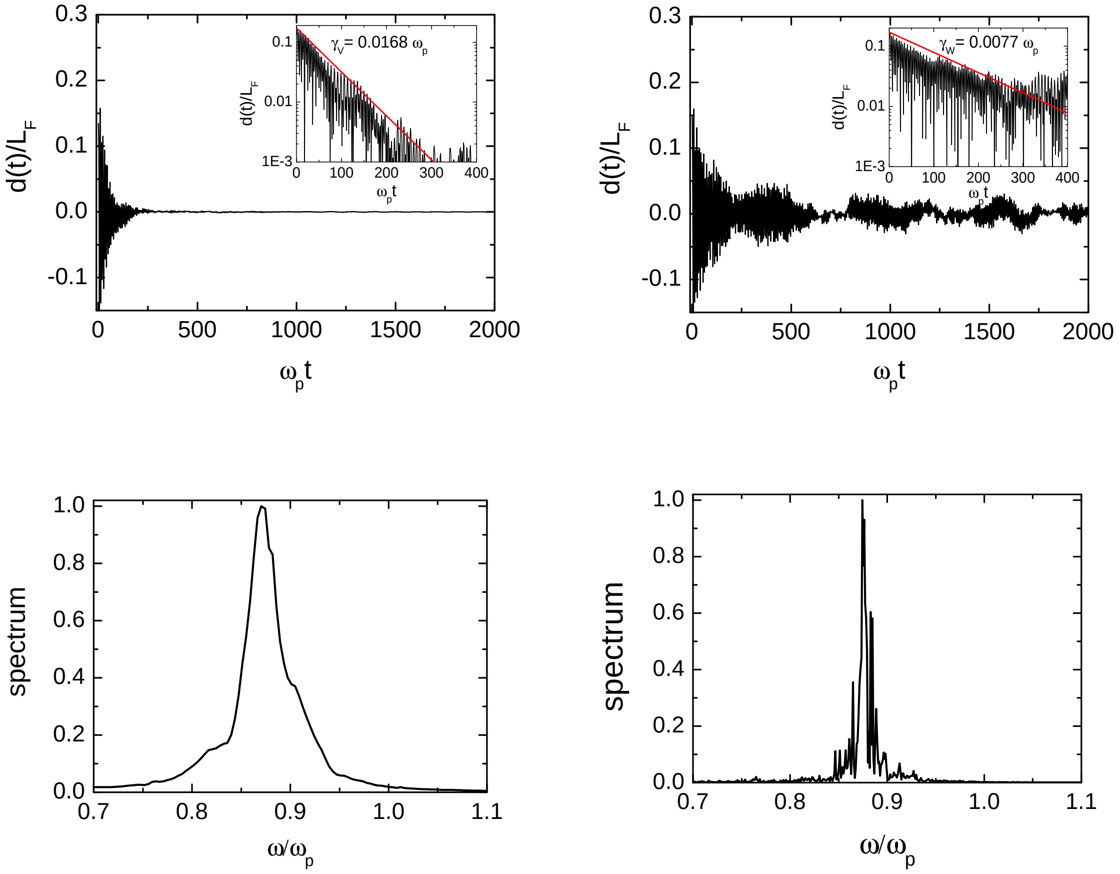

Figure 4.3: Top panels: time evolution of the electric dipole (left Vlasov, right Wigner) for the excitation $\delta v = 0.15$, the inset shows in semilog scale zoom for the initial exponential damping of the dipole oscillations. The solid red line is a fit to the numerical data. Bottom panels: frequency spectra of the time history of the electric dipole, normalized to its maximum value.

cases, are shown in figure 4.3, together with their frequency spectrum. The dipole oscillates at a frequency slightly smaller than the electron plasma frequency. The observed frequencies are not exactly equal to ω_p, because the computational box is necessarily finite. Indeed, the boundary conditions $V_H(\pm L_{max}) = 0$ allow normal modes with a frequency less than ω_p. In a truly infinite medium ($L_{max} \to \infty$), the fundamental frequency should approach ω_p. This point has been verified by taking larger computational boxes.

The dipole oscillation is initially damped exponentially with a rate approximately equal to: $\gamma_V = -0.0168\omega_p$ for the Vlasov model, and $\gamma_W = -0.0077\omega_p$ for the Wigner one. In the classical regime, the electron dipole is more damped than for the quantum, but in both cases the frequency is almost identical. The different values of the damping rates are also reflected in the corresponding frequency spectra. For the Wigner model, the main peak in the spectrum is narrower than in the Vlasov case.

Another difference between the quantum and classical runs appears in the behavior of the dipole for longer times. In the Vlasov case, after some initial fast oscillations, the dipole amplitude decays to zero, whereas in the Wigner simulations we can still observe some revivals where the amplitude of the dipole is significant.

4.3.2 Energy relaxation

The long time electron relaxation can be studied by tracking the time history of the energy quantities defined in 4.2. Looking at the classical results, several phases can be identified in the time evolution (left panel of figure 4.4). An initial phase features damped collective oscillation of the electron gas occurring at a frequency close to ω_p, which corresponds to the damping of the electric dipole discussed above. The fast oscillation are observed in the behavior of $E_{c.m.}$ up to $\omega_p t \approx 200$. At this time, the center-of-mass energy is almost entirely converted into thermal energy. After saturation of the thermal energy a slowly oscillating regime appears. These slow oscillations are slightly damped, but still persist until the end of the run. Classically, the period T of these oscillations approximately equals to the time of flight of electrons traveling through the film at a velocity close to the Fermi velocity of the metal, i.e. $T = L/v_F$. Therefore, this effect can be attributed to nonequilibrium electron bouncing back and forth against the surface of the film [36].

The general behavior of the same energy quantities in the quantum case is roughly similar, although the details of the evolution are obviously different (figure 4.4). A first difference between the classical and quantum evolutions is that the centre-of-mass energy does not completely decay to zero in the quantum regime. This effect was already observed in quantum hydrodynamic simulations [52] and implies that Landau damping (i.e., the coupling of the centre-of-mass coordinates to the internal degrees of freedom of the electron gas) is acting less efficiently in the quantum regime. Indeed, Landau damping is a phase-mixing effect that arises from many different states oscillating at slightly different frequencies and is thus amplified in the classical regime, where the number of states is effectively infinite. When the spectrum is discrete and the number of states is finite, beatings and revivals can occur, thus reducing the efficiency of Landau

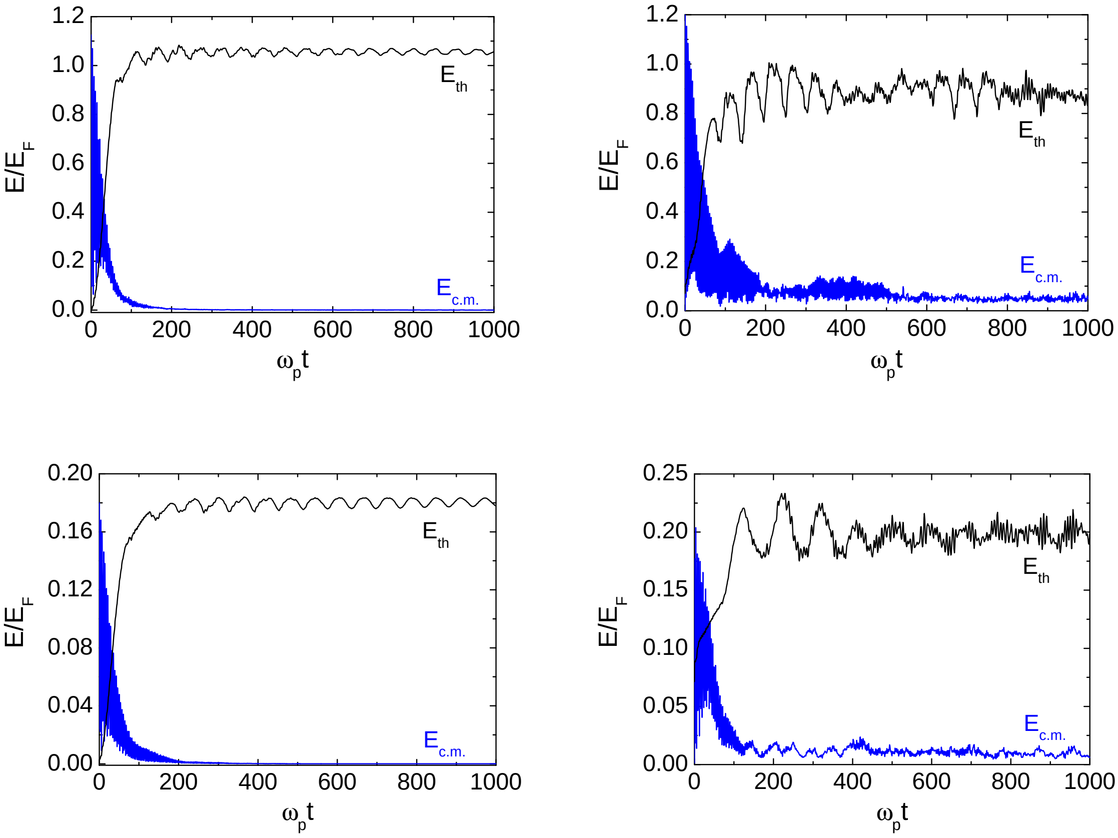

Figure 4.4: Time evolution of the thermal energy and centre-of-mass energies in the classical case (left panel) and quantum case (right panel). Top line corresponds to the excitation $\delta v = 0.15 v_F$, beneath the excitation $\delta v = 0.06 v_F$

damping. Indeed, a revival is visible in figure 4.4 (right panel) around $\omega_p t \simeq 400$, with an increase of the of the centre-of-mass energy and the corresponding decrease of the thermal energy.

Another difference between quantum and classical results can be found by reducing the magnitude of the perturbation. In the case of high energy excitation the period of the slow nonlinear oscillations is more or less the same in both instances. Now, when the disturbance is reduced to $\delta v = 0.06 v_F$, we still observe some low–frequency oscillations in the quantum dynamics, however, their period is significantly longer than that of the corresponding Vlasov results (bottom line of figure 4.4). Clearly, at low excitation, the simple picture of electron bunches traveling through the film at Fermi velocity is changed and new effects emerge.

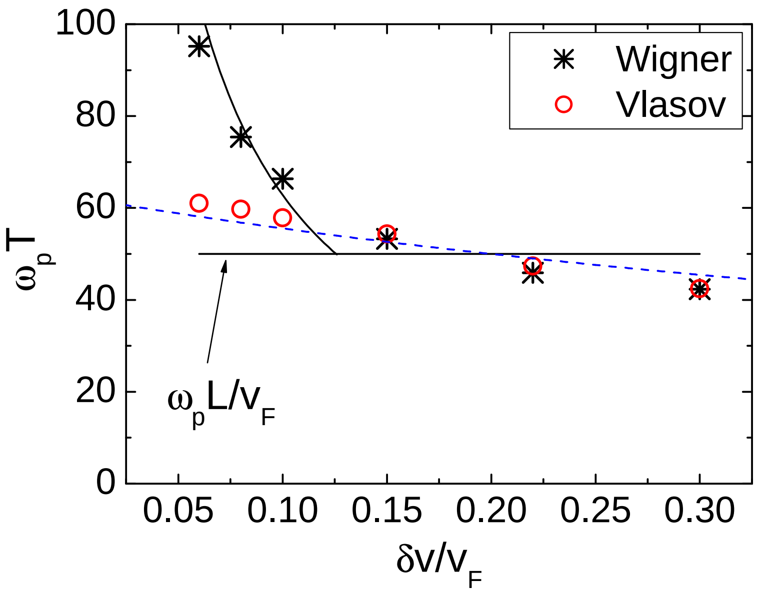

Figure 4.5: Period of the low–frequency oscillations as a function of the perturbation, for a slab of thickness $L = 50L_F$ and temperature $T_e = 300$ K, in the Vlasov and Wigner regimes. The quantum results neglect exchange and correlations (pure Hartree model). The horizontal solid line corresponds to the ballistic period L/v_F; the solid curve at small excitations refers to equation (4.2) and dashed line corresponds to the corrected classical period $T = L/(0.8v_F + |\delta v|)$

By plotting the observed period T of the low–frequency oscillations against the value of the perturbation we can find interesting feature. As expected, the classical and quantum results coincide for large excitation (i.e. the period is close to the ballistic value $T = L/v_F$), but they start to diverge near a certain threshold δv_{th}. Below the threshold, the period stays close to the ballistic value for Vlasov simulations, whereas it becomes considerably larger for the Wigner results.

In this way a clear transition between a classical and a quantum regime can be observed. The estimation of the threshold value of the excitation requires investigation of the microscopic electron dynamics in the phase space. The phase space portraits of the electron distribution function $f(x, v, t)$ in figure 4.8 show the bunches of nonequlibrium electrons traveling with a velocity close to the Fermi velocity between the surfaces of the film. These bunches (i.e. vortices in the phase space) have a spatial extension roughly equal to $2\pi L_F$ and a width of the order of δv in velocity space. The surface

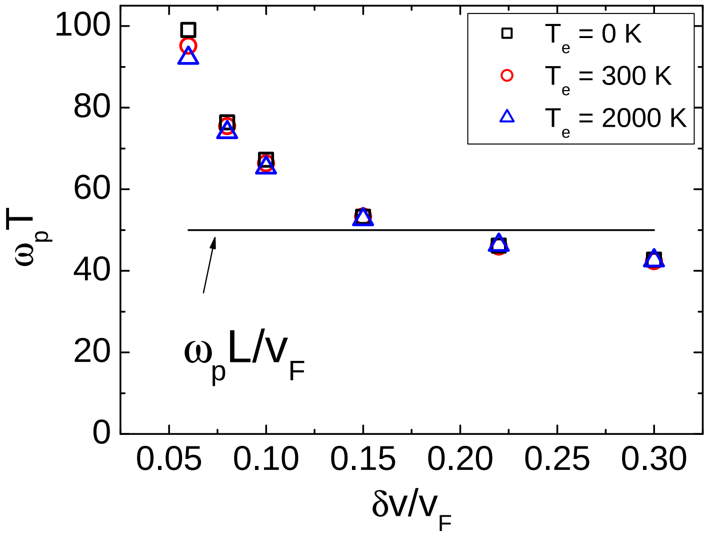

Figure 4.6: Period of the low–frequency oscillations as a function of the perturbation, for a slab of thickness $L = 50L_F$ and temperatures in the range $T_e = 0 - 2000$ K.

of the these vortices in the phase-space (which has the dimension of an action) is thus approximately $S \approx 2\pi L_F m\delta v$. The quantum effects are expected to become significant when this action is of the same order as Planck's constant, i.e. $S \approx \hbar$. This leads to the following expression for the threshold, in dimensionless units:

$$\frac{\delta v_{th}}{v_F} = \frac{\hbar\omega}{4\pi E_F}. \tag{4.1}$$

For sodium it gives $v_{th} = 0.15 v_F$, which is fairly close to the observed value.

This result can be interpreted from a different angle. By applying the perturbation δv, we change slightly the velocity of the electrons near the Fermi surface. The change in kinetic energy, for these electrons, can be written as $\delta E = m v_F \delta v$. Taking equation (4.1), we obtain that the threshold can be expressed as $\delta E = \hbar\omega_p/2\pi$. Thus, quantum effects become significant when the excitation induces a change in the kinetic energy on the Fermi surface that is considerably smaller than the plasmon energy $\hbar\omega_p$.

Below the threshold, the quantum results still display some persistent low–frequency oscillations, but these are no longer related to the ballistic motion of the electrons and subsequent bouncing on the surfaces. Instead, the quantum oscillations can be linked to the excitation energy around the Fermi surface in such a way that $\hbar\omega = \delta E$, where

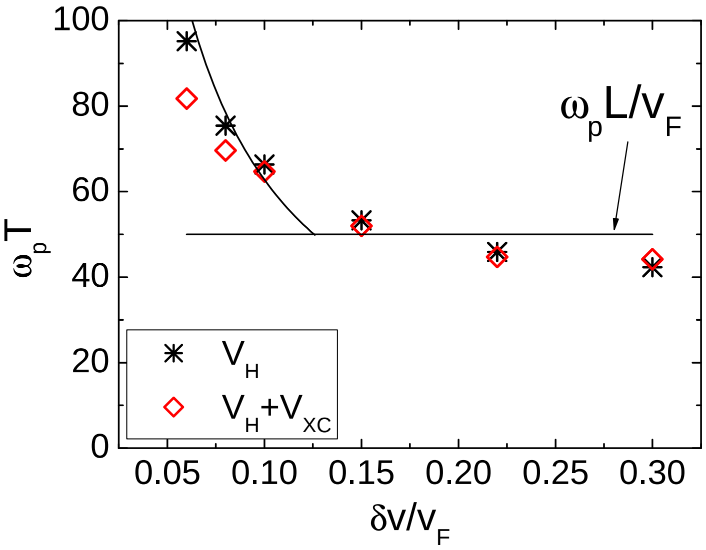

Figure 4.7: Period of the low–frequency oscillations as a function of the perturbation, for a slab of thickness $L = 50L_F$ and temperature $T_e = 300$ K, in quantum regime. Black stars: pure Hartree model; red diamonds: Hartree plus exchange and correlations.

$\omega = 2\pi/T$ is the oscillation frequency. Then, we obtain for the period:

$$T = \frac{2\pi\hbar}{mv_F\delta v}, \tag{4.2}$$

which reproduces rather well the observed data (black line in figure 4.5). The oscillations observed for the low-perturbation regime appear to be linked to the excitation of quantum eigenmodes close to the Fermi level. In contrast, for large perturbation, many states are excited simultaneously, thus activating the classical ballistic regime at the Fermi speed.

The Vlasov results also display a weak dependence on the perturbation amplitude, and the period is not exactly equal to the ballistic value $T = L/v_F$. This effect can be explained as follows. Some previous studies of the classical behavior [51] showed that the transit velocity of the electrons is somewhat smaller than the Fermi speed, namely $\approx 0.8v_F$. In addition, the actual transit velocity should also include the perturbation δv. Those two effects lead to an expression for the oscillation period given by $T \approx L/(0.8v_F + |\delta v|)$, which corresponds to the dashed line in figure 4.5 and appears to agree rather well with the Vlasov results all over the perturbation range.

The effect of the electron temperature is portrayed in figure 4.6 for the Wigner model. For all the cases showed here, the quantum–classical transition is still clearly observed. In the low excitation regime we are able to discern the weak dependence of the oscillation period on the electron temperature.

Finally, we investigate the effect of exchange and correlations potential

$$V_{xc}(x) = -\frac{0.611}{r_s(x)} - \frac{0.587e^2}{(r_s(x)+7.8)^2}(r_s(x)+5.85). \tag{4.3}$$

The observed period (figure 4.7) is slightly smaller (compared with the Hartree result) in the low-excitation regime, whereas it converges again to the Vlasov results for high excitations. As the combined effect of exchange and correlations has a considerable impact on the ground-state potential, it is not too surprising that the oscillation period is also affected. Nevertheless, a clear departure from the ballistic value of the period is still observed for low excitations.

4.3.3 Phase-space dynamics

In the classical studies[36, 50, 51], it was clearly shown that the oscillations studied in the above paragraphs are due to electrons travelling through the film at a velocity close to the Fermi speed of the metal. Indeed, the phase-space portraits of the electron distribution function revealed the presence of travelling vortices around $v = v_F$. We have already discussed the fact that the transition between the classical and quantum behavior occurs when the size of these vortices becomes of the order of Planck's constant.

Direct comparison between the quantum and classical electron distribution portraits in phase-space are presented in figure 4.8 for high and low excitation, respectively. For the larger excitation ($\delta v = 0.15 v_F$), both the Vlasov and the Wigner simulations feature several coherent structures (vortices) propagating ballistically at the Fermi velocity. For the smaller excitation value ($\delta v = 0.06 v_F$), the vortices are still visible in the Vlasov regime, but they have completely disappeared from the Wigner simulations. In this case, the Vlasov and Wigner regimes exhibit clearly different properties in their respective phase-space portraits.

A zoom on the phase-space portraits (figure 4.9) confirms the presence of electron vortices near Fermi speed. Quantum effects can destroy these structures, thus preventing the ballistic oscillations from arising. In the specific case $\delta v = 0.06 v_F$, the area (action) of a phase-space vortex is, in normalized units, $S/(m v_F L_F) \approx 2\pi \delta v / v_F = 0.38$. Which

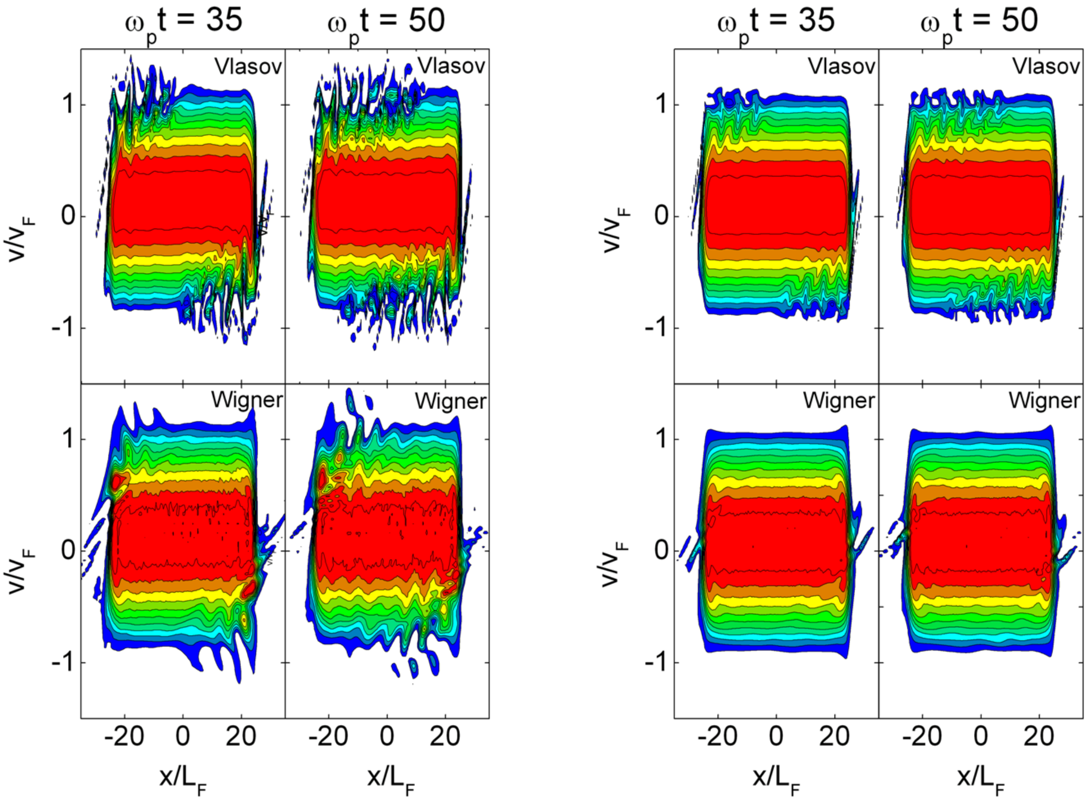

Figure 4.8: Contour plot of the electron distribution function in the phase space at different times, $\omega_p t = 35$ and $\omega_p t = 50$, for large excitation $\delta v = 0.15 v_F$ (left panel) and for small excitation $\delta v = 0.06 v_F$ (right panel). Top panels: classical results and bottom panels: quantum results.

is smaller than the normalized Planck's constant $\hbar/(m v_F L_F) \approx 0.94$ for sodium, and quantum effects are strong enough to impede the formation of the vortices.

4.4 Discussion

In this chapter, we extended classical studies on the electron dynamics in thin metal films, by including quantum-mechanical effects through the Wigner phase-space representation.

Previous (purely classical) simulations had highlighted a regime of low-frequency "ballistic" oscillations due to the bouncing of nonequilibrium electrons on the film surfaces [36, 50]. These oscillations were subsequently observed in experiments on thin gold

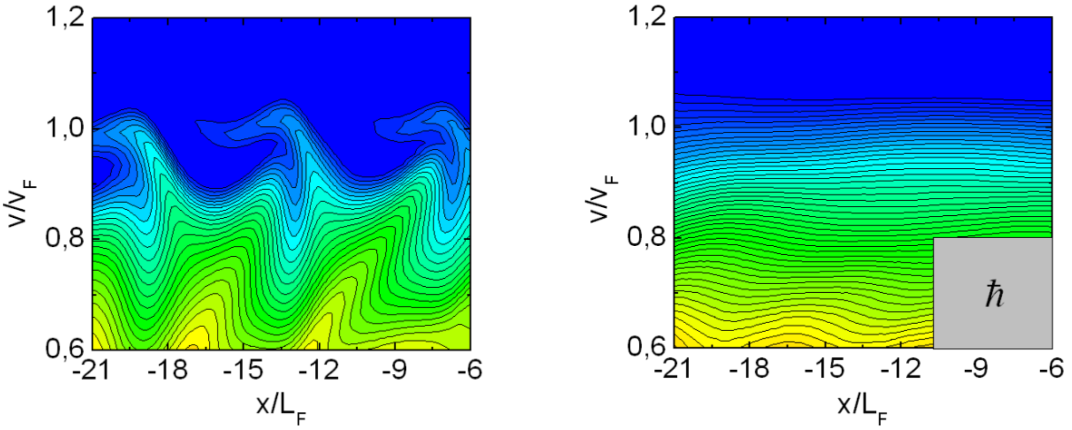

Figure 4.9: Zoom of the electron distribution function in the phase-space region near the Fermi surface, at time $\omega_p t = 35$, for a film of thickness $L = 50L_F$, temperature $T_e = 300$, and excitation $\delta v = 0.06v_F$. Vortices are present in the Vlasov case (left panel), but disappeared in the Wigner case (right panel). The shaded are in the right panel represents Planck's constant in normalized units, i.e. $\hbar/(mv_F L_F)$.

films [23].

Our key result was that, by reducing the strength of the initial excitation, a neat transition from a classical to a quantum regime could be observed. Indeed, at weak excitation energies (smaller than one quantum of plasmon energy, $\hbar\omega_p$) the period of the low-frequency oscillations departs significantly from the ballistic value observed in the classical simulations. The estimated threshold of this quantum-classical transition agrees well with the simulations. We also proved that this result is robust, in the sense that it depends only weakly on physical parameters such as the electron temperature, or the choice of a specific exchange-correlation functional.

The above findings constitute an example of a quantum-classical transition in the electron dynamics that could, in principle, be observed experimentally. For instance, in [51] it was shown that the ballistic oscillations could be used to enhance the energy absorption by the electron gas, when the film is irradiated with an electromagnetic wave (laser pulse) that matches the frequency of the ballistic oscillations (for sodium films, the frequency lies in the infrared range). This is a case of nonlinear resonant absorption. In the quantum regime, the resonant frequency should be further redshifted (because the period increases), and the overall effect could be observable experimentally.

Further, recent pump-probe experiments [53] carried out on metal nanoparticles revealed an increase of the expected electron-phonon relaxation time when the particle's diameter is less than 2 nm. This anomalous behaviour was attributed to quantum effects arising from the discrete nature of the electronic states inside such small nanoparticles.

In our simulations, the quantum-classical transition occurs not by reducing the size, but by weakening the external excitation. This might make it even easier to observe in practice, as a precise knowledge of the film thickness is not *a priori* required. In addition, although our approach pertains primarily to alkali metals (particularly sodium), the observed effects should be generic and have a wider application to noble-metal films (Au, Ag), which are generally used in the experiments.

Chapter 5

Electron–lattice interaction

In the preceding chapter we focused our attention on the ultrafast electronic processes during which the ionic lattice remains frozen. Now, in order to complete the description of the electron dynamics in metallic nano-objects we need to incorporate the electron–ion coupling.

As it was described in more details in the previous chapter, after the electrons absorb the laser energy via interband and/or intraband transitions (the ionic background stays motionless), the injected energy is redistributed through electron–electron collision (time scale of the order of 100 fs). On a picosecond time scale, the electron gas starts to interact incoherently with phonons, and eventually relaxes to thermal equilibrium at the same temperature as the lattice. The lattice motion occurs on even longer times scales, and won't be addressed in the following description.

As the evolution spans overs an extremely wide time range, its comprehensive modeling is a difficult task. Several past studies were devoted to the early stages of the electron dynamics, relied on sophisticated microscopic models including Hartree–Fock calculation [54], time–dependent density–functional theory (TDDFT) [44], and phase-space approach [36]. For longer time scales, however, the situation is more problematic. On the one hand, the above models are computationally very expensive, particularly for large systems. On the other hand, the long-time electron dynamics becomes dissipative, as the electrons exchange energy incoherently with the ion lattice via electron–phonon (e–ph) scattering. Although some authors have recently attempted to include dissipative effects in TDDFT calculations [55], there is as yet no broad consensus on how to construct a many-body quantum model that incorporates dissipation.

Here we would like to present an extended version of the Wigner model to describe the microscopic electron dynamics over all time scales up to the coupling with the ion lattice.

5.1 Model

Our model describing the coupling between electrons and lattice is based on the same phase-space approach described in Chapter 4, in which the quantum evolution of the electron population is represented by the Wigner peudoprobability distribution $f(x, v, t)$. The advantage of this approach is that dissipative terms can be introduced by analogy with the classical transport models, such as the Fokker–Planck (FP) equation.

The evolution of the system is governed by the modified Wigner equation:

$$\frac{\partial f}{\partial t} + v\frac{\partial f}{\partial x} + \frac{im}{2\pi\hbar^2}\int\limits_{-\infty}^{\infty}\int\limits_{-\infty}^{\infty} d\lambda dv' e^{im(v-v')\lambda/\hbar} f(x, v', t) \tag{5.1}$$
$$\times \left[V_{eff}\left(x + \frac{1}{2}\lambda, t\right) - V_{eff}\left(x - \frac{1}{2}\lambda, t\right)\right] = \left(\frac{\partial f}{\partial t}\right)_{e-ph},$$

which now includes an electron–phonon coupling. As usually this equation is coupled self-consistently to the Poisson's equation.

5.1.1 1D geometry for thin metal film

The right–hand side of (5.2) represents electron–phonon scattering and has the form of a classical FP term:

$$\left(\frac{\partial f}{\partial t}\right)_{e-ph} = D\nabla_v^2 f + \gamma\nabla_v \cdot (vG[f]), \tag{5.2}$$

where γ is the nominal relaxation rate, D is a diffusion coefficient in velocity space, and $G[\cdot]$ is a functional that depends on the statistics and on the dimensionality of the system. For different distributions, G assumes the following forms:

- $G[f] = f$ – for particles obeying Maxwell–Boltzmann statistics
- $G[f] = f(1 - kf)$ – for fermions in 3D
- $G[f] = f_0[1 - \exp(-f/f_0)]$ – for fermions in 1D.

In the last expression f_0 stands for $f_0 = \frac{3}{4}\frac{\overline{n}_i}{v_F}\frac{T_i}{T_F}$, where T_i is the lattice temperature (for more details see Appendix A). Here we have one more complication resulting from the fact that the Wigner distribution can takes negative values. Thus, to ensure that G behaves identically for positive and negative values of f, the actual form of the functional is: $G[f] = f_0[1 - \exp(-|f|/f_0)]\mathrm{sgn}(f)$.

The FP equation can be seen as the continuum limit of the master equation of a Markovian process (random walk in velocity space). It can be proven that $(\partial f/\partial t)_{e-ph} = 0$ when the electron distribution is given by a 1D Fermi-Dirac function (μ is the chemical potential),

$$f_{eq}(v) = \frac{3}{4}\frac{n_0}{v_F}\frac{T_i}{T_F} \ln\left[1 + \exp\left(-\frac{mv^2/2 - \mu}{k_B T_i}\right)\right], \tag{5.3}$$

provided D and γ satisfy the relation

$$\frac{D}{\gamma} = \frac{k_B T_i}{m}. \tag{5.4}$$

Thus, the FP term guarantees that the electron distribution relaxes to a classical Fermi–Dirac distribution with a temperature equal to that of the lattice.

The electron relaxation rate can be written as $\gamma = g/2c_e$, where g is the electron–phonon coupling constant appearing in the two-temperature model (which will be described in more details later) and c_e is the electron heat capacity. For an ideal Fermi gas (which is a good approximation for a metal film with thickness on the order of a few nanometers), the heat capacity depends on the temperature as

$$c_e(T_e) = \pi^2 n_0 k_B \frac{T_e}{2T_F}. \tag{5.5}$$

In our case, the electron temperature is a time-dependent quantity that can be computed self-consistently from the Wigner distribution f.

The only physical parameter that remains to be fixed is the electron-phonon coupling constant g. Recent experiments on nanometer-sized sodium clusters [12] showed that g is largely insensitive to the temperature and the size of the system. The measured value of the coupling constant was roughly $g = 2 \times 10^{16}$ W/m^3 K, which is about twice as the experimental bulk value. All in all, we stress that our model does not contain any free fitting parameters and is entirely based on first-principles considerations and experimentally measured quantities.

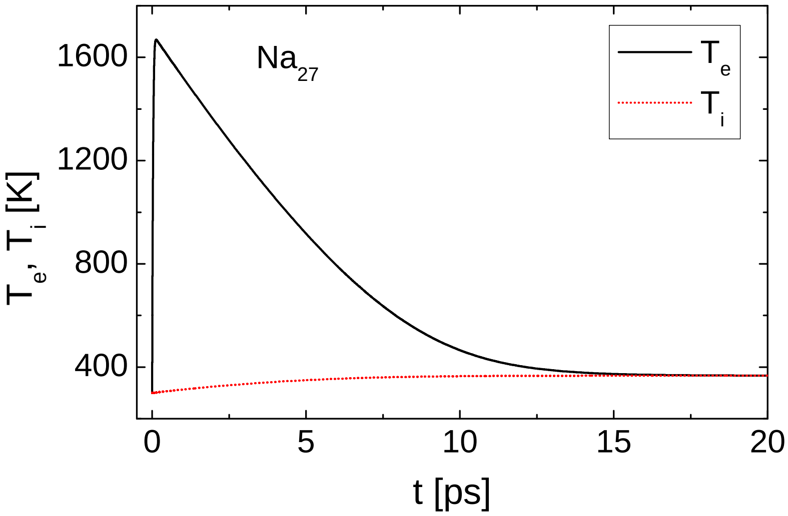

Figure 5.1: Time evolution of the electron temperature and lattice temperature for Na$_{27}$. In the two-temperature model, the pulse duration is $\tau = 100$ fs and the pulse intensity is $I = 10^9$ Wm^{-2}.

5.2 Two-temperature model

The absorption of the laser pulse cause the increase of the electron temperature of several thousands of degrees. If the pump–probe delay is comparable to or shorter then the electron–phonon energy–transfer time, then the electrons and lattice will not be in thermal equilibrium. The thermal relaxation to the lattice is achieved by the electron–phonon scattering. The characteristic time for the free electrons and the lattice to reach thermal equilibrium is called the thermalisation time and is typically on the order of a few picoseconds. The time evolution of the electron and lattice temperature can be described by a set of coupled nonlinear differential equations called the two-temperature model (TTM):

$$\begin{aligned} c_e \frac{\partial T_e}{\partial t} &= -g(T_e - T_i) + P(t) \\ c_i \frac{\partial T_i}{\partial t} &= g(T_e - T_i) \end{aligned} \tag{5.6}$$

where $P(t)$ represents the power density of the laser which acts as a source for the initial increase of temperature of the electrons, c_i is the lattice heat capacity, c_e is the electron heat capacity given by (5.5), and g is the electron–lattice coupling constant.

In figure 5.1 we show the typical time evolutions of the electron and ion temperature for a sodium nanoparticle composing of 27 atoms. The pulse duration is $\tau = 100$ fs and the pulse intensity is $I = 10^9$ Wm^{-2}. As can be seen from the picture, ions and electrons are in thermal equilibrium after 15 ps.

5.2.1 Connection between the two-temperature model and the Fokker–Planck equation

The two-temperature concept described above has been used in many experiments [12, 56, 57], and despite its simplicity, is capable of reproducing with good accuracy a large number of experimental results. Thus in our simulations we would like to compare our results with those from the TTM. First, however, let us show that there is a connection between the two-temperature model and the Fokker–Planck equation. This connection can be easily shown for the Maxwell–Boltzmann distribution, that is when $G[f] = f$.

Developing the integral on the left-hand side of (5.2) up to order $O(\hbar^2)$ we obtain

$$\frac{\partial f}{\partial t} + v\frac{\partial f}{\partial x} - \frac{eE}{m}\frac{\partial f}{\partial v} - \frac{e\hbar^2}{24m^3}\frac{\partial^2 E}{\partial x^2}\frac{\partial^3 f}{\partial v^3} = D\frac{\partial^2 f}{\partial v^2} + \gamma\frac{\partial}{\partial v}(vf). \tag{5.7}$$

where $E = -\partial V_{eff}/\partial x$. Multiplying equation (5.7) by v^2 and integrating over $dxdv$ we obtain

$$\frac{\partial}{\partial t}\iint fv^2 dxdv + 2\frac{eE}{m}\iint fvdxdv = 2DN_e - 2\gamma\iint fv^2 dxdv \tag{5.8}$$

with $N_e = \iint fdxdv$. Now, defining the average square velocity $\iint fv^2dxdv/N_e \equiv \langle v^2\rangle$, and the average velocity $\iint fvdxdv/N_e \equiv \langle v\rangle$ we can write

$$\frac{\partial\langle v^2\rangle}{\partial t} + \frac{2e}{m}E\langle v\rangle = 2D - 2\gamma\langle v^2\rangle. \tag{5.9}$$

Now by multiplying equation (5.7) by v and repeating the same procedure we get

$$\frac{\partial}{\partial t}\iint fvdxdv + \frac{eE}{m}N = -\gamma\iint fvdxdv \tag{5.10}$$

which leads to the following expression

$$\frac{\partial\langle v\rangle}{\partial t} + \frac{eE}{m} = -\gamma\langle v\rangle. \tag{5.11}$$

Multiplying this equation by $-2\langle v\rangle$

$$-\frac{\partial\langle v\rangle^2}{\partial t}-\frac{2eE}{m}\langle v\rangle=2\gamma\langle v\rangle^2. \tag{5.12}$$

Summing equations (5.9) and (5.12):

$$\frac{\partial}{\partial t}\langle(v-\langle v\rangle)^2\rangle=2D-2\gamma\langle(v-\langle v\rangle)^2\rangle \tag{5.13}$$

But $m\langle(v-\langle v\rangle)^2\rangle\equiv k_BT_e$, and we get

$$\frac{\partial T_e}{\partial t}=2\frac{Dm}{k_B}-2\gamma T_e. \tag{5.14}$$

Then taking the formula $D=\gamma k_BT_i/m$ and assuming a constant lattice temperature T_i, we finally achieve equation

$$\frac{\partial T_e}{\partial t}=-2\gamma(T_e-T_i) \tag{5.15}$$

which is the two-temperature equation for the electron temperature with $2\gamma=g/c_e$ and $P=0$.

5.3 Relaxation of the electron temperature

In this chapter we study the electron dynamics after the inclusion of the dissipation term. We are particularly interested in the energy exchanges between the electrons and the lattice. We concentrate on sodium films, for which $\omega_p^{-1}=0.11$ fs, $L_F=0.12$ nm, and $T_F=3.62\times10^4$ K. In the forthcoming simulations, the film thickness is $L=50L_F$. The excitation ranges from $\delta v=0.06v_F$ to $\delta v=0.35v_F$ and corresponds to an excitation energy $E^*/E_F=\overline{n}_iL(\delta v/v_F)^2$. For $\delta v=0.1v_F$, E^* is approximately equal to the energy absorbed by a sodium nanoparticle of radius $R=1$ nm irradiated by a laser pulse of intensity $I=10^{12}$ Wm^{-2} for a duration $\tau=100$ fs ($E^*=I\tau\pi R^2$)[12]. Although the numerical results reported in the next sections were performed in the Hartree regime, we checked that the exchange-correlation potential does not alter any of the conclusions.

The evolution of the electron temperature for three values of the excitation is presented in figure 5.2. We can clearly see, in all cases, the initial heating of the electron gas, with a peak value of temperature of a few thousand degrees. After reaching the maximum value, as time goes on, the electrons start cooling down by exchanging energy with the phonon bath.

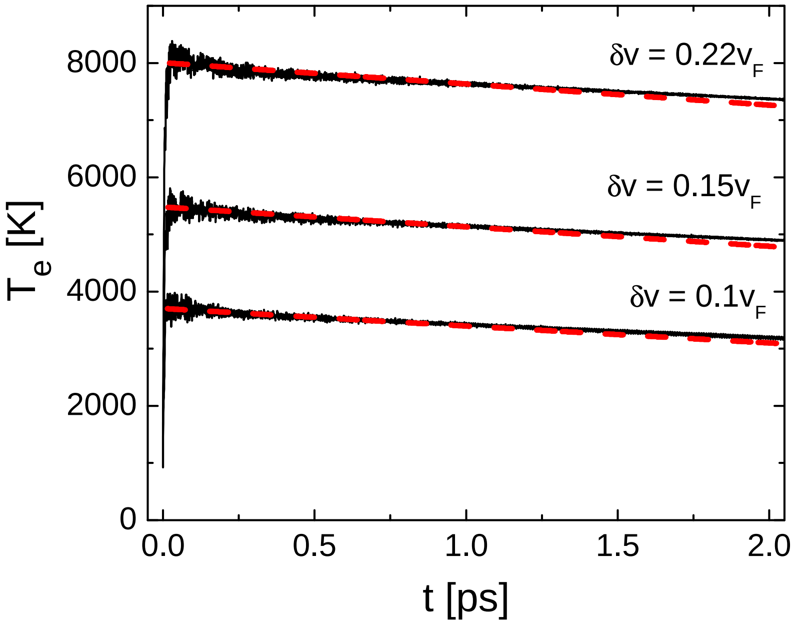

Figure 5.2: Time evolution of the electron temperature for three values of excitation at the ground state temperature $T_e = T_i = 1000$ K. The red dashed lines corresponds to results from two-temperature model.

The results of our Wigner calculations can be compared with those obtained with a simple TTM. In order to have a meaningful comparison we need to impose some necessary conditions on the TTM. First of all, our model does not include the change of the lattice temperature and we keep T_i fixed throughout the entire simulation (T_i is equal to the initial ground state temperature $T_i = T_e(0)$). Thus the ions are assumed to constitute a perfect reservoir with infinite heat capacity.

Another complication arises form the laser excitation $P(t)$. As in our model the excitation is in the form of a uniform shift δv of the electron distribution in velocity space, it is difficult to find simple connection between that kind of excitation and the laser term $P(t)$. This problem is solved by simply omitting the excitation process and just focusing on the relaxation stage. This can be achieved by setting the initial electron temperature in the TTM to be equal to the peak temperature observed in the Wigner simulations, which occurs around $t_{peak} = 50$ fs. The conditions imposed on the TTM lead to the expression given by (5.15) and the solution of this equation is what we actually compare with the Wigner results.

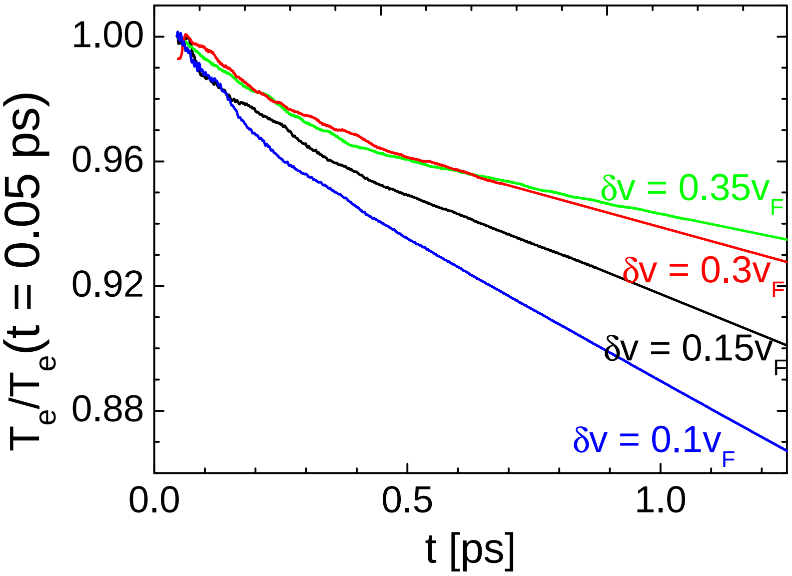

Figure 5.3: Time evolution of the running average of the electron temperature for various excitation energies.

As can be seen in figure 5.2 the agreement between the TTM and the Wigner simulations is quite impressive, and thus provides a direct confirmation of the validity of the TTM. This is an important issue, as the TTM is extremely popular as a phenomenological tool to interpret the electron relaxation curves obtained from experiments on thin metal films and nanoparticles.

Looking at the figure 5.2 we can infer that the temperature relaxation times τ_R are of the order of a few picoseconds, although their actual values are difficult to estimate as the decay is so slow and it would involve enormous computation time to see all the relaxation. Nevertheless, the trend can be extracted (figure 5.3) by using the running average of the electron temperature, defined as

$$\langle T_e \rangle(t) = \frac{1}{2T} \int_{t-T}^{t+T} T_e(t')dt' \tag{5.16}$$

with $T = 25$ fs. This enables us to smooth out the fast oscillations and highlight the long-time trend. Figure 5.3 presents the normalized evolution of the running average of the electron temperature. The curves start at $t = 50$ fs in order to eliminate the initial stage of the temperature grow, focusing on the long time behavior, and is normalized to the value of the temperature at the starting point.

In our simulations the relaxation time increases for larger excitation energies, in agreement with many experimental results and simulations based on the TTM [12, 58]. From such short runs it's difficult to extract the actual relaxation time, but for low excitation it appears to be around 3 ps.

5.3.1 Relaxation to classical equilibrium

Another way of highlighting the relaxation of our system toward a classical equilibrium, is by showing a cross-cut of the electron Wigner distribution at the midpoint of the film, $f(x = 0, v)$. In figure 5.4 we present such cuts for different times and two values of the excitation. In case of small perturbation ($\delta v = 0.06 v_F$), the electron distribution relaxes very fast and for time $\omega_p t = 10^4$ is virtually identical to the Fermi–Dirac equilibrium f_{eq}. In particular, no appreciable negative values of f are visible, except for the short times. In contrast, for $\delta v = 0.3 v_F$, the Wigner distribution is still significantly far from equilibrium, and negative values are clearly present. Such high excitation causes a strongly out-of-equilibrium situation and complete relaxation to the classical equilibrium requires much longer times.

5.4 Decoherence time

The relaxation time measures the speed at which the energy is exchanged between the electrons and the lattice. Another relevant time scale is given by the decoherence time, which represents the typical time over which quantum correlations are lost to an external environment (here, the ion lattice). After an inelastic scattering event, the energy of the electron changes, and the phase of the wavefunction is randomly distributed between 0 and 2π: in this way the quantum coherence progressively vanishes. In a density–matrix language, the relaxation time corresponds to the decay of the diagonal terms, whereas the decoherence time is related to the nondiagonal terms. In our representation the decoherence time is not exactly the same as in the density matrix approach, and we define it as the loss of the quantumness [59] due to electron–phonon coupling.

In order to evaluate the decoherence time τ_D, we recall that $f(x, v, t)$ can take negative values. The degree of "classicality" a Wigner distribution can be estimated from the weight of its negative parts [33], which leads us to define the quantity $S(t) = \int \int f_{<} dx dv$

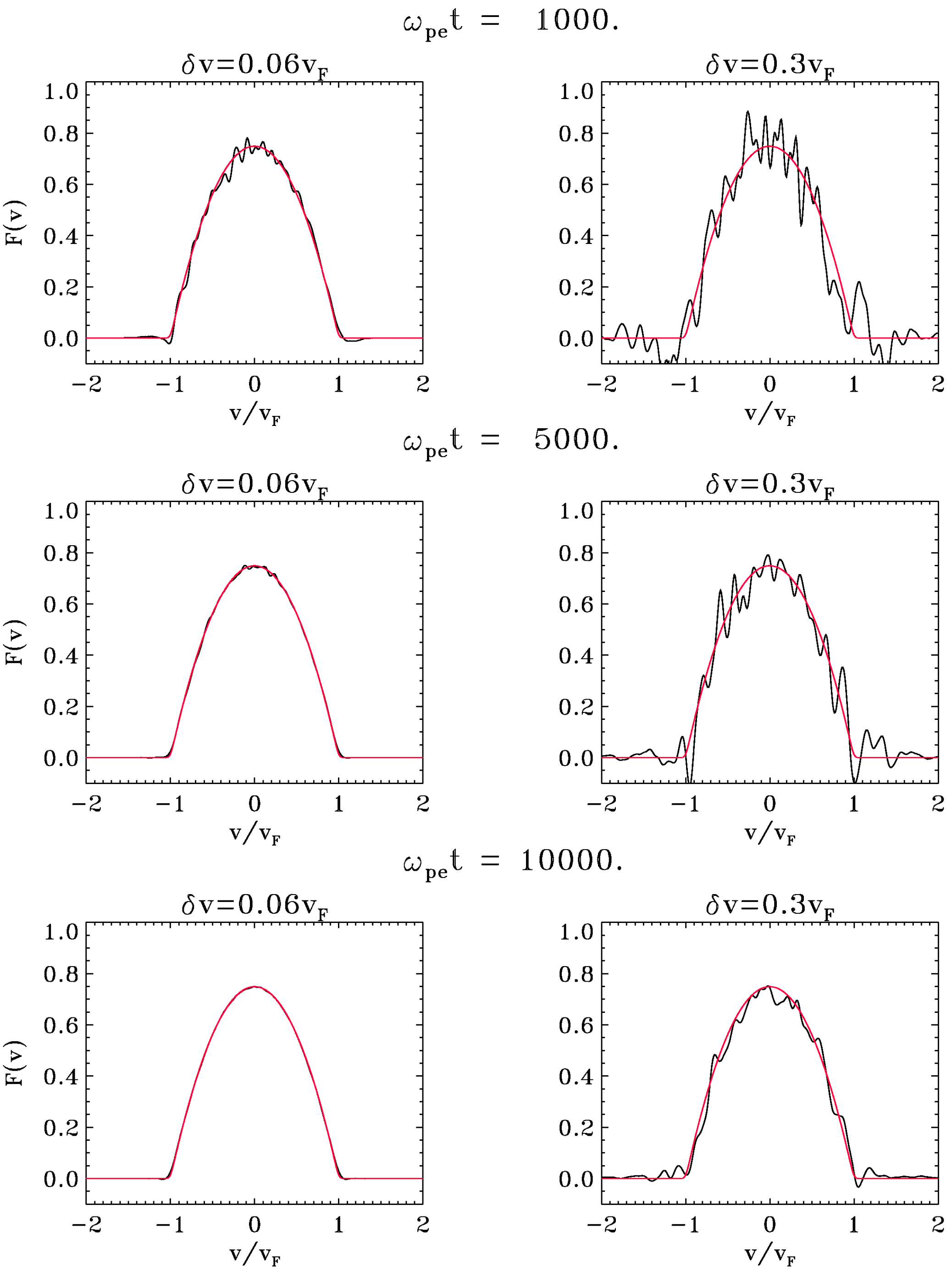

Figure 5.4: Wigner distribution at the midpoint of the film, for different times and two values of the excitation. The red curve represents the Fermi-Dirac equilibrium f_{eq}.

where:

$$f_{<} = \begin{cases} -f & \text{when f} < 0 \\ 0 & \text{elsewhere} \end{cases} \tag{5.17}$$

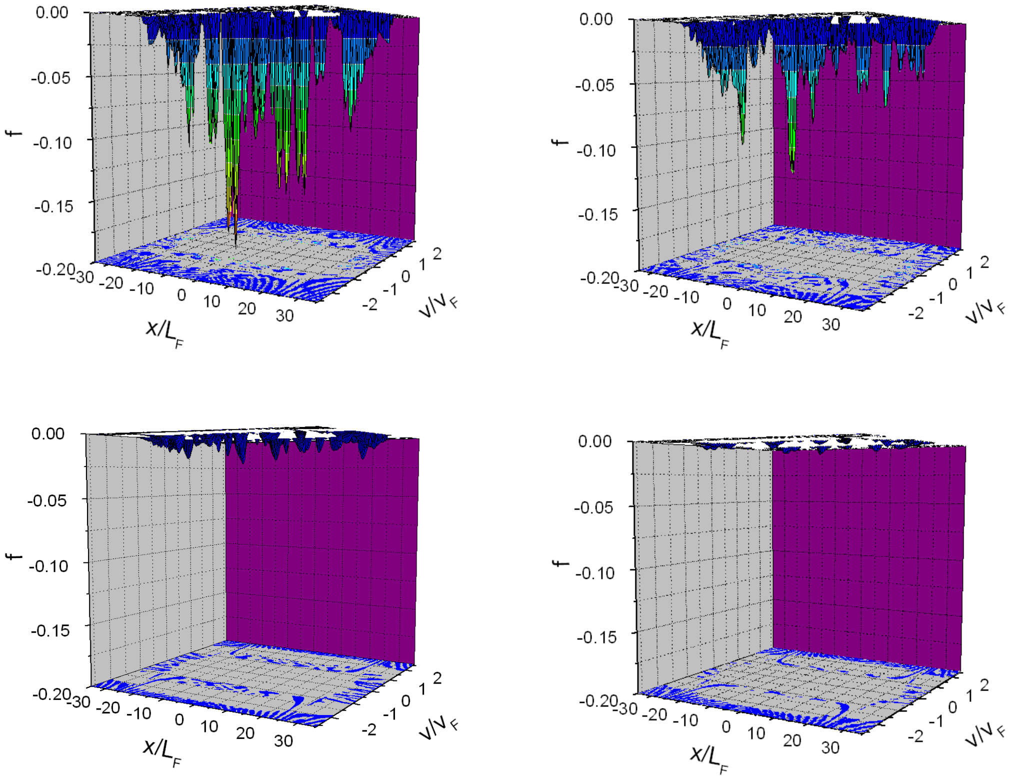

Figure 5.5: Negative part of the Wigner function at $\omega_p t = 1000$, $\omega_p t = 5000$, $\omega_p t = 10000$, and $\omega_p t = 20000$, for the excitation $\delta v = 0.22 v_F$

The decoherence time τ_D can be estimated by fitting $S(t)$ with a simple decaying exponential function $S_{fit}(t) = S_0 + A \exp(-t/\tau_D)$. The negative parts of the Wigner function in phase-space are presented in figure 5.5 for different times. As time goes on, the quantum distribution loses its negative values and becomes more and more classical.

5.4.1 Excitation dependence

The typical behavior of the "negativity" of the Wigner function is presented in figure 5.6. In the time evolution of this quantity we can distinguish two stages: first, soon after the initial excitation, the electron distribution function gains quite significant negative values; subsequently, it decays exponentially to zero. The ground state temperature here is $T_e = 1000$ K and even for the time $t = 0$ we can still observe some negative values, which disqualify the Wigner function as a real probability distribution.

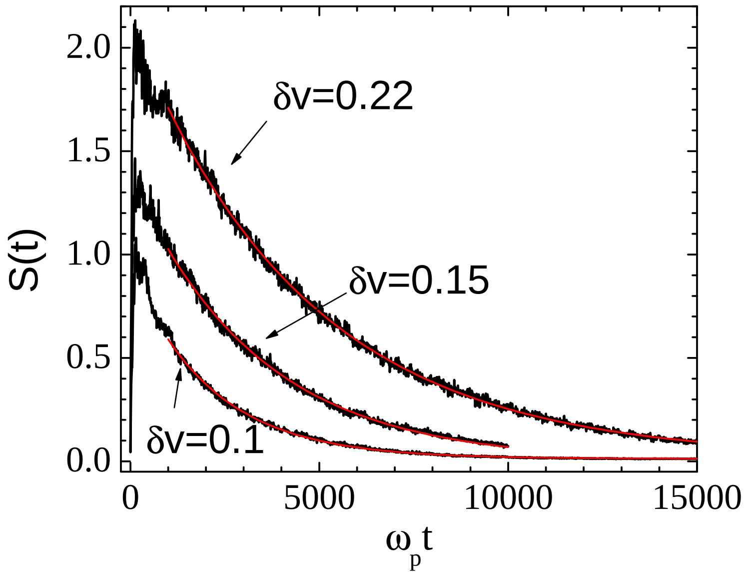

Figure 5.6: Evolution of $S(t)$ for different excitations, together with exponentials fits (red lines).

The decoherence time as a function of the excitation is shown in figure 5.7. Similarly to the relaxation time, it increases with increasing energy of excitation. With higher energy injected into the system, the decoherence time becomes longer and longer.

The typical decoherence time obtained in our simulations is of the order of 1 ps (as $10000\omega_p^{-1} \approx 1.1$ ps) and is related to the electron–phonon coupling. The electron–electron interactions, in our representation, are not explicitly included and are reflected through the mean field. Nevertheless the typical electronic process, such as Landau damping, is visible in our simulation and occurs at the times scales around 20 fs (which can be seen in figure 4.4). This effect shows that the decoherence due to electronic processes is of the same order of magnitude as in the experimental observations [60].

5.4.2 Temperature dependence

According to Fermi–liquid theory [61], the decoherence time τ_D is constrained by any inelastic dissipation effects, like electron–electron, and electron–phonon interactions, or scattering of electrons from magnetic impurities. In the absence of any extrinsic sources of decoherence, τ_D is dominated by electron–electron and electron–phonon interactions.

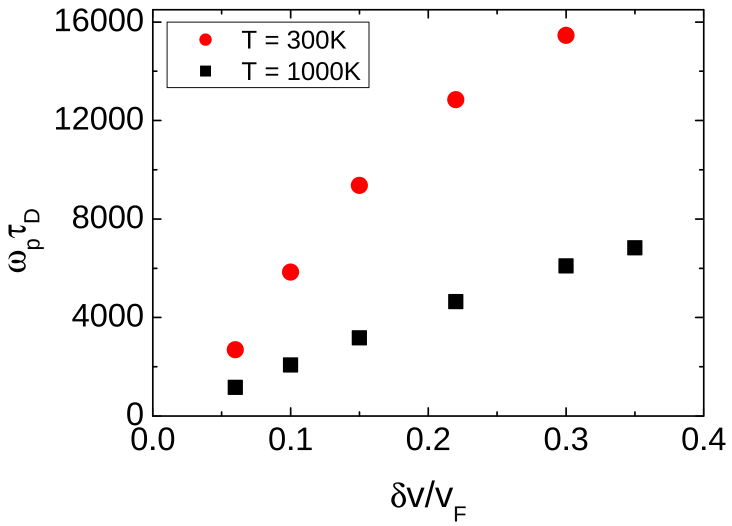

Figure 5.7: The decoherence time as a function of the excitation for two temperatures $T_e = 300$ K, and $T_e = 1000$ K.

In the Fermi–liquid theory without any dissipation, the lifetime of quasiparticles follows a $(E - E_F)^{-2}$ power law. The inclusion of the disorder and the dimensionality of a system leads to expression given by Altshuler [61]

$$\tau_D = \left(\frac{D\nu_d}{T}\right)^{\frac{2}{4-d}} \tag{5.18}$$

where D is the electron diffusion coefficient, d is the sample dimensionality, and ν_d is the density of states for the corresponding dimensionality.

The temperature behavior of the decoherence time has recently been the subject of a controversial debate. Due to phase breaking mechanisms, τ_D is expected to diverge as the temperature goes to zero. Even at zero temperature, the electrons are scattered by static defects like impurities or the edge of the sample. Such interactions, however, represent elastic scattering events during which the energy is conserved, so they don't change phase of the electron wavefunction, and should not lead to the decoherence.

Contrary to this expectation, in some experiments [62] a systematic low–temperature saturation of τ_D has been observed. This finding started a controversial debate whether this saturation is intrinsic or extrinsic. The intrinsic saturation at zero temperature was explained by electron–electron interactions in the ground state [63]. On the other hand,

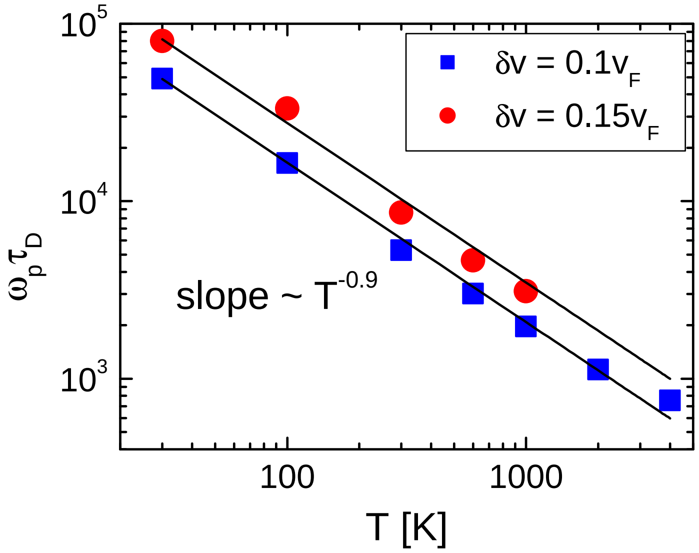

Figure 5.8: The decoherence time τ_D as a function of the temperature for two different excitations.

this effect can also be justified by various extrinsic phenomena such as the presence of dynamical two–level systems, or the presence of small magnetic impurities [64]. None of those mechanisms, however, has been able to exclude the possibility of an intrinsic saturation.

The temperature behavior of the decoherence time for our model is presented in figure 5.8. This quantity follows the power low $T^{-0.9}$ for two presented values of the excitation. The exponent is very close to unity, which results from the equation (5.18) for a 2D electron gas.

In our model we include only electron–phonon coupling and long range electron–electron interactions, which are hidden in the mean field. By virtue of these arguments our calculations contain only intrinsic mechanisms which play a role in the dissipation processes. In our numerical results we do not observe any apparent saturation in the temperature dependence of τ_D which can suggest, in agreement with the conclusion given in [65], that the saturation of the decoherence time can be caused by the external scattering. For the semiconductors the saturation was noticed for the temperatures less than 1 K, for metals however, this temperature should be much larger because of the higher electron density.

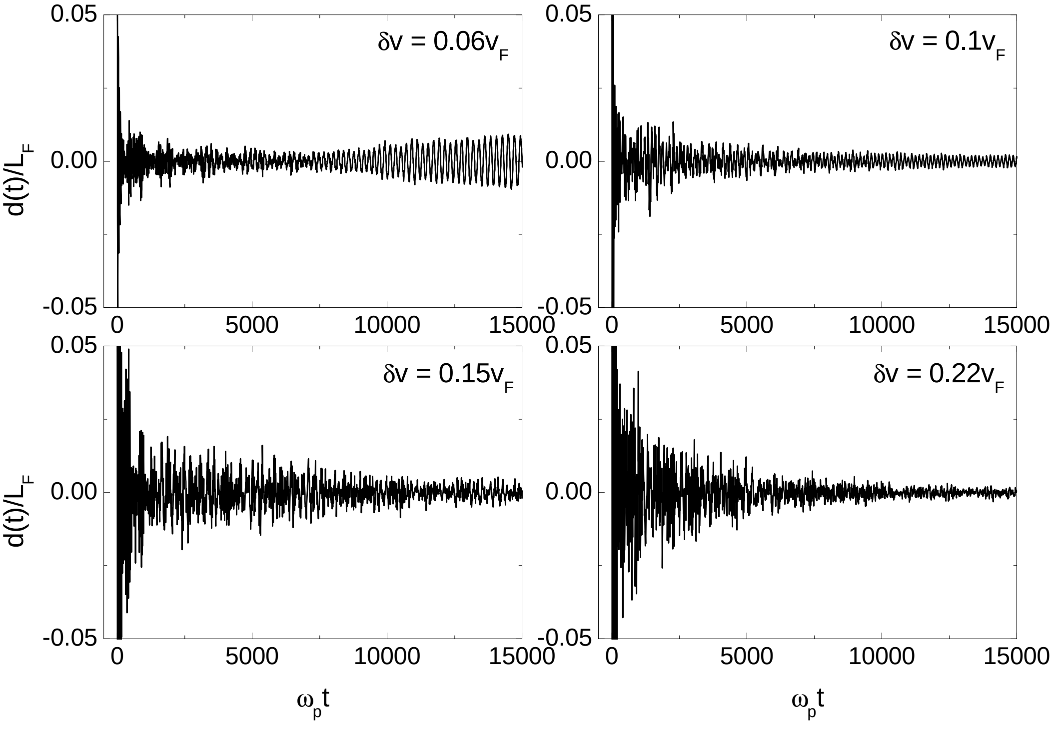

Figure 5.9: Time history of the electric dipole evolution for different excitation energy at $T_e = 300$ K.

5.5 Evolution of the electric dipole

Another interesting effect of the electron–lattice interaction can be observed in the behavior of the electric dipole (3.28). Figure 5.9 shows a direct comparison of this quantity for different values of the excitation. As was described in earlier chapters, the initial phase of the evolution features collective oscillations of the electron gas at the plasma frequency. Those oscillations are exponentially damped, after which we can observe other processes connected with the energy relaxation. The time evolution of the electric dipole without the dissipation term (see figure 4.3) revealed that the oscillations do not vanish completely and we can observe some irregular revivals, that are slightly suppressed but still visible until the end of the run.

An intriguing effect can been observed in the behavior of the dipole after the electron–phonon coupling has been introduced. In the case of the low excitation energy, after

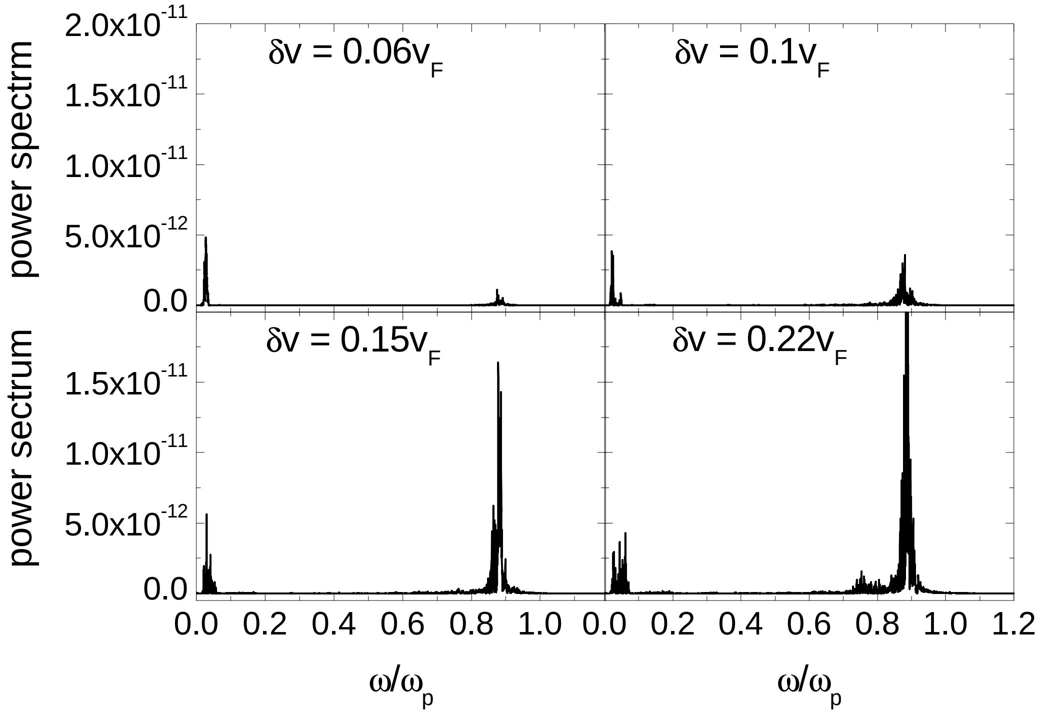

Figure 5.10: Frequency spectrum of the electric dipole at different excitations.

initial collective oscillations, and their subsequent damping, around the time $\omega_p t = 7000$ the dipole oscillations show up anew with increasing amplitude. The frequency of these oscillation is quite well defined ($\omega = 0.027\omega_p$), as can be seen in the top left panel of figure 5.10, and their magnitude is larger than that of the peak representing plasma oscillations ($\omega = 0.878\omega_p$). The amplitude of those oscillations decreases with the excitation, and for high disturbances we observe the situation similar to that without electron–phonon interactions.

Going back to the figure 5.10, where we show the power spectrum of the electric dipole for different excitations, we clearly see that the plasmon oscillations become more significant with increasing perturbation, whereas the amplitude of the low frequency oscillations stays more less the same (although some new frequencies show up).

5.6 Discussion

From the above results, it appears that the electron–lattice interactions can be correctly described by two typical timescales, namely, the relaxation time $\tau_R \approx 3$ ps and the decoherence time $\tau_D \approx 0.25$ ps for $\delta v = 0.1 v_F$ (these are often referred to as T_1 and T_2 in the semiconductor literature [66]). The relaxation time observed in the simulations is in good agreement with that measured in experiments on small sodium clusters [12].

The overall electron thermalization thus occurs in two stages. First, quantum correlations are lost to an external environment due to decoherence process, during which the Wigner distribution loses its negative values and tends to a classical Fermi-Dirac function with temperature $T_e \gg T_i$. This is consistent with experimental observations, which shows a thermal distribution of emitted electrons (with T_e a few thousand degrees) soon after the laser irradiation of sodium clusters [67]. Subsequently, the electron gas cools down until it reaches the lattice temperature. This relaxation process occurs on a timescale $\tau_R \gg \tau_D$.

The decoherence times emerge naturally from the equations and its scalings with the temperature is very close to the theoretical prediction for two dimensional systems. We do not see also any sign of the saturation of the decoherence time at low temperatures. As we do not include any extrinsic dissipation mechanism, this fact can suggest that the observed in experiments [62] low-temperatures saturation of τ_D is not intrinsic.

Chapter 6

Ground-state fidelity in nonparabolic quantum wells

6.1 Introduction

Another issue we would like to bring up in this thesis is the stability of a quantum system against perturbations from the environment. An interesting measure of the robustness of a quantum system is given by the Loschmidt echo [68], which describes the stability properties of the system under imperfect time reversal. When the system is allowed to evolve under the action of an unperturbed Hamiltonian H_0 until time t, then it is evolved backwards in time until $2t$ with the original Hamiltonian plus a small perturbation $H_0 + \delta H$ (the "environment"), the square of the scalar product of the initial and final states defines the quantum Loschmidt echo. The overlap of two systems evolving in two different Hamiltonians can be written mathematically as

$$M(t) = \left|\langle\psi_0 \mid e^{i(H_0+\delta H)t/\hbar} e^{-i(H_0)t/\hbar} \mid \psi_0\rangle\right|^2 , \tag{6.1}$$

where ψ_0 is the initial wavefunction.

The idea of Loschmidt was revived recently in the context of quantum information theory, as the attempt at coding information using quantum bits is prone to failure if a small coupling to an uncontrollable environment destroys the unitary evolution of the wave function.

An equivalent approach to the Loschmidt echo was proposed by Peres [69] in terms of the so-called quantum fidelity. Peres noted that the stability of a quantum system against external perturbations can be measured by the overlap of two wavefunctions evolving in slightly different Hamiltonians (unperturbed H_0, and perturbed $H = H_0 + \delta H$). The quantum fidelity at time t is then defined as the square of the scalar product of the wavefunctions evolving in these Hamiltonians:

$$F(t) = |\langle \psi_{H_0}(t) \mid \psi_H(t) \rangle|^2 . \tag{6.2}$$

In this chapter, we aim to provide characterization of the ground-state fidelity in semiconductor quantum wells. We shall use the static definition of the fidelity, represented by the overlap of the scalar product, between two ground-states corresponding to two slightly different Hamiltonians:

$$F(l) = |\langle \psi_{H_0}(l) \mid \psi_H(l) \rangle|^2 . \tag{6.3}$$

where l corresponds to the energy level.

The concept of the ground-state fidelity has been recently applied to the analysis of the quantum phase transitions (QPTs) [70–73]. The idea underlying this method is that in the neighborhood of critical regions a small change of the Hamiltonian parameters can give rise to dramatic ground-state variations, due to the strong difference of the ground-state structure in opposite phases. The overlap between neighboring states is then expected to decrease abruptly at the phase boundaries. Here we will focus just on a measure of similarity between states described by sightly different Hamiltonians.

Small semiconductor devices, such as quantum dots and quantum wells, have been recently in focus of intensive studies, particularly for possible applications in the emerging field of quantum computing [74]. The electronic devices based on solid–state have the advantage over other competing approaches [75] (ion traps, neutral atoms, superconducting circuits, etc), because of the long experience acquired on semiconductor microelectronics. The implementation of basic qubit operations is mostly based on use of the electron spin states. Nevertheless, to manipulate the electrons themselves, it is still necessary to resort to electric fields, either static (dc) [76] or oscillating (laser pulses) [77].

In the parabolic quantum well symmetry, the parabolic potential $V_{conf} = Ax^2$, mimics the potential created by a uniform slab of positive charge of density $\overline{n}_i$. Electrons are introduced remotely in the quantum well by placing donors at some distance from either side of the well. The electrons enter the well to screen the parabolic potential and distribute themselves in a uniform layer. Because the separation of the donors from the electrons can reach several hundred Angstroms in such a system, the electron

Table 6.1: Typical parameters for metallic and semiconductor nanostructures

	Units	Metal film	Quantum well
n_e	m^{-3}	10^{28}	10^{22}
m	–	m_e	$m^* \simeq 0.067m_e$
ε	–	ε_0	$\varepsilon \simeq 13\varepsilon_0$
ω_p^{-1}	fs	1	1000
E_F	eV	1	0.001
T_F	K	10^4	100
L_F	nm	0.1	10
a_0	Å	0.529	102
$a_{lattice}$	Å	5	5
r_s/a_0	–	4	3

impurity interactions are considerably smaller than it is possible in the usual doped semiconductors.

In the samples used in experiments, the parabolic quantum wells can be achieved by tailoring the conduction band edge of an alloy of semiconductors, usually $\mathrm{Ga}_{1-x}\mathrm{Al}_x\mathrm{As}$. Since the band offset between GaAs and $\mathrm{Ga}_{1-x}\mathrm{Al}_x\mathrm{As}$ is proportional to x, a parabolic confinement can be obtained by varying the fraction of aluminum quadratically with position [78].

Metallic and semiconductor nano-objects operate in very different regimes, as the electron density is several orders of magnitudes larger for the former. Consequently, the typical time, space, and energy scales can be very different, as illustrated in table 6.1. However, if we take into account the effective electron mass and dielectric constant, the relevant dimensionless parameters turn out to be rather similar. For example, the Wigner-Seitz radius r_s commonly used in the solid state physics, normalized to the effective Bohr radius $a_0 = 4\pi\varepsilon\hbar^2/me^2$ is of the same order for metals and semiconductors. It is therefore not surprising that the electron properties of both types of nanostructures can be described by means of similar models, and because those similarities we would like to use the method described in Chapter 2 to investigate semiconductor quantum wells.

6.2 Model

In order to study the ground-state fidelity we investigate a system of electrons confined in a nonparabolic quantum well, interacting through their Coulomb mean field. The ground-state properties of this system can be obtained from the solution of the one-dimensional Kohn–Sham equation

$$\left[-\frac{\hbar^2}{2m^*}\frac{d^2}{dx^2}+V_{Hartree}(x)+V_{conf}(x)\right]\psi_{H_0}(l)=\varepsilon_l\psi_{H_0}(l). \tag{6.4}$$

where m^* is the effective mass of the carriers in the well, $V_{Hartree}$ represents the electric potential generated by all the electrons (obtained from the solution of Poisson's equation), $\psi_{H_0}(l)$ and ε_l are the stationary wave functions and the associated energy eigenvalues. The confining potential is composed of a harmonic part with a small quartic component:

$$V_{conf}(x)=\frac{e\overline{n}_i}{\varepsilon}\left(\frac{1}{2}x^2+\frac{K}{12}x^4\right), \tag{6.5}$$

where K represents the anharmonicity factor.

In order to investigate the quantum fidelity relative to the Hamiltonian H_0, we add a small perturbation δV, from which we obtain the perturbed eigenstates $\psi_H(l)$. Having calculated the wavefunctions for both system we make use of the definition of the static ground-state fidelity

$$F(l)=\left|\int\psi^*_{H_0}(l)\psi_H(l)dx\right|^2. \tag{6.6}$$

The quantum fidelity $F(l)$ describes the overlap between the wavefunctions corresponding to the same energy state. It is possible to obtain more general quantity describing the whole system, not only individual states, by summing all the contributions from individual states represented by the total fidelity

$$F_{tot}=\sum_{l=1}w_lF(l) \tag{6.7}$$

where w_l stands for occupation probability (at $T_e=0$)

$$w_l=\frac{m^*}{\pi\hbar^2L\overline{n}_i}(E_F-\varepsilon_l), \tag{6.8}$$

where L is the width of the quantum well, and E_F is the Fermi energy.

In this chapter we consider the quantum well of width $L=78a_0\approx 8000$Å. We focus our attention on the ground-state configuration at $T_e=0$ K, for which we obtain 28 occupied states. The numerical method used to solve (6.4) is described in section 2.1.3.

6.3 Numerical result

6.3.1 Unperturbed system

The ground-state properties of our system, in the unperturbed case, are mostly determined by the parameter K appearing in (6.5), which describes the deviation form a parabolic potential (anharmonicity). In case of a purely parabolic system, the density profile (blue solid line in figure 6.1) is similar to what we observed for thin metal films. Of course the details of the calculation of the effective potential and the resulting density profile are different, but we can still observe the same Friedel oscillations, which are an indication of the quantum confinement of the electrons.

After inclusion of the small anharmonic term to the confining potential the above picture changes, as we can see in figures 6.1 and 6.2. The density profile grows from the middle of the well to the edges and has the largest value near the borders, where the quartic terms is dominating. The effective potential is no longer flat at the bottom and its shape strongly depends on the value of K.

The anharmonic term in the confining potential has an important influence on the energy levels and corresponding wave functions. The change of the potential in the middle of the well, amounts to the creation of two "separate" wells, which the electrons can occupy with equal probability. This effects leads to the degeneracy of the lowest state, which is shown in figure 6.3 and the corresponding table. For example, the first two states have the same energy $\varepsilon_1 = \varepsilon_2 = 0.078E_F$, and are situated in the two separated wells. A first small difference between the energy levels can be found for $\varepsilon_7 = 0.273E_F$ and $\varepsilon_8 = 0.278E_F$ which lie near the top of the new wells. The wave functions for these states have a finite probability only within the two separate wells, and vanish at the center of the system. For higher energy states, where we do not observe degeneracy anymore and the energy levels are separated, the situation is more similar to what we observe for normal parabolic confinement.

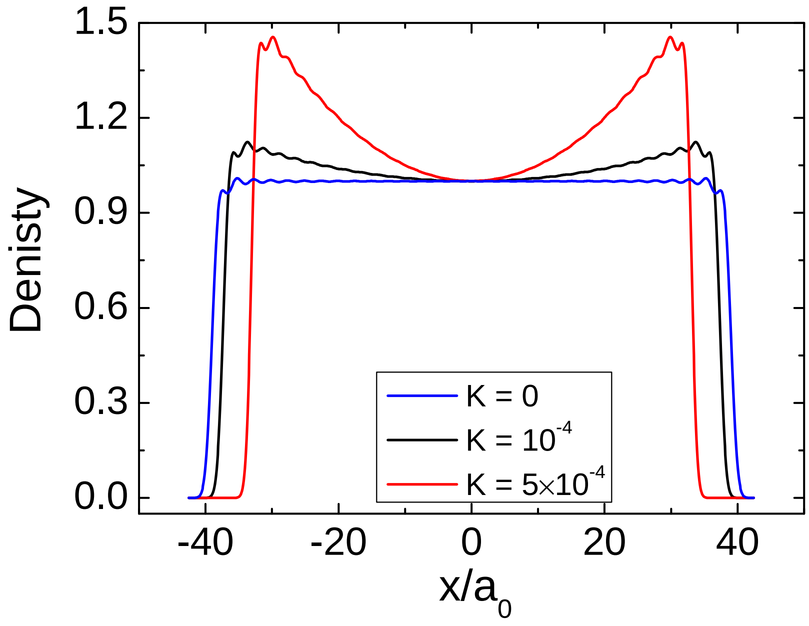

Figure 6.1: Normalized density profiles for different values of the anhamonicity factor K.

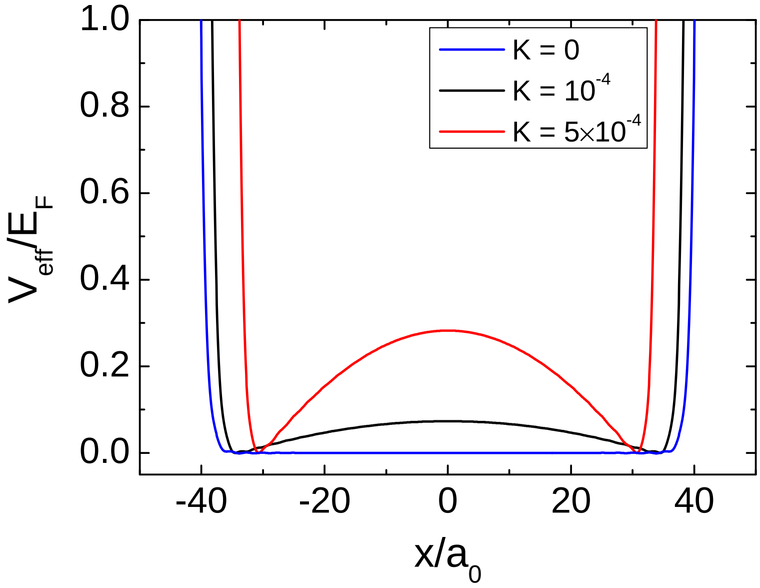

Figure 6.2: Effective potential for different values of K.

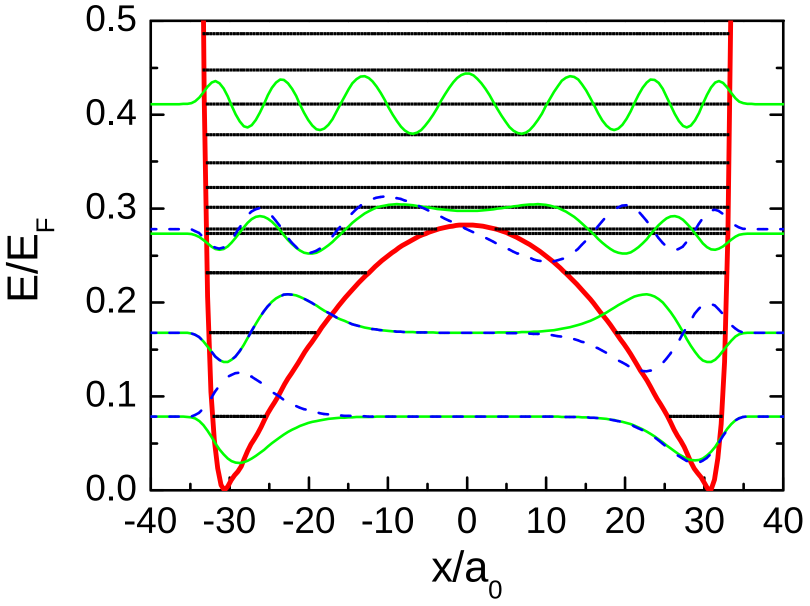

l	ε_l/E_F
1	0.078
2	0.078
3	0.168
4	0.168
5	0.231
6	0.231
7	0.273
8	0.278
9	0.301
10	0.322

Figure 6.3: Energy levels and wave functions in nonparabolic quantum well of thickness $L = 78a_0$. The green solid lines represent respectively ψ_1, ψ_3, ψ_7, and ψ_{13}, while the blue dashed lines corresponds to ψ_2, ψ_4, and ψ_8. In the table we present the exact values of energy levels to highlight the degeneracy of the lowest states.

6.3.2 Ground-state fidelity

In our model the perturbation of the Hamiltonian δV is realized by adding a random potential consisting of the sum of a large number of uncorrelated waves

$$\delta V = -\frac{e\overline{n}_i}{\varepsilon}\epsilon \sum_{j=1}^{N_{max}} \left(\frac{L}{2\pi j}\right)^2 \cos\left(\frac{2\pi j}{L}x + \alpha_j\right) \tag{6.9}$$

where ϵ is the amplitude of the perturbation, and α_j's are random phases. Here we will focus on the dependence of the fidelity on the amplitude ϵ.

The procedure of computing the quantum fidelity of our system runs as follows: first, we solve the Kohn–Sham equation (6.4) with unperturbed potential in order to find $\psi_{H_0}(l)$, then the same procedure is repeated including the perturbation δV to obtain $\psi_H(l)$, and finally we compute the fidelity given by (6.6).

Table 6.2: Calculated energy levels for different amplitudes of perturbation for $K = 10^{-4}$.

	ε_l/E_F			
l	$\epsilon = 0$	$\epsilon = 10^{-5}$	$\epsilon = 10^{-4}$	$\epsilon = 10^{-3}$
1	0.0336	0.0336	0.0335	0.0323
2	0.0336	0.0336	0.0336	0.0333
3	0.0635	0.0635	0.0634	0.0626
4	0.0643	0.0643	0.0642	0.0634
5	0.0777	0.0777	0.0776	0.0771
6	0.0868	0.0868	0.0868	0.0860
7	0.1003	0.1003	0.1003	0.0998
8	0.1162	0.1162	0.1161	0.1153
9	0.1346	0.1346	0.1345	0.1340
10	0.1552	0.1552	0.1551	0.1544

We first examine the influence of the perturbation ϵ on the energy levels. In table 6.2, we show the values of the lower energy levels ε_l for different amplitudes of the perturbation. In the case of small amplitudes, the energies are almost unaffected, and stay close to the value observed without the perturbation. Only very high disturbance changes appreciably the energy spectrum and we are even able to see small separation of the degenerate states. For $\epsilon = 10^{-3}$ the first two levels, which were initially equal $\varepsilon_1 = \varepsilon_2 = 0.0336E_F$, are now slightly separated by $\Delta\varepsilon_{2-1} = 0.001E_F$. Of course this separation is not large when we compare it with the energy difference between the levels 2 and 3 (which is equal to $\Delta\varepsilon_{3-2} = 0.03E_F$), but still we can talk about small degeneracy breaking in our system.

The wavefunctions are more sensitive to the perturbation than the energy levels themselves. Even for very small amplitude we are able to see the difference between the unperturbed and perturbed states. A measure of this difference is provided by the quantum fidelity, which is presented in figure 6.4 for two values of K. In both instances, the random potential has a significant influence only on the low energy states, for which a very small perturbation can change the wavefunctions. For example, for the first state ψ_1 (figure 6.5), in the unperturbed case the wavefunction has two symmetric peaks, whereas in the perturbed system we observe only one peak. This effect is a clear signature of

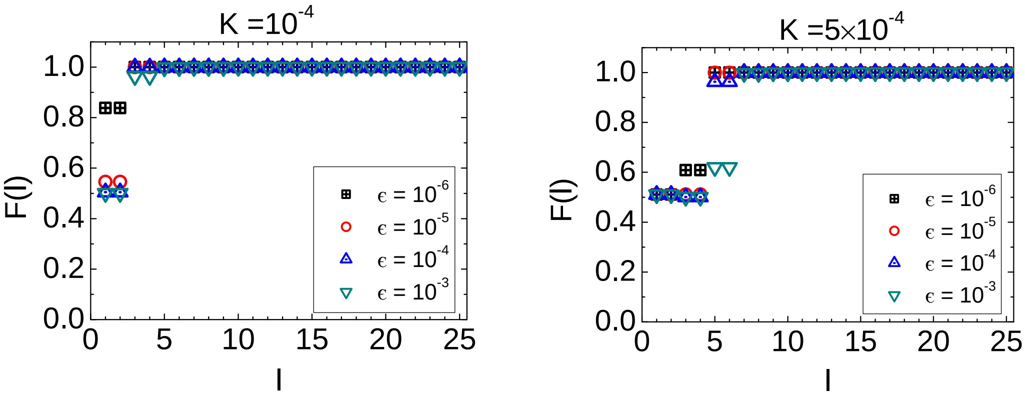

Figure 6.4: Quantum fidelity for different values of anharmonicity factor versus the level number.

symmetry breaking caused by the perturbation. The value of the fidelity for that state, $F_1 = 0.51$, is related to the fact that the perturbation shifted the probability from one well to the other. Similar probability shifts can be also noted for other states affected by the random potential. The number of the wavefunctions which underwent such a transition depends on the value of anharmonicity coefficient, and the strength of this change is controlled by the amplitude of the perturbation.

6.3.3 Total fidelity

In the analysis of the quantum fidelity in the previous section we focused on the individual states and their behavior after the perturbation was added. Now we would like to present a somewhat more general description of our system in terms of the total fidelity defined by (6.7). In this representation each individual state has a weight which determines its contribution to F_{tot}.

In figure 6.6 we present F_{tot} as a function of K, for different perturbations. For small enough K the total fidelity is equal to unity, that is the value which we obtain for unperturbed system. With increasing K we observe a roughly linear decrease of the total fidelity.

Another interesting feature of our system can be found when we plot the total fidelity as a function of the perturbation (figures 6.7 and 6.8). As we can see on the figures, even tiny disturbance can change the fidelity quite appreciably. The steps observed in

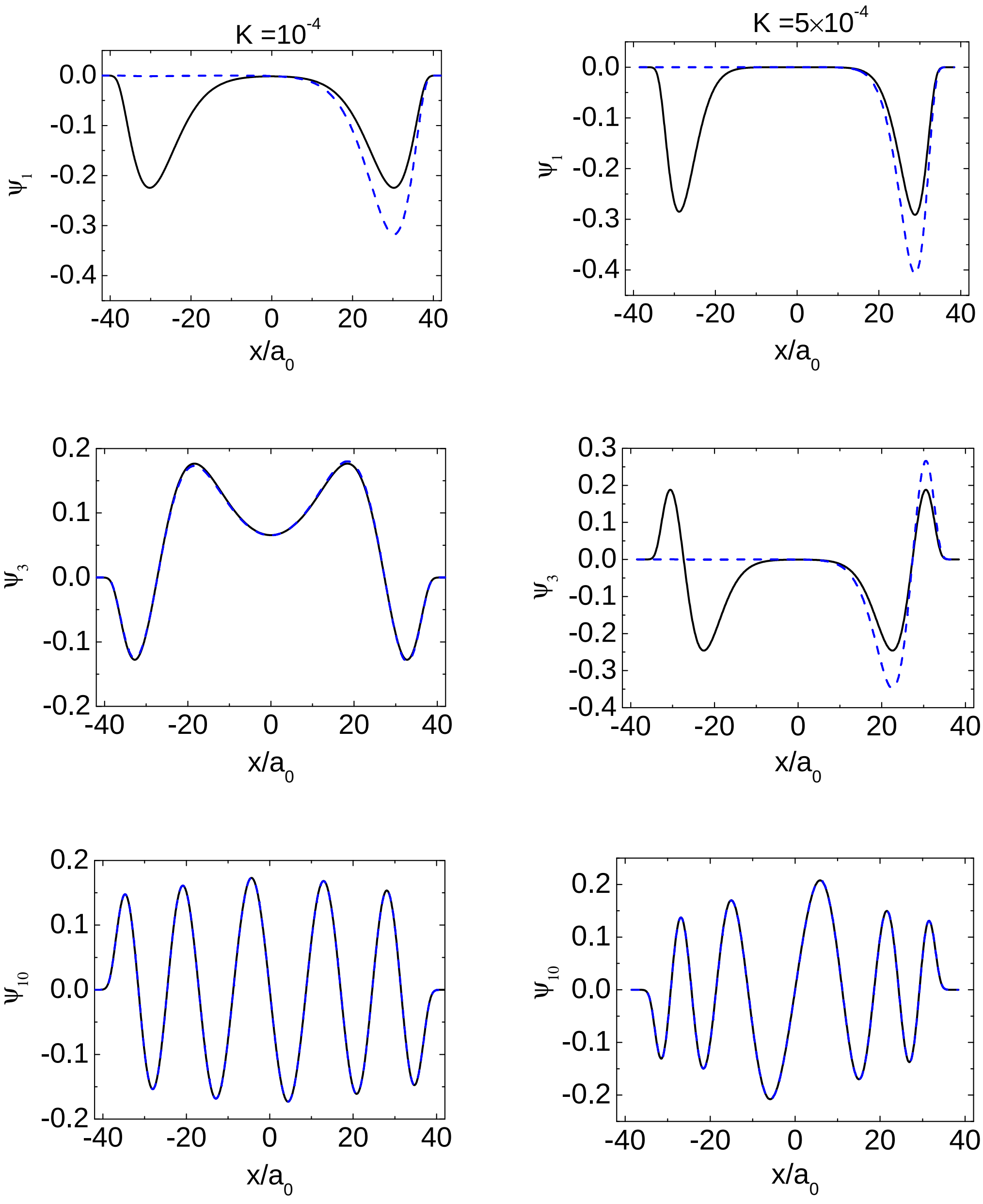

Figure 6.5: Unperturbed (black solid lines) and perturbed (blue dashed lines) wavefunctions for the perturbation $\epsilon = 10^{-4}$.

the plots of the total fidelity, reveal how the perturbation acts on the different systems. First, when the amplitude is not large enough, we do not see any change. After ϵ reaches a certain threshold value (around $\epsilon \approx 10^{-11}$), the first two states start to be affected and we observe the drop. For still increasing amplitude the perturbation is not strong enough to change another states and the fidelity stays constant. After reaching another

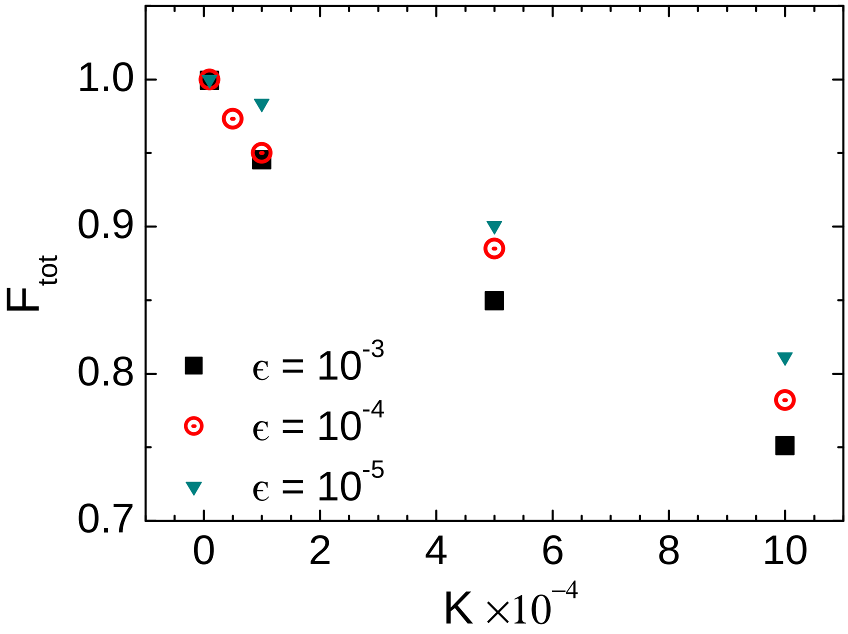

Figure 6.6: Total fidelity as a function of K for different amplitudes of the perturbation.

threshold value, once again the fidelity jumps and then remains almost unchanged until the next leap.

The discussion given above concerns the case with $K = 5 \times 10^{-4}$, where we can see three clear jumps around $\epsilon_{tr3} = 10^{-11}$, $\epsilon_{tr2} = 10^{-6}$, and $\epsilon_{tr1} = 10^{-4}$. For $K = 10^{-4}$ fewer states are affected by the perturbation and only two jumps are observed, which appear approximately for the same values of the perturbation ϵ_{tr1} and ϵ_{tr2}. In figures 6.7 and 6.8 we have presented the partial fidelity only for the odd states, as they are equal to the neighboring even states and give the same value of F_l.

6.4 Discussion

In this chapter, we have investigated the ground-state properties of an electron gas confined in a nonparabolic quantum well. We have considered two ground states corresponding to two slightly different Hamiltonians.

In the unperturbed system the main influence on the ground-state properties was

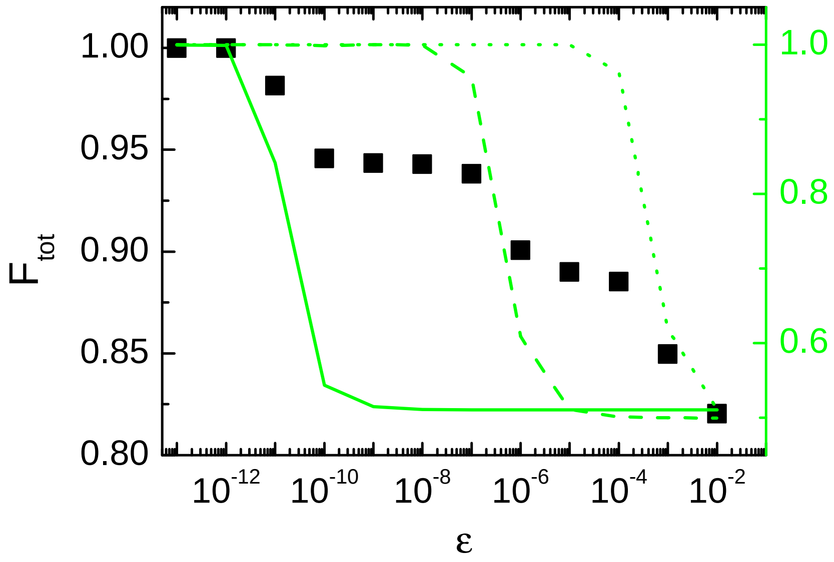

Figure 6.7: Total fidelity as a function of perturbation for $K = 5 \times 10^{-4}$ (black points), together with the fidelity for the individual states (green lines): F_1 (solid line), F_3 (dashed line), and F_5 (dotted line).

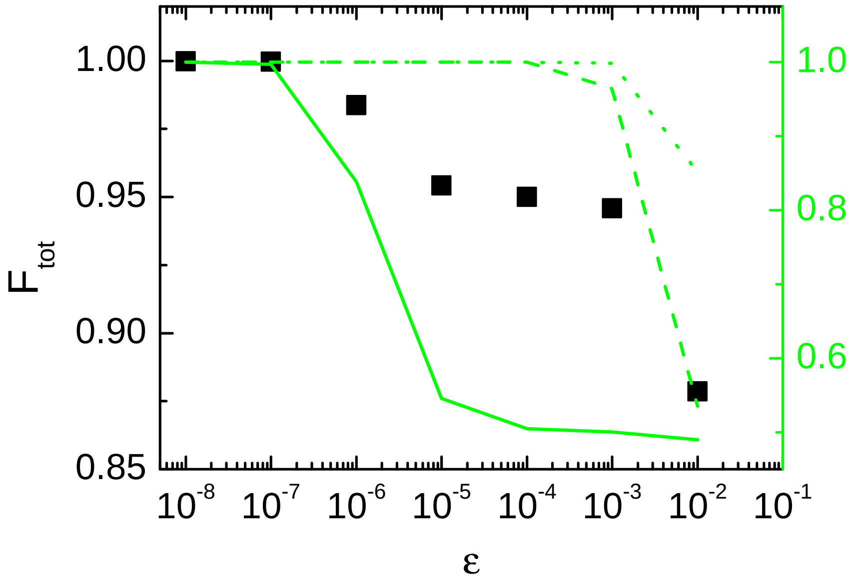

Figure 6.8: Same as figure 6.7 but for $K = 10^{-4}$.

determined by the anharmonicity coefficient. The quartic term included in the Hamiltonian created degenerate energy states in the two wells at the bottom of the effective potential.

After the random potential was added the energy levels were almost unaffected, and only a very large perturbation caused a small separation of the degenerate states. On the contrary, the wavefunctions show large sensitivity on the random disturbance. This effect could be observed in the behavior of the quantum fidelity, which measured the similarity between the unperturbed and perturbed systems. At first, it may be surprising that the wavefunctions representing the lowest, and not the highest states, are changed so easily. When we look, however, at the confining potential we can clearly see that the low energy states are more confined spatially that others, and this effect can facilitate symmetry breaking action of the random potential. The behavior of the total fidelity as a function of ϵ revealed several steps, which were connected with the perturbation affecting one state after another.

In summary, the random potential does not alter the energy spectrum of the electron confined in a nonparabolic quantum well, but the spatial probability of finding an electron can be changed significantly even by a small disturbance.

Chapter 7

Conclusions

7.1 Results of the thesis

The recent rise of interest in nanotechnology has lead to the development of new materials revealing promising and not hitherto observed effects. Understanding new phenomena in sub-micron objects, which have applications in the real world, is a matter of great importance in nanoscale science and engineering. In the present thesis, we have studied theoretically the ultrafast dynamics of the electron gas confined in thin metal films, which are widely used in modern high-speed electronic devices. We have concentrated here on the quantum effects resulting from the spatial confinement that leads to the discretization of the electronic states in the direction normal to the film surfaces.

Our numerical study of the electron dynamics was based on the use of microscopic kinetic methods, originally developed in nuclear and plasma physics. In these methods, the valence electron are assimilated to an inhomogeneous electron plasma. To follow the quantum electron dynamics, we made use of the Wigner equation coupled self-consistently to the Poisson equation. The Wigner representation is a useful tool to express quantum mechanics in a phase-space formalism, in which a quantum state is described by a Wigner function. The phase space formulation of quantum mechanics cannot have the same interpretation as in classical mechanics, because the Heisenberg uncertainty principle states that position and momentum cannot be known simultaneously with arbitrary precision. A consequence of the uncertainty principle is that the Wigner function can take negative values and thus cannot be regarded as a real probability density. Besides this particularly important inconvenience, the Wigner function satisfies most of the standard properties of probability distributions. The Wigner evolution equation in the classical limit reduces to the Vlasov equation.

Although the Wigner formalism is fully quantum, the quantization rules are not explicitly taken into account, and must be imposed by additional constraints. Therefore we chose a standard method based on DFT to determine the ground-state, which is then used to construct the initial Wigner function. The studies of the ground-state properties of the quantum and classical models revealed some similarities between the two. The behavior of the chemical potential in both cases is similar and follows the bulk result, up to temperatures of the order of Fermi temperature. Also the thermal energy for quantum and classical results are close to each other, and similar to the results obtained for a noninteracting electron gas. The above findings may suggest that the presence of surfaces does not have a major role on the ground-state properties, although, as we have seen, it is of paramount importance for transport phenomena.

Computing of the ground-state was just a preliminary step in our analysis of the electron dynamics. The first dynamical feature investigated in this thesis was connected with the non-interacting linear response. In our non–liner model we were able to access the linear regime by using the ground-state potential instead of the self-consistent electric potential. The frequency spectra obtained form the electric dipole were in good agreement with the transition frequencies between energy levels computed from DFT.

Concerning the non–linear dynamics, we were able to confirm that, in the case of large excitations, the electron transport is ballistic and occurs at a speed close to the Fermi velocity of the metal, which was observed in experimental measurements on thin gold film. The early stage after the laser excitation is dominated by collective oscillations of the electron gas at the plasma frequency. These oscillations are exponentially damped with different rates for the Wigner and Vlasov model. This fact can be pointed as the first difference between the quantum and classical description. Another difference can be found in the subsequent regime of low–frequency oscillations. Electrons bouncing back and forth against the film surfaces trigger a regime of slow oscillations observed in the behavior of the thermal energy. The period of these "ballistic" oscillations was equal to the time of flight L/v_F in the classical regime. Our key result in the quantum model was that, at weak excitation energies (smaller than one quantum of plasmon energy, $\hbar\omega_p$) the period of the low–frequency oscillations differs considerably from the ballistic value observed in the classical simulations. In this way, by reducing the strength of the initial excitation, we observe a clear transition from a classical to a quantum regime. We also proved that this result is robust, in the sense that it depends only weakly on physical parameters such as the electron temperature, or the choice of a specific exchange–correlation functional.

One of the advantages of the phase-space formulation of the quantum dynamics is that dissipative terms can be introduced similarly to classical transport models, like the Fokker–Planck equation. After including the electron–phonon scattering, the total energy is no longer conserved and the electrons start to interact incoherently with the phonons. The overall electron thermalization occurs in two stages. First, during the decoherence process, the Wigner distribution loses its negative values (thus becoming a real probability density) and tends to a classical Fermi–Dirac function with temperature $T_e \gg T_i$. Subsequently, the electron gas cools down until it reaches the lattice temperature. This relaxation process occurs on a time scale much longer than the decoherence time. The relaxation of the electron temperature obtained from the Wigner model is in good agreement with the two-temperature model (TTM). This fact provides a direct confirmation of the validity of the TTM.

Apart from the electronic properties of thin metal films we have also investigated the ground-state properties of semiconductor quantum wells. Although densities in metallic and semiconductor nano-objects differ by several orders of magnitudes, the relevant dimensionless parameters are rather similar, and we can adopt the same numerical methods as for metals.

The study of the ground state properties in a nonparabolic quantum well, in the presence of a random potential, revealed the apparent symmetry breaking of the wavefunctions. Contrary to what can be expected, the change of the fidelity (which measures the overlap between the wavefunctions) is largest for the low energy states. This effect can be connected to the spatial confinement of these states. The more general representation of the influence of the perturbation on our system was described in terms of the total fidelity. The perturbation-dependence of this quantity revealed a series of steps, which are related to the successive disruption of eigenstates of increasing energy.

7.2 Outlook

The electron dynamics described in Chapters 5 and 6, was based on the assumption that, due to their large mass, the ions respond so slowly that they can be assimilated as a motionless density (jellium model). For time scales of the order of a few picoseconds, the ions will start reacting to the electron motion, so that the jellium model becomes no longer valid. The concept of the electron-phonon coupling described in Chapter 6 was based on the dissipative terms introduced by analogy with classical transport models. We did not implemented explicitly the ionic motion. For a correct treatment of the ionic motion one should adopt a molecular dynamics point of view, and follow the (classical) trajectory of each ion.

The present thesis could be generalized by the incorporation of a magnetic field and an electron spin. For that purpose we will need to construct a Wigner equation that includes spin effects. In terms of the density matrix the evolution of the spin system can be written in the following form (Von Neumann equation):

$$i\hbar\frac{\partial\rho}{\partial t} = [H,\rho] \tag{7.1}$$

where

$$\rho = \begin{pmatrix} \rho^{\uparrow\uparrow} & \rho^{\uparrow\downarrow} \\ \rho^{\downarrow\uparrow} & \rho^{\downarrow\downarrow} \end{pmatrix}; \quad H = \begin{pmatrix} H^{\uparrow\uparrow} & H^{\uparrow\downarrow} \\ H^{\downarrow\uparrow} & H^{\downarrow\downarrow} \end{pmatrix}. \tag{7.2}$$

The only nondiagonal terms in the Hamiltonian come from the magnetic field $\mathbf{B}$, composed of an external part $\mathbf{B}_{\mathrm{EX}}$ and an "internal" part $\mathbf{B}_{\mathrm{XC}}$ that stems from the exchange and correlation energy.

The Wigner function will also be represented by a matrix

$$f = \begin{pmatrix} f^{\uparrow\uparrow} & f^{\uparrow\downarrow} \\ f^{\downarrow\uparrow} & f^{\downarrow\downarrow} \end{pmatrix}. \tag{7.3}$$

By introducing the transformation

$$\begin{aligned} \rho_0 &= \tfrac{\rho^{\uparrow\uparrow}+\rho^{\downarrow\downarrow}}{2}, \quad \rho_x = \tfrac{\rho^{\uparrow\downarrow}+\rho^{\downarrow\uparrow}}{2}, \\ \rho_z &= \tfrac{\rho^{\uparrow\uparrow}-\rho^{\downarrow\downarrow}}{2}, \quad \rho_y = \tfrac{\rho^{\downarrow\uparrow}-\rho^{\uparrow\downarrow}}{2i}, \end{aligned} \tag{7.4}$$

the Wigner functions can be written as

$$f_0(\mathbf{r},\mathbf{v},t) = \frac{m}{2\pi\hbar}\int \rho_0\left(\mathbf{r}-\frac{\lambda}{2},\mathbf{r}+\frac{\lambda}{2}\right) e^{im\mathbf{v}\lambda/\hbar}d\lambda, \tag{7.5}$$

$$f_\alpha(\mathbf{r},\mathbf{v},t) = \frac{m}{2\pi\hbar}\int \rho_\alpha\left(\mathbf{r}-\frac{\lambda}{2},\mathbf{r}+\frac{\lambda}{2}\right) e^{im\mathbf{v}\lambda/\hbar}d\lambda, \tag{7.6}$$

where $\alpha = x, y, x$. The equations of motion for the Wigner functions read as

$$\begin{aligned} &\frac{\partial f_0}{\partial t} + \mathbf{v}\frac{\partial f_0}{\partial \mathbf{r}} + \\ &\frac{em}{2i\pi\hbar^2}\iint d\lambda d\mathbf{v}' e^{im(\mathbf{v}-\mathbf{v}')\lambda/\hbar}\left[V\left(\mathbf{r}+\frac{\lambda}{2}\right) - V\left(\mathbf{r}-\frac{\lambda}{2}\right)\right] f_0(\mathbf{r},\mathbf{v}',t) - \\ &\sum_\alpha \frac{m\mu_B}{2i\pi\hbar^2}\iint d\lambda d\mathbf{v}' e^{im(\mathbf{v}-\mathbf{v}')\lambda/\hbar}\left[B_\alpha\left(\mathbf{r}+\frac{\lambda}{2}\right) - B_\alpha\left(\mathbf{r}-\frac{\lambda}{2}\right)\right] f_\alpha(\mathbf{r},\mathbf{v}',t) = 0 \end{aligned} \tag{7.7}$$

$$\begin{aligned} &\frac{\partial f_\alpha}{\partial t} + \mathbf{v}\frac{\partial f_\alpha}{\partial \mathbf{r}} + \\ &\frac{em}{2i\pi\hbar^2}\iint d\lambda d\mathbf{v}' e^{im(\mathbf{v}-\mathbf{v}')\lambda/\hbar}\left[V\left(\mathbf{r}+\frac{\lambda}{2}\right) - V\left(\mathbf{r}-\frac{\lambda}{2}\right)\right] f_\alpha(\mathbf{r},\mathbf{v}',t) - \\ &\sum_\alpha \frac{m\mu_B}{2i\pi\hbar^2}\iint d\lambda d\mathbf{v}' e^{im(\mathbf{v}-\mathbf{v}')\lambda/\hbar}\left[B_\alpha\left(\mathbf{r}+\frac{\lambda}{2}\right) - B_\alpha\left(\mathbf{r}-\frac{\lambda}{2}\right)\right] f_0(\mathbf{r},\mathbf{v}',t) = 0 \end{aligned} \tag{7.8}$$

where μ_B is Bohr's magneton. The above equations will give the complete picture of the electron dynamics in the quantum regime.

Concerning the study of the ground-state fidelity, future investigations might aim to clarify the role of the electron density in the quantum well. As it was shown in [68] the electron density has a large influence on the dynamical properties of the quantum fidelity, and it would be instructive to have similar results for the static case. Another possible direction for research in this field is an investigation of the so-called "fidelity susceptibility" used to identify quantum phase transitions [79]. Because the fidelity is a measure of similarity between states, it should drop abruptly at critical points, as a consequence of the dramatic changes in the structure of the ground-state, regardless of what type of internal order is present in quantum many-body states. A perhaps more effective indicator is given by the singularity in the second derivative of the fidelity, which is the above-mentioned fidelity susceptibility. Finally, there is the question of the influence of a finite temperature on our system. When the temperature increases new states become available to the electrons, and it would be interesting to study how these states change with the perturbation.

Appendix A

Fokker–Planck equation in 1D

Our one-dimensional approximation used to describe thin metal films requires sometimes the projection of the velocity states parallel to the surface on the perpendicular direction (see for example section 2.3). Let us now justify the connection between the 3D functional $G[\,\cdot\,]$ for fermions and its 1D counterpart.

The Fokker–Planck equation for fermions in 3D reads as:

$$\frac{\partial f}{\partial t} = \nabla_{\mathbf{v}} \cdot (D \nabla_{\mathbf{v}} f) + \nabla_{\mathbf{v}} \cdot [\mathbf{v} f (1-f)] \tag{A.1}$$

where $f = f(\mathbf{v}, t) = f(v_x, \mathbf{v}_\perp)$. We assume that the 3D distribution can be written as:

$$f_{\mathrm{3D}}(\mathbf{v}) = \frac{1}{1 + e^{g(v_x,t)} \cdot e^{\beta v_\perp^2/2}} \tag{A.2}$$

with $m = 1$ and $\beta = 1/k_B T_e$. Integrating over $\mathbf{v}_\perp = (v_y, v_z)$ we obtain:

$$\frac{\partial f_{\mathrm{1D}}}{\partial t} = \frac{\partial^2 f_{\mathrm{1D}}}{\partial v_x^2} + \frac{\partial}{\partial v_x} \left(v_x G\left[f_{\mathrm{1D}} \right] \right) \tag{A.3}$$

where

$$f_{\mathrm{1D}} \equiv \int_0^\infty f_{\mathrm{3D}}(\mathbf{v}) d\mathbf{v}_\perp = 2\pi \int_0^\infty f_{\mathrm{3D}}(\mathbf{v}) v_\perp dv_\perp \tag{A.4}$$

and

$$G\left[f_{\mathrm{1D}} \right] = \int_0^\infty f_{\mathrm{3D}} (1 - f_{\mathrm{3D}}) d\mathbf{v}_\perp . \tag{A.5}$$

Taking $a = e^{g(v_x)}$ the integral of the linear term in the last equation is

$$\int_0^\infty f_{3\mathrm{D}} v_\perp dv_\perp = \int_0^\infty \frac{v_\perp dv_\perp}{1 + a \cdot e^{\beta v_\perp^2/2}}. \tag{A.6}$$

Substituting $z \equiv \beta v_\perp^2/2$ we have

$$\frac{1}{\beta} \int_0^\infty \frac{dz}{ae^z + 1} = \frac{1}{\beta} \int_0^\infty \frac{e^{-z} dz}{a + e^{-z}}, \tag{A.7}$$

making another substitution $y = e^{-z}$:

$$\int_0^1 \frac{dy}{a + y} = \frac{1}{\beta} \ln \left[(a + y)\right]_0^1 \tag{A.8}$$

Going back to the previous notation we obtain:

$$\int_0^\infty f_{3\mathrm{D}} v_\perp dv_\perp = \frac{1}{\beta} \ln \left(\frac{1 + e^{g(v_x)}}{e^{g(v_x)}} \right) = \frac{1}{\beta} \ln \left(1 + e^{-g(v_x)}\right). \tag{A.9}$$

Now we need integrate the nonlinear term

$$\int_0^\infty f_{3\mathrm{D}}^2 v_\perp dv_\perp = \int_0^\infty \frac{v_\perp dv_\perp}{\left[1 + a \cdot e^{\beta v_\perp^2/2}\right]^2} \tag{A.10}$$

by making the same substitutions as above we get:

$$\int_0^1 \frac{dy}{(a + y)^2} = \frac{1}{\beta} \left[\frac{a}{a + y} + \ln |a + y| \right]_0^1 = \frac{1}{\beta} \left[\frac{a}{a + 1} - 1 + \ln \left| \frac{1 + a}{a} \right| \right]. \tag{A.11}$$

A back transformation leads to the following expression

$$\int_0^\infty f_{3\mathrm{D}}^2 v_\perp dv_\perp = \frac{1}{\beta} \left[-\frac{1}{1 + e^{g(v_x)}} + \ln \left| 1 + e^{-g(v_x)} \right| \right]. \tag{A.12}$$

In summary

$$\int_0^\infty (f_{3\mathrm{D}} - f_{3\mathrm{D}}^2) d\mathbf{v}_\perp = \frac{1}{\beta} \frac{1}{1 + e^{g(v_x)}} \equiv G[f_{1\mathrm{D}}]. \tag{A.13}$$

Now, let us compute

$$f_0\left(1-e^{-f_{1\mathrm{D}}/f_0}\right) \tag{A.14}$$

with $f_0=\beta^{-1}$ we obtain

$$\beta^{-1}\left(1-e^{-\beta f_{1\mathrm{D}}}\right)=\beta^{-1}\left(1-\frac{1}{1+e^{-g(v_x)}}\right)=\frac{1}{\beta}\frac{1}{1+e^{g(v_x)}}, \tag{A.15}$$

which is equal to (A.13).

Thus we have proved that

$$G[f_{1\mathrm{D}}]=f_0\left(1-e^{-f_{1\mathrm{D}}/f_0}\right) \tag{A.16}$$

which is the expression used in Chapter 5 for fermions in 1D.

Bibliography

[1] D. L. Feldheim and C. A. Foss, *Metal Nanoparticles.* Marcel Dekker, 2002.

[2] D. K. Ferry, S. M. Goodnick, and J. Bird, *Transport in nanostructures.* Cambridge University Press, 2009.

[3] E. L. Wolf, *Nanophysics and Nanotechnology.* Wiley-vch Verlag GmbH and Co. KGaA, 2004.

[4] B. Bhushan, *Springer handbook of nanotechnology.* Springer–Verlag Berlin Heidelberg, 2004.

[5] J. Y. Bigot, V. Halté, J. C. Merle, and A. Daunois, “Electron dynamics in metallic nanoparticles,” *Chemical Physics*, vol. 251, no. 1-3, pp. 181 – 203, 2000.

[6] S. D. Brorson, J. G. Fujimoto, and E. P. Ippen, “Femtosecond electronic heat-transport dynamics in thin gold films,” *Phys. Rev. Lett.*, vol. 59, pp. 1962–1965, Oct 1987.

[7] C. Suárez, W. E. Bron, and T. Juhasz, “Dynamics and transport of electronic carriers in thin gold films,” *Phys. Rev. Lett.*, vol. 75, pp. 4536–4539, Dec 1995.

[8] R. H. M. Groeneveld, R. Sprik, and A. Lagendijk, “Femtosecond spectroscopy of electron-electron and electron-phonon energy relaxation in Ag and Au,” *Phys. Rev. B*, vol. 51, pp. 11433–11445, May 1995.

[9] C.-K. Sun, F. Vallée, L. H. Acioli, E. P. Ippen, and J. G. Fujimoto, “Femtosecond-tunable measurement of electron thermalization in gold,” *Phys. Rev. B*, vol. 50, pp. 15337–15348, Nov 1994.

[10] W. Rudolph, P. Dorn, X. Liu, N. Vretenar, and R. Stock, “Microscopy with femtosecond laser pulses: applications in engineering, physics and biomedicine,” *Applied Surface Science*, vol. 208–209, pp. 327–332, 2003.

[11] J.-S. Lauret, C. Voisin, G. Cassabois, C. Delalande, P. Roussignol, O. Jost, and L. Capes, "Ultrafast carrier dynamics in single-wall carbon nanotubes," *Phys. Rev. Lett.*, vol. 90, p. 057404, Feb 2003.

[12] M. Maier, G. Wrigge, M. A. Hoffmann, P. Didier, and B. v. Issendorff, "Observation of electron gas cooling in free sodium clusters," *Phys. Rev. Lett.*, vol. 96, p. 117405, Mar 2006.

[13] E. E. B. Campbell, K. Hansen, K. Hoffmann, G. Korn, M. Tchaplyguine, M. Wittmann, and I. V. Hertel, "From above threshold ionization to statistical electron emission: The laser pulse-duration dependence of c_{60} photoelectron spectra," *Phys. Rev. Lett.*, vol. 84, pp. 2128–2131, Mar 2000.

[14] M. Nisoli, S. Stagira, S. De Silvestri, A. Stella, P. Tognini, P. Cheyssac, and R. Kofman, "Ultrafast electronic dynamics in solid and liquid gallium nanoparticles," *Phys. Rev. Lett.*, vol. 78, pp. 3575–3578, May 1997.

[15] M. Madjet and P. A. Hervieux, "Many-body effects and autoionization resonances in photoionization of simple metal clusters," *Eur. Phys. J. D*, vol. 9, p. 217, 1999.

[16] B. Rethfeld, A. Kaiser, M. Vicanek, and G. Simon, "Ultrafast dynamics of nonequilibrium electrons in metals under femtosecond laser irradiation," *Phys. Rev. B*, vol. 65, p. 214303, May 2002.

[17] M. Aeschlimann, M. Bauer, S. Pawlik, R. Knorren, G. Bouzerar, and K. Bennemann, "Transport and dynamics of optically excited electrons in metals," *Applied Physics A: Materials Science and Processing*, vol. 71, pp. 485–491, 2000.

[18] R. Knorren, G. Bouzerar, and K. H. Bennemann, "Theory for transport and temperature effects on two-photon photoemission: Application to cu," *Phys. Rev. B*, vol. 63, p. 125122, Mar 2001.

[19] C. Guillon, P. Langot, N. D. Fatti, and F. Vallée, "Nonequilibrium electron energy-loss kinetics in metal clusters," *New Journal of Physics*, vol. 5, no. 1, p. 13, 2003.

[20] V. I. Tatarskii, "The Wigner representation of quantum mechanics," *Sov. Phys. Usp.*, vol. 26, pp. 311–327, 1983.

[21] L. Saminadayar, C. Bauerle, and D. Mailly, *Encyclopedia of Nanoscience and Nanotechnology*, vol. 3. American Scientific, 2004.

[22] C. P. Poole and F. J. Owens, *Introduction to nanotechnology.* John Wiley and Sons, 2003.

[23] X. Liu, R. Stock, and W. Rudolph, "Ballistic electron transport in au films," *Phys. Rev. B*, vol. 72, p. 195431, Nov 2005.

[24] J. D. Walecka, *Fundamentals of Statistical Mechanics.* Imperial College Press, 1989.

[25] R. R. Puri, *Mathematic methods of quantum optics.* Springer, 2001.

[26] S. Ichmaru, *Statistical Plasma Physics.* Addison–Wesley, 1992.

[27] P. M. Bellan, *Fundamentals of plasma physics.* Cambridge University Press, 2006.

[28] G. Manfredi and P.-A. Hervieux, "Vlasov simulations of electron dynamics in metallic nanostructures," *Computational Materials Science*, vol. 35, no. 3, pp. 327 – 331, 2006.

[29] E. Wigner, "On the quantum correction for thermodynamic equilibrium," *Phys. Rev.*, vol. 40, pp. 749–759, Jun 1932.

[30] L. Hai-Woong, "Theory and application of the quantum phase-space distribution functions," *Phys. Rep.*, vol. 259, pp. 147–211, Aug. 1995.

[31] L. E. Ballentine, *Quantum Mechanics: A modern development.* Word scientific publishing, 1998.

[32] G. Manfredi, "How to model quantum plasmas," *Fields Institute Communications Series*, vol. 46, pp. 263–287, 2005.

[33] A. Kenfack and K. Zyczkowski, "Negativity of the wigner function as an indicator of non-classicality," *Journal of Optics B: Quantum and Semiclassical Optics*, vol. 6, no. 10, p. 396, 2004.

[34] A. Liebsh, *Electronic Excitations at Metal Surfaces.* Plenum, 1997.

[35] "Friedel oscillations: wherein we learn that the electron has a size," June 2009. `http://gravityandlevity.wordpress.com/2009/06/02/friedel-oscillations-wherein-we-learn-that-the-electron-has-a-size/`.

[36] G. Manfredi and P.-A. Hervieux, "Finite-size and nonlinear effects on the ultrafast electron transport in thin metal films," *Physical Review B (Condensed Matter and Materials Physics)*, vol. 72, no. 15, p. 155421, 2005.

[37] L. D. Landau and E. M. Lifshitz, *Statistical physics*, vol. 1. Oxford, 3 ed., 1980.

[38] R. Fitzpatrick, *Introduction to plasma physics.* 2006.

[39] E. S. F. Filbet and P. Bertrand, "Conservative numerical schemes for the vlasov equation," *J. Comput. Phys.*, vol. 172, no. 166, pp. 166–187, 2001.

[40] N.-D. Suh, M. R. Feix, and P. Bertrand, "Numerical simulation of the quantum liouville-poisson system," *Journal of Computational Physics*, vol. 94, no. 2, pp. 403 – 418, 1991.

[41] C. Cheng and G. Knorr, "The integration of the vlasov equation in configuration space,"

[42] B. Izrar, A. Ghizzo, P. Bertrand, E. Fijalkow, and M. R. Feix, "Integration of vlasov equation by a fast fourier eulerian code," *Computer Physics Communications*, vol. 52, no. 3, pp. 375 – 382, 1989.

[43] E. Fijalkow, "Numerical solution to the Vlasov equation: The 1D code," *Computer Physics Communications*, vol. 116, no. 2-3, pp. 329 – 335, 1999.

[44] F. Calvayrac, P.-G. Reinhard, E. Suraud, and C. Ullrich, "Nonlinear electron dynamics in metal clusters," *Physics Reports*, vol. 337, pp. 493–578, October 2000.

[45] A. Kawabata and R. Kubo, "Electronic properties of fine metallic particles. ii. plasma resonance absorption," *Journal of the Physical Society of Japan*, vol. 21, no. 9, pp. 1765–1772, 1966.

[46] U. Kreibig and M. Vollmer, *Optical Properties of Metal Clusters.* Springer, 1995.

[47] B. Lamprecht, J. R. Krenn, A. Leitner, and F. R. Aussenegg, "Resonant and off-resonant light-driven plasmons in metal nanoparticles studied by femtosecond-resolution third-harmonic generation," *Phys. Rev. Lett.*, vol. 83, pp. 4421–4424, Nov 1999.

[48] R. A. Molina, D. Weinmann, and R. A. Jalabert, "Oscillatory size dependence of the surface plasmon linewidth in metallic nanoparticles," *Phys. Rev. B*, vol. 65, p. 155427, Apr 2002.

[49] D. F. Zaretsky, P. A. Korneev, S. V. Popruzhenko, and W. Becker, "Landau damping in thin films irradiated by a strong laser field," *Journal of Physics B: Atomic, Molecular and Optical Physics*, vol. 37, no. 24, p. 4817, 2004.

[50] G. Manfredi and P.-A. Hervieux, "Vlasov simulations of ultrafast electron dynamics and transport in thin metal films," *Phys. Rev. B*, vol. 70, p. 201402, Nov 2004.

[51] G. Manfredi and P.-A. Hervieux, "Nonlinear absorption of ultrashort laser pulses in thin metal films," *Opt. Lett.*, vol. 30, pp. 3090–3092, Nov 2005.

[52] N. Crouseilles, P.-A. Hervieux, and G. Manfredi, "Quantum hydrodynamic model for the nonlinear electron dynamics in thin metal films," *Phys. Rev. B*, vol. 78, p. 155412, Oct 2008.

[53] A. Arbouet, C. Voisin, D. Christofilos, P. Langot, N. D. Fatti, F. Vallée, J. Lermé, G. Celep, E. Cottancin, M. Gaudry, M. Pellarin, M. Broyer, M. Maillard, M. P. Pileni, and M. Treguer, "Electron-phonon scattering in metal clusters," *Phys. Rev. Lett.*, vol. 90, p. 177401, Apr 2003.

[54] U. Schwengelbeck, L. Plaja, L. Roso, and E. C. Jarque, "Plasmon-induced photon emission from thin metal films," *Journal of Physics B: Atomic, Molecular and Optical Physics*, vol. 33, no. 8, p. 1653, 2000.

[55] R. D'Agosta and G. Vignale, "Relaxation in time-dependent current-density-functional theory," *Phys. Rev. Lett.*, vol. 96, p. 016405, Jan 2006.

[56] L. Jiang and H.-L. Tsai, "Improved two-temperature model and its application in ultrashort laser heating of metal films," *Journal of Heat Transfer*, vol. 127, no. 10, pp. 1167–1173, 2005.

[57] J. G. Fujimoto, J. M. Liu, E. P. Ippen, and N. Bloembergen, "Femtosecond laser interaction with metallic tungsten and nonequilibrium electron and lattice temperatures," *Phys. Rev. Lett.*, vol. 53, pp. 1837–1840, Nov 1984.

[58] G. V. Hartland, "Measurements of the material properties of metal nanoparticles by time-resolved spectroscopy," *Phys. Chem. Chem. Phys.*, vol. 6, pp. 5263–5274, 2004.

[59] S. Deléglise, I. Dotsenko, C. Sayrin, J. Bernu, M. Brune, J.-M. Raimond, and S. Haroche, "Reconstruction of non-classical cavity field states with snapshots of their decoherence," *Nature*, vol. 455, pp. 510–514, 2008.

[60] Z. Ovadyahu, "Nonequilibrium dephasing in two-dimensional indium oxide films," *Phys. Rev. B*, vol. 63, p. 235403, May 2001.

[61] B. L. Altshuler, A. G. Aronov, and D. E. Khmelnitsky, “Effects of electron-electron collisions with small energy transfers on quantum localisation,” *Journal of Physics C: Solid State Physics*, vol. 15, no. 36, p. 7367, 1982.

[62] P. Mohanty, E. M. Q. Jariwala, and R. A. Webb, “Intrinsic decoherence in mesoscopic systems,” *Phys. Rev. Lett.*, vol. 78, pp. 3366–3369, Apr 1997.

[63] D. S. Golubev and A. D. Zaikin, “Quantum decoherence in disordered mesoscopic systems,” *Phys. Rev. Lett.*, vol. 81, pp. 1074–1077, Aug 1998.

[64] F. Pierre and N. O. Birge, “Dephasing by extremely dilute magnetic impurities revealed by aharonov-bohm oscillations,” *Phys. Rev. Lett.*, vol. 89, p. 206804, Oct 2002.

[65] Y. Niimi, Y. Baines, T. Capron, D. Mailly, F.-Y. Lo, A. D. Wieck, T. Meunier, L. Saminadayar, and C. Bäuerle, “Quantum coherence at low temperatures in mesoscopic systems: Effect of disorder,” *Phys. Rev. B*, vol. 81, p. 245306, Jun 2010.

[66] H. O. Wijewardane and C. A. Ullrich, “Coherent control of intersubband optical bistability in quantum wells,” *Applied Physics Letters*, vol. 84, no. 20, pp. 3984–3986, 2004.

[67] R. Schlipper, R. Kusche, B. v. Issendorff, and H. Haberland, “Thermal emission of electrons from highly excited sodium clusters,” *Applied Physics A: Materials Science and Processing*, vol. 72, pp. 255–259, 2001. 10.1007/s003390100763.

[68] G. Manfredi and P.-A. Hervieux, “Loschmidt echo for the many-electron dynamics in nonparabolic quantum wells,” *New Journal of Physics*, vol. 11, no. 1, p. 013050, 2009.

[69] A. Peres, “Stability of quantum motion in chaotic and regular systems,” *Phys. Rev. A*, vol. 30, pp. 1610–1615, Oct 1984.

[70] M.-F. Yang, “Ground-state fidelity in one-dimensional gapless models,” *Phys. Rev. B*, vol. 76, p. 180403, Nov 2007.

[71] M. Cozzini, P. Giorda, and P. Zanardi, “Quantum phase transitions and quantum fidelity in free fermion graphs,” *Phys. Rev. B*, vol. 75, p. 014439, Jan 2007.

[72] P. Zanardi and N. Paunković, “Ground state overlap and quantum phase transitions,” *Phys. Rev. E*, vol. 74, p. 031123, Sep 2006.

[73] J.-H. Zhao and H.-Q. Zhou, "Singularities in ground-state fidelity and quantum phase transitions for the kitaev model," *Phys. Rev. B*, vol. 80, p. 014403, Jul 2009.

[74] D. Loss and D. P. DiVincenzo, "Quantum computation with quantum dots," *Phys. Rev. A*, vol. 57, pp. 120–126, Jan 1998.

[75] P. Zoller, T. Beth, D. Binosi, R. Blatt, H. Briegel, D. Bruss, T. Calarco, J. I. Cirac, D. Deutsch, J. Eisert, A. Ekert, C. Fabre, N. Gisin, P. Grangiere, M. Grassl, S. Haroche, A. Imamoglu, A. Karlson, J. Kempe, L. Kouwenhoven, S. Kröll, G. Leuchs, M. Lewenstein, D. Loss, N. Lütkenhaus, S. Massar, J. E. Mooij, M. B. Plenio, E. Polzik, S. Popescu, G. Rempe, A. Sergienko, D. Suter, J. Twamley, G. Wendin, R. Werner, A. Winter, J. Wrachtrup, and A. Zeilinger, "Quantum information processing and communication," *The European Physical Journal D - Atomic, Molecular, Optical and Plasma Physics*, vol. 36, pp. 203–228, 2005.

[76] J. Gorman, D. G. Hasko, and D. A. Williams, "Charge-qubit operation of an isolated double quantum dot," *Phys. Rev. Lett.*, vol. 95, p. 090502, Aug 2005.

[77] L. Jönsson, M. M. Steiner, and J. W. Wilkins, "Coherent electron–hole correlations in quantum dots," *Applied Physics Letters*, vol. 70, no. 9, pp. 1140–1142, 1997.

[78] L. Brey, J. Dempsey, N. F. Johnson, and B. I. Halperin, "Infrared optical absorption in imperfect parabolic quantum wells," *Phys. Rev. B*, vol. 42, pp. 1240–1247, Jul 1990.

[79] W.-L. You, Y.-W. Li, and S.-J. Gu, "Fidelity, dynamic structure factor, and susceptibility in critical phenomena," *Phys. Rev. E*, vol. 76, p. 022101, Aug 2007.